

ACOUSTIC METAMATERIAL DESIGN AND APPLICATIONS

BY

SHU ZHANG

DISSERTATION

Submitted in partial fulfillment of the requirements  
for the degree of Doctor of Philosophy in Mechanical Engineering  
in the Graduate College of the  
University of Illinois at Urbana-Champaign, 2010

Urbana, Illinois

Doctoral Committee:

Assistant Professor Nicholas X. Fang, Chair and Director of Research  
Professor Jianming Jin  
Associate Professor Gustavo Gioia  
Associate Professor Harley T. Johnson

## ABSTRACT

The explosion of interest in metamaterials is due to the dramatically increased manipulation ability over light as well as sound waves. This material research was stimulated by the opportunity to develop an artificial media with negative refractive index and the application in superlens which allows super-resolution imaging. High-resolution acoustic imaging techniques are the essential tools for nondestructive testing and medical screening. However, the spatial resolution of the conventional acoustic imaging methods is restricted by the incident wavelength of ultrasound. This is due to the quickly fading evanescent fields which carry the subwavelength features of objects. By focusing the propagating wave and recovering the evanescent field, a flat lens with negative-index can potentially overcome the diffraction limit. We present the first experimental demonstration of focusing ultrasound waves through a flat acoustic metamaterial lens composed of a planar network of subwavelength Helmholtz resonators. We observed a tight focus of half-wavelength in width at 60.5 KHz by imaging a point source. This result is in excellent agreement with the numerical simulation by transmission line model in which we derived the effective mass density and compressibility. This metamaterial lens also displays variable focal length at different frequencies. Our experiment shows the promise of designing compact and light-weight ultrasound imaging elements.

Moreover, the concept of metamaterial extends far beyond negative refraction, rather giving enormous choice of material parameters for different applications. One of the most interesting examples these years is the invisible cloak. Such a device is proposed to render the hidden object undetectable under the flow of light or sound, by guiding and controlling the wave path through an engineered space surrounding the object. However, the cloak designed by transformation optics usually calls for a highly anisotropic metamaterial, which make the experimental studies remain challenging. We present here the first practical realization of a low-loss and broadband acoustic cloak for underwater ultrasound. This metamaterial cloak is constructed with a network of acoustic circuit elements, namely serial inductors and shunt capacitors. Our experiment clearly shows that the acoustic cloak can effectively bend the ultrasound waves around the hidden object, with reduced scattering and shadow. Due to the non-resonant nature of the building elements, this low loss ( $\sim 6\text{dB/m}$ ) cylindrical cloak exhibits excellent invisibility over a broad frequency range from 52 to 64 kHz in the measurements. The low visibility of the cloaked object for underwater ultrasound shed a light on the fundamental understanding of manipulation, storage and control of acoustic waves. Furthermore, our experimental study indicates that this design approach should be scalable to different acoustic frequencies and offers the possibility for a variety of devices based on coordinate transformation.

## ACKNOWLEDGMENTS

I would like to thank my advisor, Dr. Nicholas Fang, for providing me the wonderful opportunity to finish my PhD degree and work on these exciting projects. His unwavering support, invaluable guidance and suggestions in exploration this research and presenting the thesis are greatly appreciated.

At the same time, many thanks to all the committee members, Dr. Jianming Jin, Dr. Gustavo Gioia and Dr. Harley T. Johnson, for their invaluable suggestions and help.

Special thank to Dr. Leilei Yin for his great help on experiment techniques. I am very grateful to everybody in our research group: Pratik Chaturvedi, Jun Xu, Keng Hao Hsu, Kin Hung Fung, Tarun Malik, Anil Kumar, Howon Lee and Hyungjin Ma. I truly learned the most from them. They were the first people I turned to for help with a challenging problem.

Finally, I would like to thank my parents for their constant encouragement and belief in me during this course. I am greatly indebted to Chunguang Xia for his special efforts in spending countless hours helping me. His support made the last few years of hard work possible. I would also like to extend my thanks to all my friends who kept me in good spirits during my stay here.

## Table of Contents

1. INTRODUCTION.....	1
1.1. Metamaterial.....	1
1.2. Thesis Organization.....	4
2 ACOUSTIC TRANSMISSION LINE .....	9
2.1 Introduction .....	9
2.2 Locally Resonant Sonic Materials.....	10
2.3 Acoustic Circuits .....	11
2.4 Reflection and Transmission .....	15
2.5 Absorption and Attenuation of Sound in Pipe.....	23
2.6 Acoustic Isotropic Metamaterial .....	36
2.7 Anisotropic Acoustic Metamaterial.....	42
3 ULTRASOUND FOCUSING USING ACOUSTICMETAMATERIAL NETWORK.....	51
3.1 Introduction .....	51
3.2 Negative Refractive Index Lens.....	53
3.3 Phononic Crystal .....	55
3.4 Ultrasound Focusing by Acoustic Transmission Line Network.....	59
4 BROADBAND ACOUSTIC CLOAK FOR ULTRASOUND WAVES .....	86
4.1 Introduction .....	86
4.2 Optical Transformation .....	88
4.3 Acoustic Cloak .....	95
4.4 Numerical Simulation of Acoustic Cloak Based on Transmission Line Model.....	98
4.5 Irregular Transmission Line Network .....	103
4.6 Experimental Study of Acoustic Cloak Based on Transmission Line Model .....	110
5 SUMMARY AND FUTURE WORK .....	130
5.1 Summary .....	130
5.2 Future Work.....	131
APPENDIX A: LUMPED CIRCUIT MODEL .....	133
APPENDIX B: FRESNEL LENS DESIGN BY ACOUSTIC TRANSMISSION LINE .....	140
APPENDIX C: NEGATIVE INDEX LENS BASED ON METAL-INSULATOR-METAL (MIM) WAVEGUIDES.....	148
APPENDIX D: SCATTERING FIELDS FROM THE CLOAK.....	161
APPENDIX E: EXPERIMENTAL SETUP AND DATA ACQUISITION.....	174
APPENDIX F: CICUIT MODELING.....	179

# 1 INTRODUCTION

## 1.1 Metamaterial

Over the past eight years, metamaterials have shown tremendous potential in many disciplines of science and technology. The explosion of interest in metamaterials is due to the dramatically increased manipulation ability over light as well as sound waves which are not available in nature. The core concept of metamaterial is to replace the molecules with man-made structures, viewed as “artificial atoms” on a scale much less than the relevant wavelength. In this way, the metamaterial can be described using a small number of effective parameters. In late 1960s, the concept of metamaterial was first proposed by Veselago for electromagnetic wave<sup>1</sup>. He predicted that a medium with simultaneous negative permittivity and negative permeability were shown to have a negative refractive index. But this negative index medium remained as an academic curiosity for almost thirty years, until Pendry *et al*<sup>2,3</sup> proposed the designs of artificial structured materials which would have effectively negative permeability and permittivity. The negative refractive index was first experimentally demonstrated at GHz frequency.<sup>4,5</sup>

It is undoubtedly of interest whether we can design metamaterial for the wave in other systems, for example, acoustic wave. The two waves are certainly different. Acoustic wave is longitudinal wave; the parameters used to describe the wave are pressure and particle velocity. In

electromagnetism (EM), both electric and magnetic fields are transverse wave. However, the two wave systems have the common physical concepts as wavevector, wave impedance, and power flow. Moreover, in a two-dimensional (2D) case, when there is only one polarization mode, the electromagnetic wave has scalar wave formulation. Therefore, the two sets of equations for acoustic and electromagnetic waves in isotropic media are dual of each other by the replacement as shown in Table 1.1 and this isomorphism holds for anisotropic medium as well. Table 1.1 presents the analogy between acoustic and transverse magnetic field in 2D under harmonic excitation. From this equivalence, the desirable effective density and compressibility need to be established by structured material to realize exotic sound wave properties. The optical and acoustic metamaterial share many similar implementation approaches as well.

The first acoustic metamaterial, also called as locally resonant sonic materials was demonstrated with negative effective dynamic density.<sup>6</sup> The effective parameters can be ascribed to this material since the unit cell is sub-wavelength size at the resonance frequency. Furthermore, by combining two types of resonant structural, acoustic metamaterial with simultaneous negative bulk modulus and negative mass density was numerically demonstrated.<sup>7</sup> Recently, Fang *et al.*<sup>8</sup> proposed a new class of acoustic metamaterial which consists of a 1D array of Helmholtz resonators which exhibits dynamic effective negative modulus in experiment.

**Table 1.1** Analogy between acoustic and electromagnetic variables and material characteristics

Acoustics	Electromagnetism (TMz)	Analogy
$\frac{\partial P}{\partial x} = -i\omega\rho_x u_x$	$\frac{\partial E_z}{\partial x} = -i\omega\mu_y H_y$	
$\frac{\partial P}{\partial y} = -i\omega\rho_y u_y$	$\frac{\partial E_z}{\partial y} = i\omega\mu_x H_x$	
$\frac{\partial u_x}{\partial x} + \frac{\partial u_y}{\partial y} = -i\omega\beta P$	$\frac{\partial H_y}{\partial x} - \frac{\partial H_x}{\partial y} = -i\omega\varepsilon_z E_z$	
Acoustic pressure $P$	Electric field $E_z$	$-E_z \leftrightarrow P$
Particle velocity $u_x, u_y$	Magnetic field $H_x, H_y$	$H_y \leftrightarrow -u_x, H_x \leftrightarrow u_y$
Dynamic density $\rho_x, \rho_y$	Permeability $\mu_x, \mu_y$	$\rho_x \leftrightarrow \mu_y, \rho_y \leftrightarrow \mu_x$
Dynamic compressibility $\beta$	Permittivity $\varepsilon_z$	$\varepsilon_z \leftrightarrow \beta$

The concept of metamaterial extends far beyond negative refraction, rather giving enormous choice of material parameters for different applications. One of the most interesting examples is the invisible cloak by transformation optics.<sup>9, 10</sup> A simpler version of two-dimensional (2D) cloak was implemented at microwave frequency.<sup>11</sup> Later on, this new design paradigm is extended theoretically to make an “inaudible cloak” for sound wave.<sup>12,13,14,15</sup> The sound wave is directed to flow over a shielded object like water flowing around a rock. Because the waves reform their original conformation after passing such a shielded object, the object becomes

invisible to the detector. The cloak for surface wave is also proposed in hertz frequency range. <sup>16</sup>

Since the inception of the term metamaterials, acoustic metamaterials have been explored theoretically but there has been little headway on the experimental front. The development of acoustic metamaterial will yield new insight in material science and offer great opportunities for several applications.

## **1.2 Thesis Organization**

The central theme of this thesis is to design and characterize the acoustic metamaterial for potential application in ultrasound imaging and sound controlling. This dissertation is organized into four chapters. Besides the current chapter which intends to give a brief introduction of the acoustic metamaterial and the motivations of this dissertation, the other three chapters organized as following:

The second chapter describes the approach to build an acoustic metamaterial based on the transmission line model. The basic concept and derivation of lumped acoustic circuit is introduced. In the lumped circuit model, the aluminum is assumed as acoustically rigid, considering the acoustic impedance  $\rho c$  of aluminum is around eleven times of that of water. A more careful analysis including elasticity of the solid suggested that at low frequency the majority of acoustic energy can be predominantly confined in the fluid, when such an excitation

originates from the liquid.<sup>17</sup> On the other hand, aluminum does participate in the wave propagation, and may increase the loss.<sup>18</sup> Moreover, the loss and limitation of current lumped circuit model are discussed.

The third chapter deals with one of the most promising application of acoustic metamaterials, obtaining a negative refractive index lens which can possibly overcome the diffraction limit. An acoustic system is simulated by the analogous lumped circuit model in which the behavior of the current resembles the motion of the fluid. Based on this lumped network, an acoustic negative index lens is implemented by a two-dimensional (2D) array of subwavelength Helmholtz resonators. The experimental studies are presented, demonstrating the focusing of ultrasound waves through the negative index lens.

The fourth chapter is to construct an anisotropic cloak for sound waves at kHz range. Relying on the flexibility of the transmission line approach, an acoustic metamaterial exhibiting effective anisotropic density and bulk modulus is proposed to construct the cloak. An object can be shielded inside the cloak and thus becomes invisible to the detector. Given the simulation results, the sound-shielding capability is explored experimentally by measuring the scattered pressure field.

## References

---

<sup>1</sup> Veselago, V. G., “The electrodynamics of substances with simultaneously negative values of  $\mu$  and  $\epsilon$ ,” *Sov. Phys. Usp.*, Vol. 10, No. 4, 509 (1968)

<sup>2</sup> J. B. Pendry, A. J. Holden, D. J. Robbins, W. J. Stewart. “Magnetism from conductors and enhanced nonlinear phenomena.” *IEEE Trans. Microwave Theory Tech.* 47, 2075–2084 (1999).

<sup>3</sup> J. B. Pendry, A. J. Holden, W. J. Stewart and I. Youngs, “Extremely low frequency plasmons in metallic mesostructures.” *Phys. Rev. Lett.* 76, 4773–4776 (1996).

<sup>4</sup> Smith, D. R. et al. “Composite medium with simultaneously negative permeability and permittivity”. *Phys. Rev. Lett.* 84, 4184–4187 (2003).

<sup>5</sup> Shelby, R. A., Smith, D. R. & Schultz, S., “Experimental verification of a negative index of refraction”, *Science* 292, 77–79 (2001).

<sup>6</sup> Z. Liu, X. Zhang, Y. Mao, Y. Y. Zhu, Z. Yang, C. T. Chan, and P. Sheng, “Locally Resonant

---

Sonic Materials”, *Science* 289, 1734 (2000).

<sup>7</sup> Y. Ding, Z. Liu, C. Qiu, and J. Shi, “Metamaterial with Simultaneously Negative Bulk Modulus and Mass Density”, *Phys. Rev. Lett.* 99, 093904 (2007).

<sup>8</sup> N. Fang, D. J. Xi, J. Y. Xu, M. Ambrati, W. Sprituravanich, C. Sun, and X. Zhang, “Ultrasonic Metamaterials with Negative Modulus”, *Nat. Mater.* 5, 452 (2006).

<sup>9</sup> J. B. Pendry, D. Schurig, D. R. Smith, “Controlling Electromagnetic Fields”, *Science* 312, 1780 (2006)

<sup>10</sup> U. Leonhardt, “Optical Conformal Mapping”, *Science* 312, 1777 (2006).

<sup>11</sup> D. Schurig et al, “Metamaterial Electromagnetic Cloak at Microwave Frequencies.”, *Science* 314, 977-980(2006)

<sup>12</sup> Milton G W, Briane M and Willis J R, “On cloaking for elasticity and physical equations with

---

a transformation invariant form”, *New J. Phys.* 8, 248 (2006)

<sup>13</sup> S. A. Cummer and D. Schurig, “One path to acoustic cloaking”, *New J. Phys.* 9, 45 (2007).

<sup>14</sup> Torrent D and Sánchez-Dehesa J, “Anisotropic mass density by two dimensional acoustic metamaterials”, *New J. Phys.* **10** 023004 (2008)

<sup>15</sup> Daniel Torrent and José Sánchez-Dehesa<sup>1</sup>, “Acoustic cloaking in two dimensions: a feasible approach”, *New J. Phys.* **10** 063015 (2008)

<sup>16</sup> M. Farhat et al, “Broadband Cylindrical Acoustic Cloak for Linear Surface Waves in a Fluid”, *Phy.Rev.Lett* 101, 134501 (2008)

<sup>17</sup> C.R. Fuller and F. J. Fahy, *Journal of Sound and Vibration* **81**(4), 501-518, (1982)

<sup>18</sup> H. LAMB, *Manchester Literary and Philosophical Society-Memoirs and Proceedings*, **42**(9), (1898)

## 2 ACOUSTIC TRANSMISSION LINE

### 2.1 Introduction

Recently, there is a new research field that is known under the generic term of metamaterials. Metamaterial refers to materials “beyond” conventional materials, which dramatically increased our ability to challenge our physical perception and intuition. The exponential growth in the number of publications in this area has shown exceptionally promising to provide fruitful new theoretical concepts and potentials for valuable applications.

The physical properties of conventional materials are determined by the individual atoms and molecules from which they are composed. There are typically billions of molecules contained in one cubic wavelength of matter. The macroscopic wave fields, either electromagnetic or acoustic wave, are averages over the fluctuating local fields at individual atoms and molecules. Metamaterials extend this concept by replacing the molecules with man-made structures, viewed as “artificial atoms” on a scale much less than the relevant wavelength. In this way the metamaterial properties described using effective parameters are engineered through structure rather than through chemical composition.<sup>1</sup> The restriction that the size and spacing of this structure be on a scale smaller than the wavelength distinguishes metamaterials from photonic/phononic crystals. Photonic/phononic crystal is another different class of artificial material with periodic structure on the same scale as the wavelength. Therefore photonic/phononic crystals usually have a complex response to wave radiation that cannot be

simply described by effective parameters .However, the structural elements which make up a metamaterial is not necessary periodic.

Metamaterial with negative refractive index and the application in superlens has initiated the beginning of this material research. Early in late 1960s, metamaterial was first proposed by Veselago for electromagnetic wave.<sup>2</sup> He predicted that a medium with simultaneous negative permittivity and negative permeability were shown to have a negative refractive index. The first experimental demonstration of metamaterial with negative refractive index is reported at microwave frequency. <sup>3,4</sup> This metamaterial composed of a cubic lattice of artificial meta-atoms with split ring resonators and metallic wires. However, metamaterial with negative index is not the only possibility. Most recent developments explore new realms of anisotropic metamaterial that can produce novel phenomena such as invisibility<sup>5,6,7</sup> and hyperlens. <sup>8,9</sup> Moreover, it is of great interest to extend the metamaterial concept to other classical waves, such as acoustic wave.<sup>10,11,12</sup> Since the analogy between light and sound waves, the electromagnetic and acoustic metamaterials have been sharing much same design freedom while there has been less headway on the experimental front of acoustic wave.

## **2.2 Locally Resonant Sonic Materials**

Locally resonant sonic materials, which are a major step towards acoustic metamaterial, are designed by including a resonant unit into the building block of phononic crystal. The key difference between this sonic material and phononic crystal is that the individual unit cell is in deep-subwavelength range compared with the resonant frequency, enabling effective properties

as mass density and bulk modulus to be assigned to this material. Although the static elastic modulus and density need to be positive to maintain stable structure, these dynamic effective acoustic properties are dispersive in nature and can turn negative at resonance. When the resonance-induced scattered field prevails over the incident fields in background, the volume change can be out of phase with applied dynamic pressure, implying negative bulk modulus. On the other hand, the acceleration can be out of phase with the dynamic pressure gradient, showing negative mass density effect. Liu<sup>13</sup> experimentally demonstrated the localized resonance structure by coating heavy spheres with soft silicon rubber and encasing the coated spheres in epoxy. Negative effective density was obtained due to a dipolar resonance at low sonic frequency. Those anomalous phenomena resulted from strong coupling of the traveling elastic wave in the host medium with the localized resonance rather than Bragg scattering. In the long wavelength limit, the effective medium approach can be employed to offer a good estimation and give an intuitive understanding of this complex system.<sup>14,15,16</sup> It was demonstrated that an acoustic metamaterial can possess simultaneous negative bulk modulus and mass density by combining two types of structural units. While the monopolar resonances give rise to the negative bulk modulus, the dipolar resonances lead to the negative mass density.<sup>17</sup>

### **2.3 Acoustic Circuits**

A close analogy can be established between the propagation of sound in pipes or chambers and electrical circuits. When the dimensions of the region in which the sound propagates are much

smaller than the wavelength, a lumped-parameter model is appropriate. The essential thing here is that the phase is roughly constant throughout the system. (Appendix F)

### 2.3.1 Acoustic Impedance of a Pipe

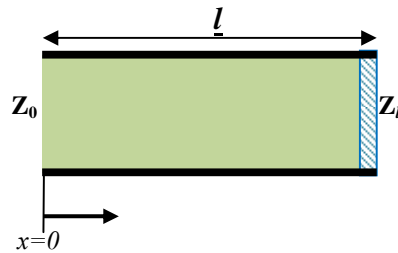


**Figure 2-1** A tube with rigid side wall terminated with acoustic impedance  $Z_l$

Assume a hollow cylindrical tube, open at one end and close another end with impedance  $Z_l$ . The origin of coordinates is chosen to be coinciding with the position of the open end of the tube. We shall assume the diameter of the tube is sufficiently small so that the waves travel down the tube with plane wave fronts. In order to make this true, the ratio of the wavelength of the sound wave to the diameter of the tube must be greater than about 6. If an initial wave traveling in the positive  $x$  direction  $p_{ai}$ , when the wave propagates at point  $x=l$ , a reflected wave traveling in the negative  $x$  direction will in general be produced  $p_{ar}$ , the corresponding particle velocity can be written as

$$v_i = v_{ai} e^{j(\omega t - kx)} \quad (2-1)$$

$$v_r = v_{ar} e^{j(\omega t + kx)} \quad (2-2)$$

Where  $v_{ai} = \frac{p_{ai}}{\rho_0 c_0}$ ,  $v_{ar} = -\frac{p_{ar}}{\rho_0 c_0}$

The total pressure in the tube at any point is

$$p = p_i + p_r \quad (2-3)$$

The total particle velocity is

$$v = v_i + v_r = \frac{p_i}{\rho_0 c_0} - \frac{p_r}{\rho_0 c_0} \quad (2-4)$$

So the general expression for the acoustic impedance includes the reflected wave is

$$Z_A = \frac{p}{Sv} = \frac{\rho_0 c_0}{S} \frac{p_{ai} e^{-jkx} + p_{ar} e^{jkx}}{p_{ai} e^{-jkx} - p_{ar} e^{jkx}} \quad (2-5)$$

So we know the impedance at  $x=0, l$  as

$$Z_{Al} = \frac{\rho_0 c_0}{S} \frac{p_{ai} e^{-jkl} + p_{ar} e^{jkl}}{p_{ai} e^{-jkl} - p_{ar} e^{jkl}} \quad (2-6)$$

$$Z_{A0} = \frac{\rho_0 c_0}{S} \frac{p_{ai} + p_{ar}}{p_{ai} - p_{ar}} \quad (2-7)$$

Combine (2-6) and (2-7), we can express the impedance at the open end  $x=0$  as a function of the impedance  $Z_{Al}$ ,<sup>18</sup>

$$Z_{A0} = \frac{\rho_0 c_0}{S} \frac{Z_{Al} + j \frac{\rho_0 c_0}{S} \tan kl}{\frac{\rho_0 c_0}{S} + j Z_{Al} \tan kl} \quad (2-8)$$

### 2.3.2 Acoustic Inductance

Consider the water in a tube of length  $l$  and area  $S$ . Assume the tube is acoustically rigid and open on both ends. Since all quantities are in phase when the dimension of the tube is much smaller than the corresponding wavelength, it moves as a whole with displacement under the action of an unbalanced force. The whole part moves without appreciable compression because of the open ends.

Substitute (2-8) with  $Z_{Al}=0$ ,<sup>19</sup>

$$Z_{A0} = j \frac{\rho_0 c_0}{S} \tan kl \quad (2-9)$$

Since  $l$  is much smaller than wavelength,  $kl = \frac{2\pi l}{\lambda}$  is a very small value, the tangent can be replaced by the Taylor series form,

$$\tan kl = kl + \frac{(kl)^3}{3} + \frac{2(kl)^5}{15} + \dots \quad (2-10)$$

Substitute (2-10) into (2-9) yields

$$Z_A = j\omega \frac{\rho_0 l}{S} + j \frac{\omega^3 \rho_0 l^3}{3Sc_0^2} + \dots \quad (2-11)$$

When  $l < \frac{\lambda}{16}$ , we can keep only the first term and neglect the higher order terms within about 5 per cent error. So we can define the acoustic inductance for an open end tube as

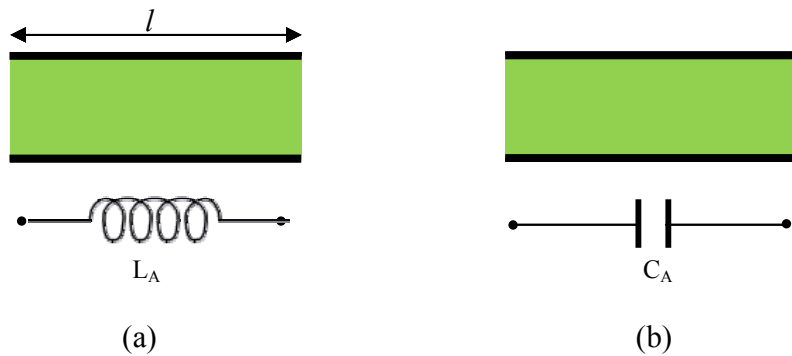


**Figure 2-2** A pipe with (a) open end and (b) rigid end is analogous to an acoustic inductor and acoustic capacitor respectively

$$L_A = j\omega \frac{\rho_0 l}{S} \quad (2-12)$$

As a result of the radiation impedance, the  $l$  in (2-12) should be replaced by an effective length of the tube added by a correction factor.  $l' = l + \frac{8a}{3\pi} = l + 0.85a$ , where  $a$  is the radius of the tube.

### 2.3.3 Acoustic Capacitance

If the tube is rigidly closed at one end, substitute  $Z_{Al} = \infty$  in (2-8) <sup>19</sup>

$$Z_{A0} = -j \frac{\rho_0 c_0}{S} \cot kl \quad (2-13)$$

For small value of  $kl$ , the cotangent can be replaced by the equivalent-series form

$$\cot kl = \frac{1}{kl} - \frac{kl}{3} - \frac{(kl)^3}{45} - \dots \quad (2-14)$$

Equation (2-13) becomes

$$Z_{A0} = -j \frac{1}{\omega \left( \frac{V}{\rho_0 c_0^2} \right)} + j\omega \frac{l\rho_0}{3S} + \dots \quad (2-15)$$

$Z_{A0}$  is valid within 5 percent for  $l$  up to  $\frac{\lambda}{8}$  series as a combination of an acoustic inductance and capacitance. Furthermore, if the second term is small enough, we may neglect it, such that the impedance of the cavity can be expressed as an acoustic capacitance.

$$C_A = \frac{V}{\rho_0 c_0^2} \quad (2-16)$$

### 2.3.4 Helmholtz Resonator

A typical Helmholtz resonator as in Figure 2-3 can be presented as a series of inductance and capacitance. The fluid inside the cavity is much easier to be compressed compared with that in the neck part. Moreover, the pressure gradient along the open neck is much greater than that inside the large cavity. Therefore the cavity displays capacitive property and leaves the smaller neck as an acoustic inductor.

## 2.4 Reflection and Transmission

When an acoustic wave traveling in one medium encounters the boundary of a second medium, reflected and transmitted waves are generated. For normal incidence, solids obey the same equations developed for fluids, which is greatly simplified. The only modification needed is that

the speed of sound in the solid must be the bulk speed of sound, relying on both bulk and shear module. The characteristic acoustic impedances and speeds of sound in two media and the angle of incident wave determine the ratios of the pressure amplitudes and intensities of the reflected and transmitted waves to those of the incident wave. For fluids, the characteristic acoustic impedance is defined as  $R = \rho c$ .

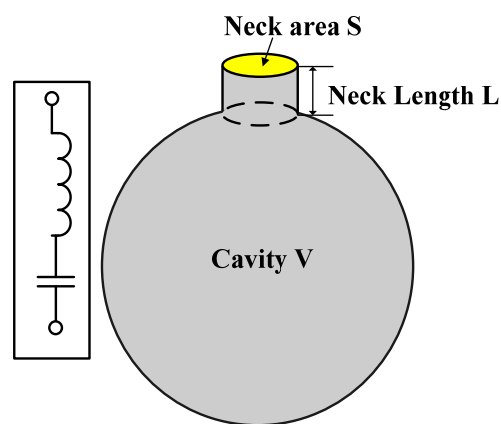


**Figure 2-3** Helmholtz resonator

### 2.4.1 Normal Incidence

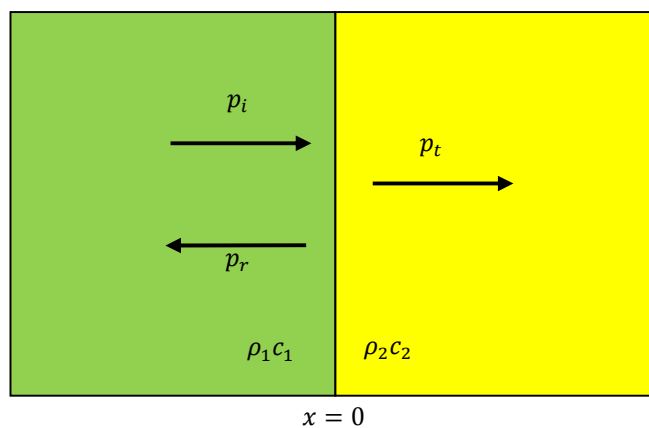


**Figure 2-4** Normal incidence

Let the boundary  $x = 0$  be the boundary between two fluids with characteristic acoustic impedance  $\rho_1 c_1$  and  $\rho_2 c_2$ . A plane wave traveling in the  $+x$  direction,

$$p_i = p_{ia} e^{j(\omega t - k_1 x)} \quad (2-17)$$

when the incident wave strikes the boundary, generates a reflected wave and a transmitted wave

$$p_r = p_{ra} e^{j(\omega t + k_1 x)} \quad (2-18)$$

$$p_t = p_{ta} e^{j(\omega t - k_2 x)} \quad (2-19)$$

Where  $k_1 = \frac{\omega}{c_1}$ ,  $k_2 = \frac{\omega}{c_2}$ ,  $\omega$  is the angular frequency and  $c_1, c_2$  are the speed of sound.

The particle velocities are

$$u_i = u_{ia} e^{j(\omega t - k_1 x)} \quad (2-20)$$

$$u_r = u_{ra} e^{j(\omega t + k_1 x)} \quad (2-21)$$

$$u_t = u_{ta} e^{j(\omega t - k_2 x)} \quad (2-22)$$

$$u_{ia} = \frac{p_{ia}}{\rho_1 c_1}, u_{ra} = -\frac{p_{ra}}{\rho_1 c_1}, u_{ta} = \frac{p_{ta}}{\rho_2 c_2} \quad (2-23)$$

The boundary conditions require the continuity of pressure and the normal component of the particle velocities must be equal at both sides of the boundary. The first condition implies that there is no net force on the boundary plane separating the media. The continuity of the normal component of velocity requires that the media remain in contact.

So at  $x = 0$

$$p_{ia} = p_{ra} + p_{ta} \quad (2-24)$$

$$u_{ia} = u_{ra} + u_{ta} \quad (2-25)$$

Substitute (2-17)-(2-23) into (2-24) and (2-25), we can obtain the reflection and transmission coefficients.

$$r_p = \frac{p_{ra}}{p_{ia}} = \frac{R_2 - R_1}{R_2 + R_1} \quad (2-26)$$

$$r_u = \frac{u_{ra}}{u_{ia}} = \frac{R_1 - R_2}{R_1 + R_2} \quad (2-27)$$

$$t_p = \frac{p_{ta}}{p_{ia}} = \frac{2R_2}{R_1 + R_2} \quad (2-28)$$

$$t_u = \frac{u_{ta}}{u_{ia}} = \frac{2R_1}{R_1 + R_2} \quad (2-29)$$

Where  $R_1 = \rho_1 c_1, R_2 = \rho_2 c_2$

The acoustic intensity of a harmonic plane progressive wave is defined as  $I = \frac{p_a^2}{2\rho c}$ . The intensity reflection and transmission coefficients are calculated.

$$r_I = \frac{I_r}{I_i} = \left( \frac{R_2 - R_1}{R_2 + R_1} \right)^2 \quad (2-30)$$

$$t_I = \frac{I_t}{I_i} = 1 - r_I = \frac{4R_1 R_2}{(R_1 + R_2)^2} \quad (2-31)$$

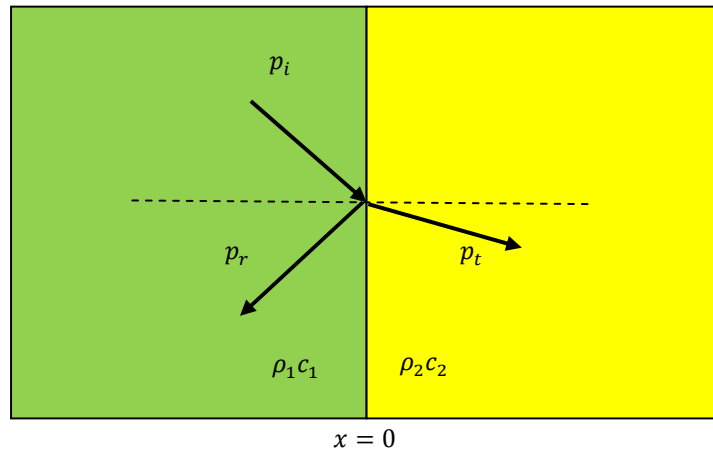


**Figure 2-5** Oblique incidence

In the limit when  $R_2 \gg R_1$ ,  $r_p \approx 1$ ,  $r_u \approx -1$ ,  $t_p \approx 2$ ,  $t_u \approx 0$ . The wave is reflected with amplitude equal to the incident wave and no change in phase. The transmitted wave has pressure amplitude twice that of the incident wave. The normal particle velocity of the reflected wave is equal to but  $180^\circ$  out of phase with that of the incident wave. Therefore the total normal particle velocity is zero at the boundary. The boundary with  $R_2 \gg R_1$  is termed rigid. In fact, such total reflection caused standing wave pattern in medium 1 and the boundary is the node for the particle velocity and antinode for the pressure. While there is no acoustic wave propagates in medium 2 since the particle velocity is zero and the pressure is static force. Given one example, the density and speed of sound of aluminum are  $2700\text{kg/m}^3$  and  $6420\text{m/s}$ . While the density and speed of sound of water is  $1000\text{ kg/m}^3$  and  $1500\text{m/s}$ . So the acoustic impedance of aluminum is around 12 times of that of water. Therefore when acoustic wave travels through water in an aluminum tube, the boundary can be assumed as rigid.

## 2.4.2 Oblique Incidence

Assume that the incident, reflected and transmitted waves make the respective angles  $\theta_i$ ,  $\theta_r$ ,  $\theta_t$ .

$$p_i = p_{ia} e^{j(\omega t - k_1 x \cos \theta_i - k_1 y \sin \theta_i)} \quad (2-32)$$

$$p_r = p_{ra} e^{j(\omega t + k_1 x \cos \theta_r - k_1 y \sin \theta_r)} \quad (2-33)$$

$$p_t = p_{ta} e^{j(\omega t + k_2 x \cos \theta_t - k_2 y \sin \theta_t)} \quad (2-34)$$

$$u_i = -\frac{1}{\rho_1} \int \frac{\partial p_i}{\partial x} dt = \frac{\cos \theta_i}{\rho_1 c_1} p_i \quad (2-35)$$

$$u_r = -\frac{1}{\rho_1} \int \frac{\partial p_r}{\partial x} dt = -\frac{\cos \theta_r}{\rho_1 c_1} p_r \quad (2-36)$$

$$u_t = -\frac{1}{\rho_2} \int \frac{\partial p_t}{\partial x} dt = \frac{\cos \theta_t}{\rho_2 c_2} p_t \quad (2-37)$$

Continuity of pressure and normal component of particle velocity at  $x = 0$  yields

$$p_{ia} e^{-jk_1 y \sin \theta_i} + p_{ra} e^{-jk_1 y \sin \theta_r} = p_{ta} e^{-jk_2 y \sin \theta_t} \quad (2-38)$$

$$\frac{\cos \theta_i}{\rho_1 c_1} p_{ia} e^{-jk_1 y \sin \theta_i} - \frac{\cos \theta_r}{\rho_1 c_1} p_{ra} e^{-jk_1 y \sin \theta_r} = \frac{\cos \theta_t}{\rho_2 c_2} p_{ta} e^{-jk_2 y \sin \theta_t} \quad (2-39)$$

Since  $\frac{\cos \theta_i}{\rho_1 c_1} p_{ia} e^{-jk_1 y \sin \theta_i} - \frac{\cos \theta_r}{\rho_1 c_1} p_{ra} e^{-jk_1 y \sin \theta_r} = \frac{\cos \theta_t}{\rho_2 c_2} p_{ta} e^{-jk_2 y \sin \theta_t}$  (2-39) must be

true for all  $y$ , this means

$$\sin \theta_i = \sin \theta_r \quad (2-40)$$

$$\frac{\sin \theta_i}{c_1} = \frac{\sin \theta_t}{c_2} \quad (2-41)$$

Equation (2-41) is the statement of Snell's law

So (2-39) can be further simplified as

$$p_{ia} + p_{ra} = p_{ta} \quad (2-42)$$

$$\frac{\cos \theta_i}{\rho_1 c_1} p_{ia} - \frac{\cos \theta_r}{\rho_1 c_1} p_{ra} = \frac{\cos \theta_t}{\rho_2 c_2} p_{ta} \quad (2-43)$$

So the reflection and transmission coefficients are

$$r_p = \frac{p_{ra}}{p_{ia}} = \frac{R_2 \cos \theta_i - R_1 \cos \theta_t}{R_2 \cos \theta_i + R_1 \cos \theta_t} \quad (2-44)$$

$$t_p = \frac{p_{ta}}{p_{ia}} = \frac{2R_2 \cos \theta_i}{R_1 \cos \theta_i + R_2 \cos \theta_t} \quad (2-45)$$

Where  $R_1 = \rho_1 c_1$ ,  $R_2 = \rho_2 c_2$

Where the Snell's law reveals

$$\cos \theta_t = \sqrt{1 - \sin^2 \theta_t} = \left[ 1 - \left( \frac{c_2}{c_1} \right)^2 \sin^2 \theta_i \right]^{1/2} \quad (2-46)$$

If  $c_1 < c_2$  and  $\theta_i > \theta_c$ , define  $\sin \theta_c = c_1/c_2$ ,

$$\cos \theta_t = -j \left[ \left( \frac{c_2}{c_1} \right)^2 \sin^2 \theta_i - 1 \right]^{1/2} \quad (2-47)$$

$\cos \theta_t$  becomes pure imaginary. The transmitted pressure is

$$p_t = p_{ta} e^{-\gamma x} e^{j(\omega t - k_1 y \sin \theta_i)} \quad (2-48)$$

$$\gamma = k_2 \left[ \left( \frac{c_2}{c_1} \right)^2 \sin^2 \theta_i - 1 \right]^{1/2} \quad (2-49)$$

The transmitted pressure field decays perpendicular to the boundary and propagates in the  $y$  direction, parallel to the boundary. For incident angle greater than the critical angle, the incident wave is totally reflected and in the steady state, no energy propagates away from the boundary into the second medium. Even though the transmitted wave possessed energy, but it propagates parallel to the boundary. As an example, the speed of sound in aluminum is greater than the one in water. As a result, as a plan wave propagates in water inside an aluminum tube and the incident angle in the solid/fluid interface is almost  $90^\circ$ , the wave is totally reflected from the aluminum and confined inside the water.

### 2.4.3 Reflection from the Surface of Solid

Define the normal specific acoustic impedance as

$$Z_n = \frac{p}{u \cdot \hat{n}} = \frac{p}{u \cos \theta} \quad (2-50)$$

Where  $\hat{n}$  is the unit vector perpendicular to the interface.

So the pressure reflection coefficient can be written as

$$r_p = \frac{p_{ra}}{p_{ia}} = \frac{\frac{R_2}{\cos \theta_t} - \frac{R_1}{\cos \theta_i}}{\frac{R_2}{\cos \theta_t} + \frac{R_1}{\cos \theta_i}} = \frac{Z_{n2} - Z_{n1}}{Z_{n2} + Z_{n1}} \quad (2-51)$$

Solids can support two types of elastic waves: longitudinal and shear. If the transverse dimensions of an isotropic solid are much larger than the wavelength of the acoustic wave, the appropriate phase speed for the longitudinal waves is

$$c = \sqrt{\frac{B + \frac{4}{3}S}{\rho}} \quad (2-52)$$

Where  $B$  and  $S$  are bulk and shear modulus of the solids and  $\rho$  is the density.

For the case of normal incidence, the transmission and reflection coefficient between solid and fluid is the same as those with two fluids interface. However, when plane wave obliquely incident on the surface of a solid, the wave transmitted into the solids might be refracted in three different cases. The wave may propagate along the surface of the solids. Another possibility is that the wave can propagate in a manner similar to two-fluid interface. Moreover, the wave may be converted into two waves, a longitude wave and a transverse wave.

For most solids, the normal specific acoustic impedance has two parts, resistance and reactance, respectively.  $z_n = r_n + jx_n$ . The pressure reflection coefficient can be revised as

$$r_p = \frac{p_{ra}}{p_{ia}} = \frac{\frac{R_2}{\cos \theta_t} - \frac{R_1}{\cos \theta_i}}{\frac{R_2}{\cos \theta_t} + \frac{R_1}{\cos \theta_i}} = \frac{\frac{r_{n2}}{\cos \theta_t} - \frac{r_{n1} + jx_{n2}}{\cos \theta_t}}{\frac{r_{n2}}{\cos \theta_t} + \frac{r_{n1} + jx_{n2}}{\cos \theta_t}} \quad (2-53)$$

This means the reflected wave at the boundary may either lead or lag the incident wave by certain angle. When  $\theta_i \rightarrow 90^\circ$ ,  $r_p$  approaches unity.

## 2.5 Absorption and Attenuation of Sound in Pipe

The previous sections are under the assumption that all losses of acoustic energy could be neglected. There are two kinds of loss in acoustic wave. The first source is associated with the boundary conditions and the other type of loss is intrinsic to the medium. The losses in the medium can be further subdivided into three basic types: <sup>20</sup> viscous losses, heat conduction losses and losses associated with internal molecular processes. Viscous losses occur when there is relative motion between adjacent portions of the medium. Heat conduction losses are caused by the conduction of thermal energy from high temperature condensations to lower temperature rarefactions. Losses resulted from molecular processes is by converting kinetic energy of the molecular into stored potential energy, rotational and vibration energies and energies of association and dissociation between different ionic species and complexes in ionized solutions. On the other hand, the loss due to the boundary is more significant when the volume of the fluid is small in comparison with the area of the walls, as when the pipe is narrow. The acoustic velocity amplitude increases from zero at the wall to the maximum value in the center of the pipe. Therefore there exist dissipative forces due to the shearing viscosity of the fluid. In addition to these viscous losses, heat conduction between fluid and the solid wall also causes energy loss. Usually it was assumed that the condensations and rarefactions in fluid are adiabatic and resulting in temperature change. However, for solid wall, the temperature is nearly constant, thus causing the tendency for heat to be conducted from the fluid medium to the solid walls during condensation and vice versa during rarefaction. The heat transfer increases the entropy of the

whole system and thus dissipates acoustic energy. In addition to those losses, there is direct absorption of the acoustic energy from the fluid medium by the wall.

### 2.5.1 Intrinsic Absorption from Viscosity in Medium

Consider a nonlinear *Navier-Stokes* equation in the absence of external body forces<sup>20</sup>

$$\rho \left( \frac{\partial \vec{u}}{\partial t} + (\vec{u} \cdot \nabla) \vec{u} \right) = -\nabla p + \left( \frac{4}{3}\mu + \mu_B \right) \nabla(\nabla \cdot \vec{u}) - \mu \nabla \times \nabla \times \vec{u} \quad (2-54)$$

Where  $\mu$  and  $\mu_B$  are coefficient of shear and bulk viscosity respectively.  $\mu_B$  is zero in monatomic gases and finite in fluids. It measures the dissipation involving the conversions of energy between molecular motion, internal molecular states and structural potential energy states.  $\mu \nabla \times \nabla \times \vec{u}$  counts when turbulence, laminar flow, vorticity occurs. In linear acoustics, these are usually confined to small region near boundaries.

Assume linear acoustic wave

$$\nabla \cdot \vec{u} = -\frac{\partial s}{\partial t} \quad (2-55)$$

Where condensation  $s = \frac{\rho - \rho_0}{\rho_0}$ ,  $\rho$  is instantaneous density and  $\rho_0$  is equilibrium density.

And the adiabatic condition yields

$$p = \rho c^2 s \quad (2-56)$$

Substitute (2-56) (2-57) into (2-55) yields lossy acoustic wave equation

$$\left( 1 + \eta \frac{\partial}{\partial t} \right) \nabla^2 p = \frac{1}{c^2} \frac{\partial^2 p}{\partial t^2} \quad (2-57)$$

Where  $\eta$  is relaxation time and  $c$  is the thermodynamic speed of sound which is not necessarily the phase speed.

Assume harmonic vibration  $e^{j\omega t}$ , (2-58) can be further simplified into Helmholtz equation

$$\nabla^2 p + k^2 p = 0 \quad (2-58)$$

$$k = \beta - j\alpha = \left(\frac{\omega}{c}\right)/(1 + j\omega\eta)^{1/2} \quad (2-59)$$

Solve the absorption coefficient  $\alpha$  and phase velocity  $c_p$

$$\alpha = \frac{\omega}{c} \frac{1}{\sqrt{2}} \left[ \frac{\sqrt{1+(\omega\eta)^2}-1}{1+(\omega\eta)^2} \right]^{1/2} \quad (2-60)$$

$$c_p = \frac{\omega}{k} = c\sqrt{2} \left[ \frac{1+(\omega\eta)^2}{\sqrt{1+(\omega\eta)^2}+1} \right]^{1/2} \quad (2-61)$$

The solution to the wave equation for a plane wave traveling in the  $x$  direction is

$$p = P_0 e^{j(\omega t - kx)} = P_0 e^{-\alpha x} e^{j(\omega t - \beta x)} \quad (2-62)$$

The typical value for  $\eta$  is about  $10^{-12}$  for fluids. So  $\omega\eta \ll 1$  is valid for very large frequency range.

$$\alpha \approx \frac{1}{2} \frac{\omega}{c} \omega\eta = (\omega^2/2\rho c^3) \left(\frac{4}{3}\mu + \mu_B\right) \quad (2-63)$$

$$c_p \approx c \left(1 + \frac{3}{8} (\omega\eta)^2\right) \quad (2-64)$$

The absorption coefficient is proportional to the square of frequency and the phase velocity is function of frequency, so the propagation is dispersive.

The loss in fluids involved with bulk viscosity is caused by the structure relaxation. Water, for example, is assumed to be a two-state liquid. The normal state has lower energy and in the state of higher energy, the molecules have a more closely packed structure. In static state, at equilibrium most of the molecules are in the first energy state. However with incident compression wave, more molecules transfer from the first state with more open space to the more closely packed second state. The time delays in this process and in the reversal resulted in a relaxation dissipation of the acoustic energy. The structure relaxation can be taken into account by adding nonvanishing absorption coefficient of bulk viscosity. Direct measurement indicates

that  $\mu_B$  in water is around three times of . The absorption coefficient of water is measures as

$$\frac{\alpha}{f^2} = 25 \left( Np \cdot \frac{s^2}{m} \right)$$

## 2.5.2 Viscous Absorption in Pipes at a Rigid Wall

### *Approach I*

For moderately small pipe ( $a > 10 \sqrt{\frac{\mu}{\rho\omega}}$ ), a laminar motion exists throughout the cross section of the pipe, the velocity increases from zero at the wall to the maximum in the center. The velocity difference causes viscous forces between two adjacent layers of the fluid medium, given by

$$f = \mu S \frac{\partial u}{\partial r} \quad (2-65)$$

Where  $S$  is the cross section area and  $u$  is particle velocity.  $\mu$  is the coefficient of shear viscosity.  $\mu$  is a measure of the diffusion of momentum by molecular collisions between regions of the fluid possessing different net velocities, so it is manifested in producing absorption even in pure longitudinal motion. It is independent of frequency and depends only on temperature. Because the temperature fluctuations in acoustic propagation are very small,  $\mu$  can be assumed to be a function of the equilibrium temperauter. These viscous processes delay the system to reach equilibrium, during which the density and temperature of the fluid are changed by expansion or compression. These resulted in the conversion of acoustic energy to random thermal energy.

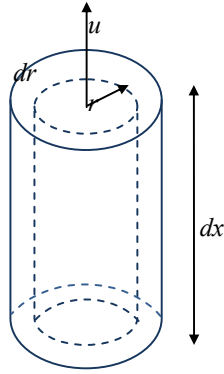


**Figure 2-6** Acoustic loss due to shear viscosity in pipes

Consider the fluid inside an annular ring of volume  $2\pi r dr dx$ , the net force by pressure gradient on such a ring is given by

$$-\frac{\partial p}{\partial x} dx \cdot 2\pi r dr \quad (2-66)$$

The net force on the annulus due to viscous force is

$$-\frac{\partial}{\partial r} \left( -\mu \cdot 2\pi r dx \frac{\partial u}{\partial r} \right) dr \quad (2-67)$$

By Newton's second law

$$\rho \frac{\partial u}{\partial t} 2\pi r dr dx = -\frac{\partial p}{\partial x} dx \cdot 2\pi r dr - \frac{\partial}{\partial r} \left( -\mu \cdot 2\pi r dx \frac{\partial u}{\partial r} \right) dr \quad (2-68)$$

Hence the equation of motion is

$$-\frac{\partial p}{\partial x} = \rho \frac{\partial u}{\partial t} - \frac{u}{r} \frac{\partial}{\partial r} \left( r \frac{\partial u}{\partial r} \right) \quad (2-69)$$

Assume harmonic wave motion  $p = P_A e^{j(\omega t - kx)}$ ,  $u = U_A e^{j(\omega t - kx)}$

So (2-70) can be simplified as

$$-\frac{\partial P_A}{\partial x} = \left( j\rho\omega - \frac{u}{r} \frac{\partial}{\partial r} \left( r \frac{\partial}{\partial r} \right) \right) U_A \quad (2-70)$$

Assume  $K = \sqrt{-\frac{j\rho\omega}{\mu}} = (1-j) \sqrt{\frac{\rho\omega}{2\mu}}$ , we can write (2-71) as

$$\frac{1}{\mu} \frac{\partial P_A}{\partial x} = \left( \frac{\partial^2}{\partial r^2} + \frac{1}{r} \frac{\partial}{\partial r} + K^2 \right) U_A \quad (2-71)$$

The solution of (2-72) is

$$U_A = \frac{\partial P / \partial x}{\mu K^2} + A J_0(Kr) \quad (2-72)$$

Where A is obtained by boundary condition that  $U_A = 0$  at  $r = a$ , so we have

$$U_A = \frac{\partial P / \partial x}{\mu K^2} + \left(1 - \frac{J_0(Kr)}{J_0(Ka)}\right) \quad (2-73)$$

The average velocity amplitude  $\bar{U}$  can be calculated

$$\bar{U} = \frac{\int_0^a 2\pi U r dr}{\pi a^2} = \frac{\partial P}{\mu K^2} \left(1 - \frac{2}{Ka} \frac{J_0(Kr)}{J_0(Ka)}\right) \quad (2-74)$$

If the radius of the pipe

$$a > 10 \sqrt{\frac{\mu}{\rho \omega}} \quad (2-75)$$

$$\frac{J_0(Kr)}{J_0(Ka)} \approx -j \quad (2-76)$$

and hence

$$1 - \frac{2}{Ka} \frac{J_0(Kr)}{J_0(Ka)} = 1 + j \frac{2}{Ka} \approx \left(1 - j \frac{2}{Ka}\right)^{-1} \quad (2-77)$$

Substitute (2-78) into (2-75), we obtain

$$-\frac{\partial P}{\partial x} = -\mu K^2 \left(1 - j \frac{2}{Ka}\right) \bar{U} = \left(j\rho\omega + \frac{2\rho\omega}{Ka}\right) \bar{U} = \left(j\rho\omega + \frac{\sqrt{2\mu\rho\omega}}{a}(1+j)\right) \bar{U} \quad (2-78)$$

So the effect of viscosity is to introduce an addition reactance term

$$j \frac{\sqrt{2\mu\rho\omega}}{a} = j\rho\omega \left(\frac{1}{a} \sqrt{\frac{2\mu}{\rho\omega}}\right) \quad (2-79)$$

And the resistance term

$$R = \frac{\sqrt{2\mu\rho\omega}}{a} \quad (2-80)$$

From (2-79) (2-80), we can write the effective density as

$$\rho' = \rho \left(1 + \frac{1}{a} \sqrt{\frac{2\mu}{\rho\omega}}\right) \quad (2-81)$$

So the effective velocity of wave propagation can be derived as

$$c' = c \sqrt{\frac{\rho'}{\rho}} \approx c \left(1 - \frac{1}{2a} \sqrt{\frac{2\mu}{\rho\omega}}\right) \quad (2-82)$$

Since

$$-\frac{\partial P}{\partial x} = \rho' c'^2 \frac{\partial^2 \bar{\xi}}{\partial x^2} \quad (2-83)$$

Where  $\bar{\xi}$  is the average particle displacement.

We can modify (2-83) in terms of  $\bar{\xi}$

$$\rho' c'^2 \frac{\partial^2 \bar{\xi}}{\partial x^2} = \rho' \frac{\partial^2 \bar{\xi}}{\partial t^2} + R \frac{\partial \bar{\xi}}{\partial t} \quad (2-84)$$

Solving this equation yields

$$\bar{\xi} = A e^{-\alpha x} e^{j(\omega t - k' x)} + B e^{\alpha x} e^{j(\omega t + k' x)} \quad (2-85)$$

Where  $\alpha = \frac{R}{2\rho' c'} \approx \frac{1}{ac} \sqrt{\frac{\mu\omega}{2\rho}}$  and  $k' = \frac{\omega}{c'}$

So the damping increases as frequency increases. For water, the viscosity is equal to 0.01g/cm, and density is 0.998g/cm<sup>3</sup>,  $\frac{\mu}{\rho} = 0.01 \text{ cm}^2/\text{sec}$

If the length of the pipe  $l$  is much smaller than wavelength, we can use (2-79) to derive the acoustic impedance.

$$\begin{aligned} Z &= \frac{\left(-\frac{\partial P}{\partial x}\right) l}{\bar{U} \pi a^2} = \left( j\rho\omega + \frac{\sqrt{2\mu\rho\omega}}{a} (1+j) \right) \frac{l}{\pi a^2} \\ &= \frac{\sqrt{2\mu\rho\omega}}{\pi a^3} l + j \left( \frac{\omega\rho l}{\pi a^2} + \frac{\sqrt{2\mu\rho\omega}}{\pi a^3} l \right) = R_v + j(X_M + X_v) \end{aligned} \quad (2-86)$$

Compare with the ideal case, the viscous forces caused modification of the impedance of the close end tube by an additional reactance term  $X_v = j \frac{\sqrt{2\mu\rho\omega}}{\pi a^3} l$  as well as an acoustic resistance  $R_v = \frac{\sqrt{2\mu\rho\omega}}{\pi a^3} l$ .

$$\frac{R_v}{X_M} = \frac{X_v}{X_M} = \frac{\frac{\sqrt{2\mu\rho\omega} l}{\pi a^3}}{\frac{\omega\rho l}{\pi a^2}} = \frac{\sqrt{\frac{2\mu}{\rho\omega}}}{a} \quad (2-87)$$

The above expressions are valid only for  $a > 10 \sqrt{\frac{\mu}{\rho\omega}}$ , the ratio  $\frac{R_v}{X_M}, \frac{X_v}{X_M}$  will not exceed  $\sqrt{2}/10$ . So the effect of viscosity can be neglected in this case with error within 10 per cent.

### **Approach II**

In a pipe with constant cross section, viscous loss can cause by shear at the boundary of the rigid wall. Consider a nonlinear *Navier-Stokes* equation (2-55) in the absence of external body forces. Assume lossless plane wave propagating along a rigid wall with boundary perpendicular to the constant phase front, we can neglect  $\left(\frac{4}{3}\mu + \mu_B\right)\nabla(\nabla \cdot \vec{u})$  which is due to viscous loss in the bulk of fluid and has been discussed in Sec 2.5.1.

$$\rho \left( \frac{\partial \vec{u}}{\partial t} + (\vec{u} \cdot \nabla) \vec{u} \right) = -\nabla p - \mu \nabla \times \nabla \times \vec{u} \quad (2-88)$$

Assume acoustic plane wave exit in the positive  $z$  space, propagation along  $x$  direction. With  $\mu = 0$ , the wave has particle velocity  $u$  and pressure as function of  $x, t$  only. The presence of rigid wall in the region  $z \leq 0$  with its boundary at  $z = 0$  introduces an additional wave component  $u'$  as function of  $x, z, t$ . The total particle velocity  $u_t$  near the boundary of the rigid wall should be zero because of viscosity. Furthermore,  $u'$  should vanish at large  $z$ .

$$u' = -u \quad \text{at } z = 0 \quad (2-89)$$

$$u' = 0 \quad \text{at } z \rightarrow +\infty \quad (2-90)$$

Substitute  $u_t \hat{x} = (u + u') \hat{x}$  into (2-90) and consider  $\nabla \times (u \hat{x}) = 0$

$$\rho \frac{\partial u'}{\partial t} + \frac{\partial p'}{\partial x} = \mu \frac{\partial^2 u'}{\partial z^2} \quad (2-91)$$

$$\frac{\partial p'}{\partial y} = 0 \quad (2-92)$$

$$\frac{\partial p'}{\partial z} = \mu \frac{\partial^2 u'}{\partial x \partial z} \quad (2-93)$$

$p'$  is the pressure associated with  $u'$ . If we neglect  $\frac{\partial p'}{\partial x}$  which we will justify in the end

$$\rho \frac{\partial u'}{\partial t} = \mu \frac{\partial^2 u'}{\partial z^2} \quad (2-94)$$

The solution for this one-dimensional diffusion equation for frequency dependence  $e^{j\omega t}$

$$u' = -ue^{-(1+j)z/\delta_\mu} \quad (2-95)$$

$$\delta_\mu = \sqrt{2\mu/\rho\omega} \quad (2-96)$$

$\delta$  is the viscous penetration depth or acoustic boundary layer thickness.

$$u = U_0 e^{j(\omega t - kx)} \quad (2-97)$$

$$u' = -U_0 e^{-z/\delta_\mu} e^{j(\omega t - kx - \frac{z}{\delta_\mu})} \quad (2-98)$$

The viscosity near the boundary of the rigid wall caused an additional wave component which decay along  $z$  direction  $e^{-z/\delta_\mu}$ , also the wave vector has  $z$  component equal to  $\frac{1}{\delta_\mu}$ . From (2-93)

we can derive  $\frac{|\frac{\partial p'}{\partial x}|}{|\frac{\partial u'}{\partial t}|} = \frac{1}{2}(k\delta_\mu)^2$ , so we can neglect  $\frac{\partial p'}{\partial x}$  in the above derivation when

$$\delta_\mu \left( \sqrt{\frac{2\mu}{\rho\omega}} \right) \ll \lambda$$

The average particle velocity

$$\begin{aligned} \langle u \rangle &= \frac{u}{\pi a^2} \int_s (1 - e^{-\frac{(1+j)z}{\delta_\mu}}) dS \\ &= u \left( 1 - \frac{2\pi a}{\pi a^2} \int_0^\infty e^{-\frac{(1+j)z}{\delta_\mu}} dz \right) \\ &= u \left( 1 - 2 \frac{\delta_\mu}{a} \frac{1}{1+j} \right) \end{aligned} \quad (2-99)$$

The acoustic impedance of the fluid with the viscous boundary layer is

$$\begin{aligned} Z &= \frac{\left( -\frac{\partial p}{\partial x} \right) l}{\langle u \rangle \pi a^2} = \frac{j\omega \rho u l}{\pi a^2 u \left( 1 - 2 \frac{\delta_\mu}{a} \frac{1}{1+j} \right)} \\ &\approx \frac{\omega \rho l \delta_\mu}{\pi a^2 a} + j\omega \frac{\rho l}{\pi a^2} \left( 1 + \frac{\delta_\mu}{a} \right) \end{aligned}$$

$$= R_b + jM_b \quad (\delta \ll a) \quad (2-100)$$

Substitute  $\delta_\mu = \sqrt{\frac{2\mu}{\rho\omega}}$

$$Z = \frac{\sqrt{2\mu\rho\omega}}{\pi a^3} l + j \left( \frac{\omega\rho l}{\pi a^2} + \frac{\sqrt{2\mu\rho\omega}}{\pi a^3} l \right) \quad (2-101)$$

It was observed that we have obtained same impedance expression for a tube considering the viscosity loss by two different approaches. The acoustic elements has a acoustic resistance  $\frac{\omega\rho l}{\pi a^2} \frac{\delta_\mu}{a}$  resulted from viscous loss in the rigid wall boundary and the effective density of the fluid is increased as  $\rho' = (1 + \frac{\delta_\mu}{a})$ , occurring as the incensement in the acoustic inductance.

The power dissipated because of the viscous boundary layer can be interpreted as  $R_b \langle u \rangle^2$ . Integrating over one period  $T$  and averaging over a wavelength gives the average power density during one cycle of motion

$$P_w = \frac{1}{\lambda} \int_0^\lambda \int_0^T \rho\omega \frac{\delta_\mu}{a} \langle u \rangle^2 dt dx = \pi\rho U_0^2 \frac{\delta_\mu}{a} \quad (2-102)$$

And the total energy density of the propagation wave is

$$P = \frac{1}{2} \rho U^2 \quad (2-103)$$

The quality factor from viscous losses at the wall is defined as

$$Q = \frac{2\pi P}{P_w} = \frac{a}{\delta_\mu} = a\sqrt{\rho\omega/2\mu} \quad (2-104)$$

Also  $Q = \frac{\omega}{2\beta}$ ,  $\alpha \approx \frac{\beta}{\omega} k$ , so

$$\alpha_\mu \approx \frac{1}{ac} \left( \frac{\mu\omega}{2\rho} \right)^{1/2} \quad (2-105)$$

### 2.5.3 Thermal Conduction

Calculation of the absorption resulting from thermal conduction between the fluid and the isothermal walls of the pipe is quite straightforward. When the fluid is subjected to an acoustic

vibration, the temperature in compressed regions will be increased while the temperature in rarefied regions will be decreased. The kinetic energy of translation in fluid is proportional to the temperature. The molecules in region with higher temperature have greater kinetic energies that diffuse into the surrounding cooler regions through intermolecular collisions. As energy leaves the region, it is lost from the acoustic wave and converted into random thermal energy of molecular motion. When there is plane wave propagation along  $x$  direction through a lossless fluid in the pipe with equilibrium absolute temperature  $T_{eq}$  which can be found from the equation of state and the adiabat to be <sup>20</sup>

$$T = T_{eq} + T_{eq}(\gamma - 1)s \quad (2-106)$$

$$s = \frac{p}{\rho c^2} = \frac{U}{c} e^{j(\omega t - kx)} \quad (2-107)$$

The additional temperature  $T'$  must maintain equilibrium temperature  $T_{eq}$  at the pipe wall and go to zero for large distance  $z$  away from the wall. The behavior of the temperature in this boundary layer region is described by the diffusion equation

$$\frac{\partial T'}{\partial t} = \frac{\kappa}{c_p \rho} \frac{\partial^2 T'}{\partial z^2} \quad (2-108)$$

Where  $c_p$  is the specific heat at constant pressure [ $J/(kg \cdot K)$ ].  $\kappa$  is the thermal conductivity [ $W/(m \cdot K)$ ]. The above equation can be solved

$$T - T_{eq} = (1 - e^{-\frac{(1+j)z}{\delta_k}}) T_{eq}(\gamma - 1)s \quad (2-109)$$

$$\delta_k = \sqrt{2\kappa/c_p \rho \omega} \quad (2-110)$$

The change in thermal energy is related to the change in temperature,  $\Delta q$  is the gain in thermal energy of a unit volume of the fluid.

$$\frac{\Delta q}{\Delta t} = c_p \rho \frac{\partial T}{\partial t} \quad (2-111)$$

In the pipe of radius  $a$ , the wave is propagating along  $x$  direction, and the boundary layer damped quickly along  $z$  direction. The loss in the boundary layer from thermal conduction is

$$\int_V \frac{\Delta q}{\Delta t} dV = 2\pi a \frac{\kappa}{T_{eq}} \int_0^\lambda \int_0^\infty \left(\frac{\partial T}{\partial z}\right)^2 dz dx = -\frac{dE}{dt} \quad (2-112)$$

The absorption coefficient is defined as

$$-2\alpha_k c = \frac{dE}{dt} / E \quad (2-113)$$

The total acoustic energy is

$$E = \frac{1}{2} \rho U^2 \pi a^2 \lambda \quad (2-114)$$

So the absorption coefficient is calculated as

$$\alpha_k = \frac{1}{ac} (\gamma - 1) \left(\frac{\kappa \omega}{2\rho c_p}\right)^{1/2} \quad (2-115)$$

The skin depth for viscosity and thermal conduction are related by Prandtl number

$$\frac{\delta_\kappa}{\delta_t} = \sqrt{Pr} \quad (2-116)$$

So

$$\alpha_k = \frac{1}{ac} \frac{(\gamma-1)}{\sqrt{Pr}} \left(\frac{\mu \omega}{2\rho}\right)^{1/2} \quad (2-117)$$

Compared with (2-107)

We obtain the ratio of the two types of absorption coefficients

$$\frac{\alpha_\kappa}{\alpha_\mu} = \frac{(\gamma-1)}{\sqrt{Pr}} \quad (2-118)$$

## 2.5.4 Total Loss in a Pipe

The total absorption coefficient for wall losses is

$$\alpha_w = \alpha_\kappa + \alpha_\mu = \frac{1}{ac} \left( \frac{\mu\omega}{2\rho} \right)^{\frac{1}{2}} \left( 1 + \frac{(\gamma-1)}{\sqrt{Pr}} \right) \quad (2-119)$$

The presence of the viscous boundary layer also modifies the phase speed of the acoustic wave. As in (2-103), the viscosity not only resulted in a resistance term, but one reactance term. The effect is equivalent to the fluid having effectively greater density  $\rho_\mu = \rho(1 + \frac{\delta_\mu}{a})$ . For adiabatic compression, the acoustic velocity depends inversely on the square root of the density. The correction of the speed of sound for the viscous boundary layer

$$\frac{c_\mu}{c} = \sqrt{\frac{\rho_\mu}{\rho}} = 1 - \frac{1}{2} \frac{\delta_\mu}{a} = 1 - \frac{\alpha_\mu}{k} \quad (2-120)$$

Similar conclusions can be reached for the thermal boundary layer. The density corrected for temperature fluctuation is  $\rho_\kappa = \rho(1 + \frac{\delta_\kappa}{a})$ , and the attendant correction to the phase velocity is

$$\frac{c_\kappa}{c} = \sqrt{\frac{\rho_\kappa}{\rho}} = 1 - \frac{1}{2} \frac{\delta_\kappa}{a} = 1 - \frac{\alpha_\kappa}{k} \quad (2-121)$$

So the total corrected phase velocity caused by the rigid wall

$$\frac{c_w}{c} = \sqrt{\frac{\rho_w}{\rho}} = 1 - \frac{1}{2} \frac{\delta_w}{a} = 1 - \frac{\alpha_w}{k} \quad (2-122)$$

As  $\alpha_w$  is proportional to  $\sqrt{\omega}$ , and  $k$  is related to  $\omega$ , the speed of sound approaches the value in free field asymptotically.

$$Z = \frac{\sqrt{2\mu\rho\omega}}{\pi a^3} l + j \left( \frac{\omega\rho l}{\pi a^2} + \frac{\sqrt{2\mu\rho\omega}}{\pi a^3} l \right) \quad (2-123)$$

$$\delta_\kappa = \sqrt{2\kappa/c_p\rho\omega} \quad (2-124)$$

Additional attenuation can be caused by the heat conduction at the walls of the pipe.<sup>21</sup> The study based on the assumption that the layer of fluid in contact with the walls can have neither velocity nor change in temperature shows the effective kinematic coefficient of viscosity is

$$v = \frac{\mu'}{\rho'} = \frac{\mu}{\rho} \left( \left( 1 + \sqrt{\gamma} - \frac{1}{\sqrt{\gamma}} \right) \frac{\kappa}{c_p \mu} \right)^2 \quad (2-125)$$

## 2.6 Acoustic Isotropic Metamaterial

Because of the strong dispersion inherent to the resonant elements in the sonic material, the effective material property was only obtained in a narrow frequency range. In addition, such resonances led to undesired material absorption. In this thesis, a new approach was employed to build a two-dimensional acoustic metamaterial based on transmission line model<sup>22</sup>.

### 2.6.1 Isotropic Distributed Transmission Line

In an inviscid medium, the two-dimensional (2D) time harmonic acoustic wave equations are

$$\frac{\partial P}{\partial z} = -j\omega\rho u_z \quad (2-126)$$

$$\frac{\partial P}{\partial x} = -j\omega\rho u_x$$

$$\frac{\partial u_z}{\partial z} + \frac{\partial u_x}{\partial x} = -j\omega\beta P \quad (2-127)$$

Substitute (2-127) into (2-126) yields

$$\frac{\partial^2 P}{\partial x^2} + \frac{\partial P}{\partial z^2} + k^2 P = 0 \quad k = \pm\omega\sqrt{\beta\rho} \quad (2-128)$$

Where  $P$  is pressure,  $\mathbf{u}$  is particle velocity,  $\beta$  is compressibility,  $\rho$  is density and  $\mathbf{k}$  is propagation constant.

In electromagnetism, a dielectric medium can be modeled using distributed transmission network.<sup>23</sup> Similar analogy can be found between an acoustic system and a distributed network.

The basic unit cell in the transmission line is composed of distributed series impedances and

shunt admittances as shown in Figure 2-7. The 2D telegrapher's equation for the distributed structure can be expressed as

$$\frac{\partial V_y}{\partial z} = -ZI_z$$

$$\frac{\partial V_y}{\partial x} = -ZI_x \quad (2-129)$$

$$\frac{\partial I_z}{\partial z} + \frac{\partial I_x}{\partial x} = -YV_y \quad (2-130)$$

Substitute (2-130) into (2-129)

$$\frac{\partial^2 V_y}{\partial x^2} + \frac{\partial^2 V_y}{\partial z^2} + k^2 V_y = 0 \quad k = \pm\sqrt{-ZY} \quad (2-131)$$

where  $V_y$  is the voltage,  $I_x, I_z$  are the currents,  $Z$  is the impedance per unit length,  $Y$  is the admittance per unit length and  $k$  is propagation constant.

Comparison of the above two sets of equations shows that the distributed transmission network can be used to model acoustic medium properties by mapping voltage and current to the pressure and particle velocity respectively. In this analogy, the impedance  $Z$  in the transmission line describes the material density  $\rho$  and the admittance  $Y$  corresponds to the compressibility  $\beta$ .

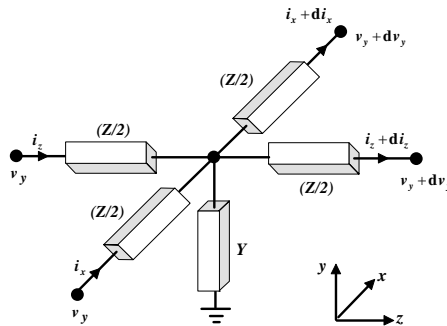


**Figure 2-7** Unit cell for a 2D isotropic distributed transmission line

## 2.6.2 Isotropic Acoustic Metamaterial Network

The distributed acoustic transmission line mentioned in previous section can be physically implemented by an acoustic lumped circuit network. An acoustic element can be predominantly of either capacitance or inductance nature, depending on the relative compressibility of the fluid inside the element. The building block in the acoustic transmission line for an effective medium with positive refractive index (PI) is shown in Figure 2-8 (a). In this structure, the channels connecting the cavity act as a series of acoustic inductors and the cavity as an acoustic capacitor.<sup>24</sup> On the other hand, the building block of the acoustic metamaterial with negative index (NI) is shown in Figure 2-8 (b). The channels are analogous to a series of acoustic capacitors while the through hole works as an acoustic inductor.<sup>25,26</sup>

Using the lumped circuit model, the propagation of acoustic wave through the PI network in Figure 2-8 (e) is described as

$$\begin{aligned}\frac{\partial P}{\partial z} &\approx \frac{P_{n+1,m} - P_{n-1,m}}{d_p} = -\frac{j\omega L_p U_z}{d_p} \\ \frac{\partial P}{\partial x} &\approx \frac{P_{n,m+1} - P_{n,m-1}}{d_p} = -\frac{j\omega L_p U_x}{d_p}\end{aligned}\quad (2-132)$$

$$\frac{\partial U_x}{\partial x} + \frac{\partial U_z}{\partial z} \approx \frac{U_{x,n,m+1} - U_{x,n,m}}{d_p} + \frac{U_{z,n+1,m} - U_{z,n,m}}{d_p} = -\frac{j\omega C_p P}{d_p}\quad (2-133)$$

Where  $P$  is pressure,  $U_x$   $U_z$  are  $x$  and  $z$  component of volume velocity,  $L_p$  and  $C_p$  are acoustic inductance and capacitance,  $d_p$  is the periodicity and  $\omega$  is angular frequency.

Compared the above equations with the microscopic sound wave equations (2-128) and (2-129), we can derive the effective density and compressibility as

$$\rho_{eff,P} = \frac{L_P S_P}{d_P} = \rho_w \frac{l_P}{d_P} \quad (2-134)$$

$$\beta_{eff,P} = \frac{C_P}{S_P d_P} = \frac{V_P}{\rho_w c_w^2 S_P d_P} \quad (2-135)$$

Where both effective density and compressibility are positive,  $\rho_w$  and  $c_w$  are the density and speed of sound of water. The geometry parameter  $l_P$  is the channel length,  $S_P$  is the cross section area of the channel and  $V_P$  is volume of the cavity as shown in Figure 2-8(c).

The corresponding propagation constant is

$$k_P = \frac{\omega \sqrt{L_P C_P}}{d_P} = \frac{\omega \sqrt{\frac{l_P V_P}{S_P c_w^2}}}{d_P} \quad (2-136)$$

The phase and group velocities are represented by

$$v_{\phi,P} = \frac{\omega}{k_P} = \frac{d_P}{\sqrt{L_P C_P}} = \frac{d_P}{\sqrt{\frac{l_P V_P}{S_P c_w^2}}}$$

$$v_{g,P} = \left( \frac{\partial k_P}{\partial \omega} \right)^{-1} = \frac{d_P}{\sqrt{L_P C_P}} = \frac{d_P}{\sqrt{\frac{l_P V_P}{S_P c_w^2}}} \quad (2-137)$$

Relative effective acoustic refractive index  $n_P$  can be determined as

$$n_P = \frac{c_w}{v_{\phi,P}} = \frac{c_w \sqrt{L_P C_P}}{d_P} = \frac{\sqrt{\frac{l_P V_P}{S_P}}}{d_P} \quad (2-138)$$

which is demonstrated to be positive.

Similarly, the propagation of acoustic wave in the NI networks in Figure 2-8 (f) are estimated as

$$\begin{aligned}\frac{\partial P}{\partial z} &\approx \frac{P_{n+1,m} - P_{n-1,m}}{d_N} = -\frac{U_z}{j\omega C_N d_N} \\ \frac{\partial P}{\partial x} &\approx \frac{P_{n,m+1} - P_{n,m-1}}{d_N} = -\frac{U_x}{j\omega C_N d_N}\end{aligned}\quad (2-139)$$

$$\frac{\partial U_x}{\partial x} + \frac{\partial U_z}{\partial z} = \frac{U_{xn,m+1} - U_{xn,m}}{d_N} + \frac{U_{zn+1,m} - U_{zn,m}}{d_N} = -\frac{P}{j\omega L_N d_N}\quad (2-140)$$

Where  $L_N$  and  $C_N$  are acoustic inductance and capacitance,  $d_N$  is the periodicity.

The effective density and compressibility are derived as

$$\begin{aligned}\rho_{eff,N} &= -\frac{S_N}{\omega^2 C_N d_N} = -\frac{S_N \rho_w c_w^2}{\omega^2 V_N d_N} \\ \beta_{eff,N} &= -\frac{1}{\omega^2 L_N d_N S_N} = -\frac{S_0}{\omega^2 \rho_w l_N d_N S_N}\end{aligned}\quad (2-141)$$

Both the effective density and compressibility are negative and function of frequency. The geometry parameter  $l_N$  is the length of the open hole,  $S_0$  is the cross section area of the open hole and  $S_N$  is the cross section area of the main channel as shown in Figure 2-8(d). The propagation constant is defined as

$$k_N = -\frac{1}{\omega d_N \sqrt{L_N C_N}} = -\frac{1}{\omega d_N \sqrt{\frac{l_N V_N}{S_0 c_w^2}}}\quad (2-142)$$

We found the phase and group velocity are

$$v_{\phi,N} = \frac{\omega}{k_N} = -\omega^2 d_N \sqrt{L_N C_N} = -\omega^2 d_N \sqrt{\frac{l_N V_N}{S_0 c_w^2}}$$

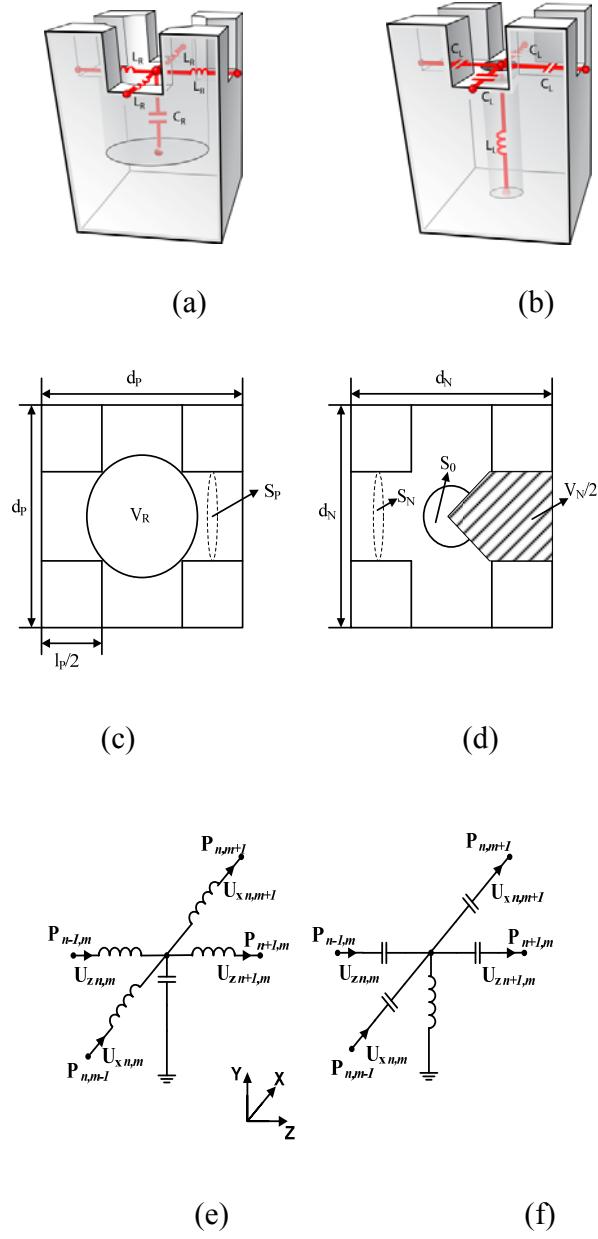


**Figure 2-8** The unit cell of (a) PI and (b) NI medium. The two-dimensional geometry of the unit cells in the (c) PI and (d) NI medium and corresponding lumped circuit in the (e) PI and (f) NI medium.

$$v_{g,N} = \left( \frac{\partial k_N}{\partial \omega} \right)^{-1} = \omega^2 d_N \sqrt{L_N C_N} = \omega^2 d_N \sqrt{\frac{l_N V_N}{S_0 c_w^2}} \quad (2-143)$$

The refractive index is calculated as

$$n_N = \frac{c_w}{v_{\phi,N}} = -\frac{c_w}{\omega^2 d_N \sqrt{L_N C_N}} = -\frac{c_w^2}{\omega^2 d_N \sqrt{\frac{L_N V_N}{S_0}}} \quad (2-144)$$

The negative root is chosen in equation (2-146) to guarantee a positive group velocity. From the above derivation, we found that an acoustic metamaterial with negative refractive index can be modeled by a series of capacitors with a shunt inductor.

## 2.7 Anisotropic Acoustic Metamaterial

Recently, a new design paradigm called conformal mapping and coordinate transformation has inspired a series of key explorations to manipulate, store and control the flow of energy, in form of either sound, elastic waves or light radiation. In electromagnetism, because of the coordinate invariance of Maxwell's equations, the space for light can be bent in almost arbitrary ways by providing a desired spatial distribution of electric permittivity  $\epsilon$  and magnetic permeability  $\mu$ .<sup>27,28</sup> Similar design approach can be applied to acoustic waves by a engineered space with desired distribution of effective density and compressibility.<sup>29,30,31</sup> A set of novel optical/acoustic devices were proposed based on transformation optics<sup>32,33,34,35</sup>; they usually call for complicated medium with anisotropic and spatially varying material parameter tensor to accomplish the desired functionality. Therefore, the 2D isotropic transmission line model is extended in this section to build an anisotropic acoustic metamaterial which promise potential application for a myriad of fascinating devices based on coordinate transformation.

### 2.7.1 Anisotropic Acoustic Distributed Transmission Line

In an inviscid medium, the two-dimensional (2D) time harmonic acoustic wave equations in a cylindrical coordinate are

$$\frac{\partial P}{r \partial \phi} = -j\omega \rho_{\phi} u_{\phi} \quad (2-145)$$

$$\frac{\partial P}{\partial r} = -j\omega \rho_r u_r$$

$$\frac{1}{r} \frac{\partial}{\partial r} (r u_r) + \frac{1}{r} \frac{\partial u_{\phi}}{\partial \phi} = -j\omega \beta P \quad (2-146)$$

Where  $P$  is pressure,  $\mathbf{u}$  is particle velocity,  $\beta$  is compressibility,  $\rho_r$ ,  $\rho_{\phi}$  is density along radial and angular direction respectively.

Assume an anisotropic transmission line in a cylindrical coordinate. The basic unit cell is composed of serial impedances and shunt admittances as shown in Figure 2-9. The 2D telegrapher's equation for the distributed structure can be expressed as

$$\frac{\partial V}{r \partial \phi} = -I_{\phi} Z_{\phi} \quad (2-147)$$

$$\frac{\partial V}{\partial r} = -I_r Z_r$$

$$\frac{1}{r} \frac{\partial}{\partial r} (r I_r) + \frac{1}{r} \frac{\partial I_{\phi}}{\partial \phi} = -V Y \quad (2-148)$$

Where  $V$  is the voltage,  $I_r$ ,  $I_{\phi}$  are the currents along  $r$  and  $\phi$  direction respectively,  $Z_r$ ,  $Z_{\phi}$  are the impedance per-unit length along radial and angular direction and  $Y$  is the admittance per-unit length.

Comparison of the above two sets of equations shows that the distributed transmission network can be used to model an anisotropic acoustic medium by mapping voltage and current to the pressure and particle velocity respectively. In this analogy, the impedance  $Z_r$ ,  $Z_{\phi}$  in the

transmission line describes the material density  $\rho_r$ ,  $\rho_\phi$  accordingly and the admittance  $Y$  corresponds to the compressibility  $\beta$ . This analog implies that we can model the cylindrical cloak with an inhomogeneous anisotropic transmission line by modifying the value of distributed impedance and admittance accordingly.

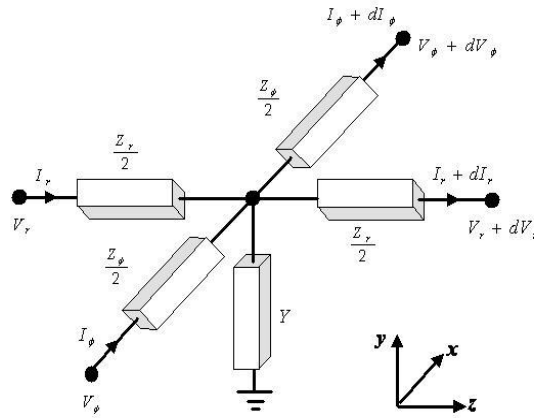


**Figure 2-9** Unit cell for a 2D anisotropic distributed transmission line

### 2.7.2 Anisotropic Acoustic Metamaterial Network

The anisotropic transmission line can be physically implemented by an acoustic lumped circuit network which consists of 2D array of the building blocks as shown in Figure 2-10. In each unit cell, the cavity with large volume in center works as an acoustic capacitor whereas the channels connecting to four neighboring cells act as serial inductors. The analogous inductor-capacitor (LC) circuit is shown in Figure 2-10 (b). This unit cell has the same topology as the one in PI isotropic medium. However, the unit cells here are positioned periodically along diagonal direction in a cylindrical coordinate. Moreover, the geometry of the unit cell is tuned individually to build an anisotropic effective acoustic medium. As the unit cell is much smaller

than the operational wavelength, the LC based circuit network is seen as effective medium by the acoustic waves. Based on the lumped circuit model, the propagation of the acoustic wave through the unit cell in Figure 2-10 (a) can be written as,

$$\frac{\partial P}{\partial r} \approx \frac{P_{n+1,m} - P_{n-1,m}}{\Delta r} = -\frac{j\omega L_r U_r}{\Delta r} \quad (2-149)$$

$$\frac{\partial P}{r \partial \phi} \approx \frac{P_{n,m+1} - P_{n,m-1}}{r \Delta \phi} = -\frac{j\omega L_\phi U_\phi}{r \Delta \phi}$$

$$\frac{1}{r} \frac{\partial}{\partial r}(r U_r) + \frac{1}{r} \frac{\partial U_\phi}{\partial \phi} \approx \frac{r_{n+1} U_{r,n+1,m} - r_n U_{r,n-1,m}}{r_n \Delta r} + \frac{U_{\phi,n,m+1} - U_{\phi,n,m-1}}{r_n \Delta \phi} = -\frac{j\omega C P}{\Delta r} \quad (2-150)$$

where  $U_r$ ,  $U_\phi$  are  $r$  and  $\phi$  component of volume velocity,  $L_r$  and  $L_\phi$  are acoustic inductance,  $C$  is acoustic capacitance and  $\omega$  is angular frequency.

Compared the above equations with the microscopic sound wave (2-149) and (2-150), we find the effective density and compressibility of the system interpreted as

$$\rho_{eff,r} = \frac{L_r S_r}{\Delta r} \quad \rho_{eff,\phi} = \frac{L_\phi S_\phi}{r \Delta \phi} \quad \beta_{eff} = \frac{C}{S_r \Delta r} \quad (2-151)$$

According to the definition of the acoustic inductance and capacitance

$$L_r = \rho_w \frac{l_r}{S_r} \quad L_\phi = \rho_w \frac{l_\phi}{S_\phi} \quad C = \frac{V}{\rho_w c_w^2} \quad (2-152)$$

Substitute (2-152) into (2-151) yields,

$$\rho_{eff,r} = \rho_w \frac{l_r}{\Delta r} \quad \rho_{eff,\phi} = \rho_w \frac{l_\phi}{r \Delta \phi} \quad \beta_{eff} = \frac{V}{\rho_w c_w^2 S_r \Delta r} \quad (2-153)$$

where  $\rho_w$  is the density of water and  $c_w$  is sound speed in water. The geometry parameters  $l_r$  and  $l_\phi$  are the channels length and  $S_r$  and  $S_\phi$  are the cross section area of the channels along  $r$  and  $\phi$  direction respectively.  $V$  is the volume of the large cavity. Equation (2-153) indicates the dependence of effective density and compressibility on the structure geometry

and filling medium which is water in the experiment. Therefore, this discrete network allows for a practical implementation of an anisotropic effective acoustic medium with spatial gradients by modifying the geometry and placement of the building blocks.

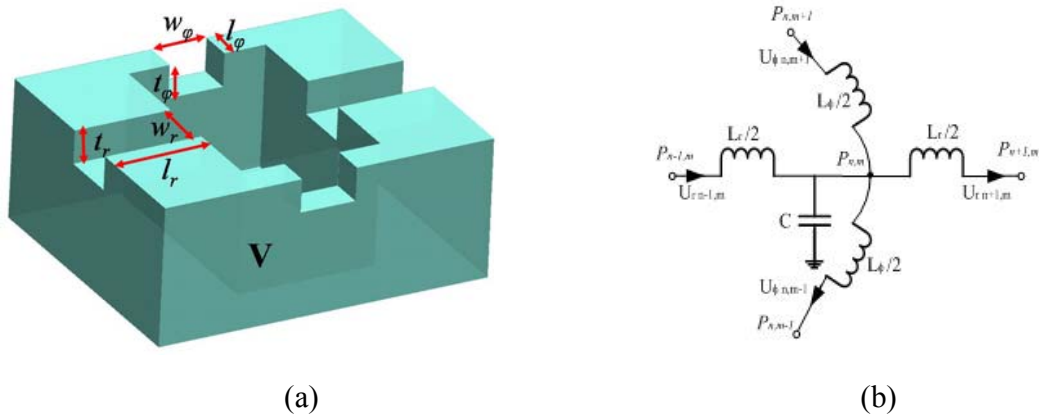


**Figure 2-10** (a) One unit cell for an anisotropic acoustic metamaterial and (b) the corresponding lumped circuit element.

## References

<sup>1</sup> J. B. Pendry, "Metamaterials and the Control of Electromagnetic Fields," *Proceedings of the Ninth Rochester Conference on Coherence and Quantum Optics* (2007).

<sup>2</sup> Veselago, V. G., "The electrodynamics of substances with simultaneously negative values of  $\mu$  and  $\epsilon$ ," *Sov. Phys. Usp.*, Vol. 10, No. 4, 509 (1968).

<sup>3</sup> Smith, D. R., et al., "Composite Medium with Simultaneously Negative Permeability and Permittivity", *Phys. Rev. Lett.* **84**, 4184–4187, (2000).

---

<sup>4</sup> Shelby, R. A., et al., "Experimental Verification of a Negative Index of Refraction", *Science* **292**, 77–79, (2001).

<sup>5</sup> J. B. Pendry, D. Schurig, D. R. Smith, "Controlling Electromagnetic Fields", *Science* **312**, 1780, (2006).

<sup>6</sup> U. Leonhardt, "Optical Conformal Mapping", *Science* **312**, 1777 (2006).

<sup>7</sup> D. Schurig et al, "Metamaterial Electromagnetic Cloak at Microwave Frequencies.", *Science* **314**, 977-980 (2006).

<sup>8</sup> Jacob, Z., Alekseyev, L. V. & Narimanov, E. "Optical hyperlens: Far-field imaging beyond the diffraction limit." *Opt. Express* **14**, 8247–8256 (2006).

<sup>9</sup> Z. Liu, H. Lee, Y. Xiong, C. Sun, X. Zhang, "Far-Field Optical Hyperlens Magnifying Sub-Diffraction-Limited Objects", *Science* **315**, 1686 (2007).

<sup>10</sup> N. Fang, D. Xi, J. Xu et al., "Ultrasonic metamaterials with negative modulus", *Nature Materials*, **5**,452-456 (2006).

<sup>11</sup> S. Zhang, L. Yin, and N. Fang, "Focusing Ultrasound with an Acoustic Metamaterial Network", *Phys. Rev. Lett.* **102**, 194301 (2009).

- 
- <sup>12</sup> J. Li, L. Fok, X. Yin, G. Bartal and X. Zhang, “Experimental demonstration of an acoustic magnifying hyperlens”, *Nature Materials* **8**, 931 - 934 (2009).
- <sup>13</sup> Z. Liu, X. Zhang, Y. Mao, Y. Y. Zhu, Z. Yang, C. T. Chan, and P. Sheng, “Locally Resonant Sonic Materials”, *Science* **289**, 1734 (2000).
- <sup>14</sup> V. Fokin, M. Ambati, C. Sun, and Xiang Zhang, “Method for retrieving effective properties of locally resonant acoustic metamaterials”, *Phys. Rev. B* **76**, 144302 (2007).
- <sup>15</sup> Z. Liu, C. T. Chan, and P. Sheng, “Analytic model of phononic crystals with local resonances”, *Phys. Rev. B* **71**, 014103 (2005).
- <sup>16</sup> Y. Wu, Y. Lai, and Z. Q. Zhang, “Effective medium theory for elastic metamaterials in two dimensions”, *Phys. Rev. B* **76**, 205313 (2007).
- <sup>17</sup> Y. Ding, Z. Liu, C. Qiu, and J. Shi, “Metamaterial with Simultaneously Negative Bulk Modulus and Mass Density”, *Phys. Rev. Lett.* **99**, 093904 (2007).
- <sup>18</sup> L. E. Kinsler, *Fundamentals of Acoustics*, 1982, Wiley, New York.
- <sup>19</sup> L.L.Beranek, *Acoustics*, 1954, McGRAW-HILL, New York.
- <sup>20</sup> Lawrence E. Kinsler, Austin R. Frey, Alan B. Coppens, and James V. Sanders, *Fundamentals of Acoustics*, 1999, Wiley, New York.

---

<sup>21</sup> R.D.Fay, *J.Acoust.Soc.Am.*, **12**,62, (1940).

<sup>22</sup> N. Fang, D. Xi, J. Xu et al., “Ultrasonic Metamaterials with Negative Modulus”, *Nature Materials*, **5**,452-456 (2006).

<sup>23</sup> A. Grbic, G. V. Eleftheriades’, “Overcoming the diffraction limit with a planar left-handed transmission-line lens”, *Phys. Rev. Lett.*, **92**, 117403 (2004).

<sup>24</sup> L.L.Beranek, *Acoustics*, 1954, McGRAW-HILL,New York.

<sup>25</sup> W. P. Mason, “A study of the regular combination of acoustic elements, with applications to recurrent acoustic filters, tapered acoustic filters, and horns”, *Bell Syst. Tech. J.* **6**, 258 (1927) .

<sup>26</sup> G. W. Stewart, “Acoustic wave filters”, *Phys.Rev.***20**, 528 (1922).

<sup>27</sup> Pendry J B, Schurig D and Smith D R ,” Controlling Electromagnetic Fields “, *Science* **312** ,1780 (2006).

<sup>28</sup> U. Leonhardt, “Optical Conformal mapping”, *Science* **312**, 1777 (2006).

<sup>29</sup> S. A. Cummer and D. Schurig, “One path to acoustic cloaking”, *New J. Phys.* **9**, 45 (2007).

<sup>30</sup> Cummer SA et al, “Scattering theory derivation of a 3D acoustic cloaking shell”, *Phys Rev Lett.* **100**, 024301(2008).

---

<sup>31</sup> Milton G W, Briane M and Willis J R, “On cloaking for elasticity and physical equations with a transformation invariant form”, *New J. Phys.* **8**, 248 (2006).

<sup>32</sup>A. V. Kildishev, V. M. Shalaev, “Engineering space for light via transformation Optics”, *Opt. Lett.* **33**, 43 (2008).

<sup>33</sup>M. Rahm, S. A. Cummer, D. Schurig, J. B. Pendry, “Optical Design of Reflectionless Complex Media by Finite Embedded Coordinate Transformations”, D. R. Smith, *Phys. Rev. Lett.* **100**, 063903 (2008).

<sup>34</sup> M. Rahm et al., “Transformation-optical design of adaptive beam bends and beam expanders”, *Opt. Express* **16**, 11555 (2008).

<sup>35</sup> Pendry J .B .and Li Jensen, “An acoustic metafluid: realizing a broadband acoustic cloak”, *New J. Phys.* **10** 115032 (2008).

### 3 ULTRASOUND FOCUSING USING ACOUSTIC METAMATERIAL NETWORK

#### 3.1 Introduction

High-resolution acoustic imaging techniques are the essential tools for nondestructive testing and medical screening. However, the spatial resolution of the conventional acoustic imaging methods is restricted by the incident wavelength of ultrasound. This is due to the quickly fading evanescent fields which carry the subwavelength features of objects. To overcome this diffraction limit, a remarkable perfect lens is proposed by John Pendry,<sup>1</sup> which offers the promise to build a device allowing super-resolution imaging of an object. This perfect lens is based on focusing the propagating wave and recovering the evanescent field through a flat negative-index slab. Since then research on metamaterials has been stimulated by the opportunity to develop artificial media that refract waves in negative direction. Several different metamaterials have been proposed and demonstrated to present negative index of refraction.

2,3,4,5,6

The successful demonstration of electromagnetic (EM) superlens<sup>7,8,9,10</sup> has inspired the search for the analogous acoustic negative-index lens. In fact, phononic crystals<sup>11,12,13,14,15</sup> were first investigated to develop negative-refractive devices for sound waves. Beam steering in phononic crystals can be achieved by Bragg scattering, leading to enhanced diffraction in negative direction. Ultrasound focusing from negative refraction by a three-dimensional phononic crystal was first demonstrated experimentally by Yang *et al.*<sup>13</sup> A focal spot around five

wavelengths in width was observed in the far field at 1.57 MHz. Recently, a finer resolution was achieved by focusing the ultrasound field emitted by a subwavelength line source using a two-dimensional (2D) phononic crystal slab.<sup>15</sup>

However, for lens design based on phononic crystals, the dependence of band structure on the lattice periodicity usually requires the spatial modulation to be the same order of magnitude as the acoustic wavelength, which would make such structure impractically large. Locally resonant sonic materials<sup>16</sup> made a major step towards the acoustic metamaterial development. Since the lattice constant is much smaller than the relevant wavelength, effective medium properties can be attributed to this sonic material at low frequency. With appropriate resonances included into the building block, acoustic metamaterials with either negative effective mass density or bulk modulus or both have been demonstrated.<sup>17,18,19,20</sup> These anomalous phenomena resulted from strong coupling of the traveling elastic wave in the host medium with the localized resonance in the building block. However, to the best of our knowledge, there is no experimental demonstration of focusing ultrasound waves in these negative index acoustic metamaterials.

In this section, we experimentally investigated the focusing of a point source from a designed ultrasonic metamaterial consisting of a planar network of subwavelength Helmholtz resonators. To facilitate the design, we adapted the 2D transmission line (TL) method which is widely used in the development of negative index EM metamaterials.<sup>8,9,10</sup> In this approach, the acoustic system is converted to an analogous lumped circuit model in which the motion of the fluid is equivalent to the behavior of the current in the circuit. Similar to permittivity and

permeability in the EM metamaterial,<sup>8</sup> the effective density and compressibility of the network structure are found to be related to the capacitance and inductance in this lumped circuit. Earlier, in the one-dimensional version of this ultrasonic metamaterial, the elastic modulus is found to be negative at specific frequency range theoretically and experimentally.<sup>21</sup>

### 3.2 Negative Refractive Index Lens

The refractive index is a fundamental parameter describing the interaction between waves and material. In late 1960s, Veselago<sup>22</sup> first considered the theoretical possibility for a medium having simultaneous negative permittivity and negative permeability. When  $\varepsilon(\omega) < 0, \mu(\omega) < 0$  at certain frequency, the refractive index is  $n = -\sqrt{\varepsilon\mu}$  and the negative sign is taken to satisfy causality. When light passes from a positive ( $n > 0$ ) to a negative ( $n < 0$ ) medium, Snell's law implies that the angle of refraction is negative, showing the refracted ray emerges on the same side of the normal as the incident ray .

In 2000, Pendry<sup>1</sup> proposed that a thin slab of metamaterial with negative refractive index could make a 'perfect lens' without any loss of details. A conventional lens cannot focus light onto an area smaller than a square wavelength due to the diffraction limit. The reason for this limit is that the evanescent waves which carries the subwavelength details of the object is exponentially decaying, leading to the loss of those fine features in the image. However, utilizing negative refractive index material, a 'perfect lens' can focus propagation waves and also amplify evanescent waves to generate subwavelength imaging.

As shown in Figure 3-1, negative refraction allows a flat slab lens of negative index to focus all the diverging light rays from an object into two images: one inside the slab and the other one outside the slab. The evanescent waves have been enhanced across the lens and decay again after emerging from the negative index lens. Therefore the amplitude at the two image planes reaches their original level. At the same time, the propagating waves pass through the negative index lens with a reversed phase front, leading to zero phase change at the image planes. By completely recovering both propagating and evanescent waves in phase and amplitude, a perfect image is obtained.

An approximation of the ‘perfect lens’ called as ‘super lens’ was built in optical frequency range under near-field condition. In the near field, since the electric and magnetic components are decoupled, the ‘super lens’ only needs negative dielectric permittivity for one polarization light. The optical superlensing effect on the scale of 60-nm ( $\lambda/6$ ) was observed by excitation of surface plasmons<sup>7</sup> through the metal/dielectric layer structure. The sub-diffraction-limited image was recorded by optical lithography at 365 nm wavelength.

In microwave frequency, subwavelength focusing was realized by different groups. One example is to use a planar transmission-line structure.<sup>10</sup> The negative index lens is a planar slab consisting of a grid of printed metallic strips over a ground plane, loaded with series capacitors and shunt inductors. In the experiment, the loaded grid is sandwiched between two unloaded printed grids that act as effective homogeneous media with a positive refractive index.

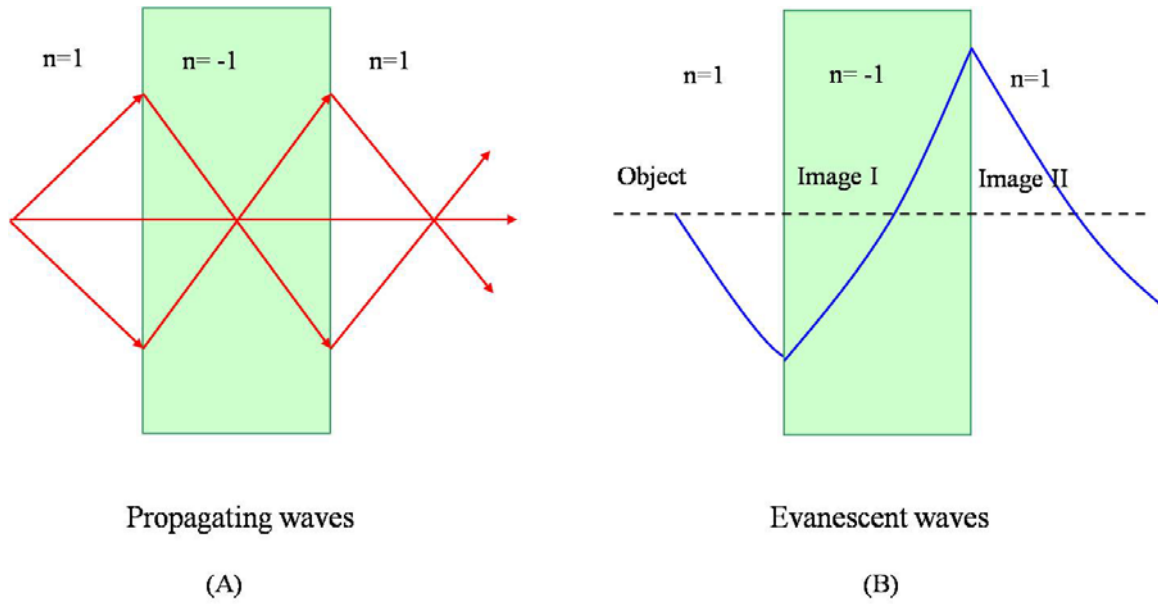


**Figure 3-1** (a) A flat lens brings all the diverging rays from an object into two focused images (b) the NI medium can enhance the evanescent waves across the lens, so the amplitude of the evanescent waves are identical at the object and the image planes.

### 3.3 Phononic Crystal

Great interest towards negative index material has been induced in phononic crystal study since Pendry proposed the ‘superlens’ idea in 2000. Phononic crystals are the acoustic or elastic analogue of photonic crystals (PC) for electromagnetic wave. It composes of periodic structure of different acoustic velocities and densities with lattice constants on the scale of the wavelength of sound (or ultrasound). Initially, phononic crystals attracted a lot of interest because of the exhibition of band gaps, over which wave propagation is forbidden due to Bragg scattering. Novel acoustic waveguide, sound insulators and filters have been proposed and demonstrated.

<sup>23,24,25,26,27</sup> The phononic crystals also have a rich variety of physical properties of interest to fundamental and applied research. There are longitudinal and transverse bulk waves as well as surface waves in phononic crystal, providing distinct advantages for studying propagation and scattering properties of classical waves.

In the low frequency region below first band gap, the phononic crystal is transparent to sound. The refractive acoustic devices have been proposed and demonstrated using phononic crystal in this frequency region when the wavelength is moderately long compared to the lattice constant. The Fabry-Perot-like interferometer and a converging lens made by periodic distributions of rigid cylinders in air have been physically realized and tested for airborne sound.<sup>28</sup> The acoustic focusing and imaging effect were numerically studied through lenslike phononic crystal device with a few wavelengths size.<sup>29,30</sup>

The negative refraction in the periodic crystal is achieved by the band-folding effect with locally positive material property ( $\mu, \epsilon$  for EM wave and  $\rho, E$  for acoustic and elastic wave), everywhere inside the crystal, which is fundamentally different from those in metamaterial with effective negative material property. The direction of power flow is given by the gradient vector  $\nabla_{\vec{k}} \omega(\vec{k})$  and thus negative refraction can be obtained because of anisotropy of crystal equifrequency contour or surface.

Negative refraction was first demonstrated in PC by employing the anisotropic shape of equifrequency surfaces (3D) or contours (2D) to achieve antiparallelism of vectors  $S$  (Poynting vector) and  $k$  (wave vector) ( $S \bullet k < 0$ ).<sup>31</sup> Furthermore, the negative refraction can also occur without negative index or backward wave effect ( $S \bullet k > 0$ ).<sup>32,33</sup> Luo *et al* studied the possibility to employ the convex equifrequency contours located at the corners of the first Brillouin zone in

the first band to achieve negative refraction in a 2D PC.<sup>15</sup> The superlensing effect was demonstrated experimentally by Cubukcu *et al* with a 2D PC made of a square array of dielectric rods in air. The refraction was achieved in the convex equifrequency contour in the first band. The full width at half maximum of the focus was  $0.21\lambda$  (where  $\lambda$  is the wavelength of the incident wave).<sup>34</sup>

Analogous phenomena are found in phononic crystal for acoustic wave. Outside the band gap, wave propagation in phononic crystals is strongly influenced by crystalline anisotropy, leading the group velocity, which represents the direction of energy transport by Bloch waves inside the crystal, no longer parallel to the wave vector.<sup>35</sup> In atomic crystals, analogous effects in phonon focusing have been extensively studied,<sup>36</sup> but experiments are limited to the long wavelength regime where  $\lambda \gg a$ .

Negative refraction of acoustic waves in two-dimensional (2D) phononic crystals<sup>37</sup> has been theoretically demonstrated in the first band resulted from equifrequency contours along the  $\Gamma M$  direction without employing the backward wave effect ( $S \cdot k > 0$ ) in a way similar to what is found in PC<sup>15</sup>. They numerically demonstrated the near-field imaging of a point source with the full width at half maximum of  $0.14\lambda$ , which overcomes diffraction limit. Far-field imaging by negative refraction through a 2D phononic crystal consisting of hexagonal arrays of steel cylinders in air are realized. The left-handed behavior  $S \cdot k < 0$  is found in the second band. The refractive index matches only with extremely high filling fraction, causing low transmission.<sup>38</sup> The ultrasound focusing phenomena result from negative refraction of a 3D phononic crystal was first demonstrated experimentally in 2004.<sup>39</sup> The negative refraction was achieved with source incident obliquely with respect to the [111] direction. Compared with the

field without lens, a focal spot around five wavelengths was observed in the far field at 1.57 MHz as presented. Ke *et al* reports experimental observation of focusing and negative refraction of acoustic wave in a 2D phononic crystal consisted of a triangular array of steel rods immersed in water. The circular equifrequency contour in the second band guaranteed the negative refraction for all incidence angles. Negative refraction was demonstrated by monitoring the transverse displacement of the sound beam transmitted through a flat phononic crystal with respect to the incident beam. The lateral resolution of the far-field image was found to be a couple of wavelength.<sup>40</sup> Recently, better resolution was observed experimentally with a similar 2D phononic crystal as in <sup>41</sup>by imaging a subwavelength line source which was positioned about half a wavelength away from the crystal surface. Prism-shaped phononic crystal was used to verify the negative refraction in the second band where the antiparallel directions of wave vector and group velocity were induced by the circular equifrequency contours.

In the above discussion, the negative refraction is induced due to the band-folding effect in the phononic crystal. The strongly modified dispersions resulted from Bragg scattering. The imaging conditions rely on appropriate intrinsic parameters of the chosen components in phononic crystal, such as the contrast of mass density and sound speed, the volume filling fraction, and the lattice structure. The dependence of band structure on the lattice periodicity usually requires the spatial modulation must be of the same order of magnitude as the sonic wavelength, which would make such structures impracticably large.

Another mechanism which can help to achieve negative refraction is local resonant structure. Negative effective mass density or elastic modulus can occur at certain frequencies if an appropriate resonance is included into the building block. Although the static elastic modulus and density need to be positive to maintain stable structure, these dynamic effective acoustic

properties are dispersive in nature and turn negative at resonance. When the resonance-induced scattered field prevails over the background incident field, the volume change can be out of phase with applied dynamic pressure, implying negative bulk modulus effect. And the acceleration is out of phase with the dynamic pressure gradient, showing negative mass density effect.<sup>42</sup> In 2000 Liu and colleagues<sup>43</sup> used localized resonance structure in a three-component phononic crystal to realize band gaps at low frequency with a lattice constant two orders of magnitude smaller than the relevant wavelength. Negative effective elastic modulus was realized due to a dipolar resonance at low sonic frequencies. Those anomalous phenomena resulted from strong coupling of the traveling elastic wave in the host medium with the localized resonance rather than Bragg scattering. In the long wavelength limit, it is more appropriate to call this “phononic crystal” as acoustic metamaterial since the lattice constant is much shorter than the acoustic wavelength of interest. Therefore the effective medium approach can be employed to offer a good estimation and give an intuitive understanding of this complex system.<sup>44,45</sup>

It was demonstrated that an acoustic metamaterial can possess simultaneously negative bulk modulus and mass density by combining two types of structural units. While the monopolar resonances give rise to the negative bulk modulus, the dipolar resonances give rise to the negative mass density.<sup>46</sup>

### **3.4 Ultrasound Focusing by Acoustic Transmission Line Network**

For lens design based on phononic crystals, the dependence of band structure on the lattice periodicity usually requires the spatial modulation to be the same order of magnitude as the acoustic wavelength, which would make such structure impracticably large. Locally resonant

sonic materials made a major step towards the acoustic metamaterial development. Since the lattice constant is much smaller than the relevant wavelength, effective medium properties can be attributed to this sonic material at low frequency. With appropriate resonances included into the building block, acoustic metamaterials with either negative effective mass density or bulk modulus or both have been demonstrated. These anomalous phenomena resulted from strong coupling of the traveling elastic wave in the host medium with the localized resonance in the building block. However, to the best of our knowledge, there is no experimental demonstration of focusing ultrasound waves in these negative index acoustic metamaterials. In this thesis, an acoustic lens with negative refractive index was implemented based on transmission line network for ultrasound focusing.

#### **3.4.1 Numerical Study of Acoustic Lens with Negative Refractive Index**

To study the ultrasound focusing by a negative index lens, a two-dimensional circuit model is simulated employing commercial software SPICE. The calculated lumped model is an approximation of the distributed acoustic system. The acoustic metamaterial with negative refractive index (NI) is composed by a two-dimensional (2D)  $50 \times 50$  periodic cascaded array of the unit cell as in Figure 3-2 (a). In order to build a PI/NI interface, an acoustic metamaterial with positive index (PI) is implemented by  $50 \times 50$  circuit cells as shown in Figure 3-2 (b). In the circuits, a very small resistance is connected to each inductor. The boundary of the

simulation model is grounded by a resistor with value equal to the characteristic impedance of the transmission line to reduce the reflection from the boundary.

Figure 3-3 (a) and (c) illustrates the normalized pressure magnitude and phase distribution of the sample at steady state when a continuous signal at 50 kHz is introduced at the center of the PI part [node (25, 25)]. The  $x$ - $y$  axes are labeled according to the cell number. The maximum field magnitude was normalized to unity. The focal point is expected around node (75, 25) since the relative index value equals  $-1$  at 50 kHz. Focusing is evident by the increased transmission and confinement of the fields near the focal plane [near node (75, 25)]. Therefore, a tight spot with central magnitude about  $-12$ dB is presented Figure 3-3 (a). Moreover, concavity waterfronts are observed in both NI and PI as evident in Figure 3-3 (c).

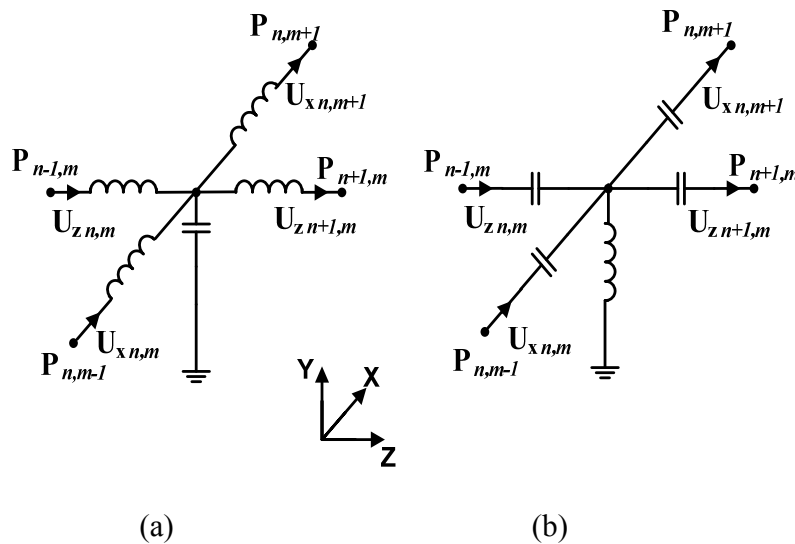
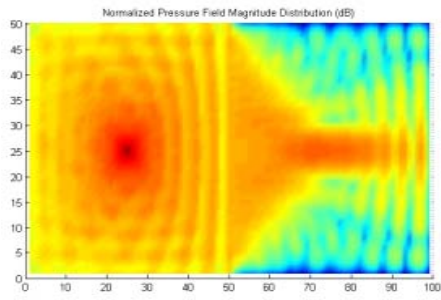
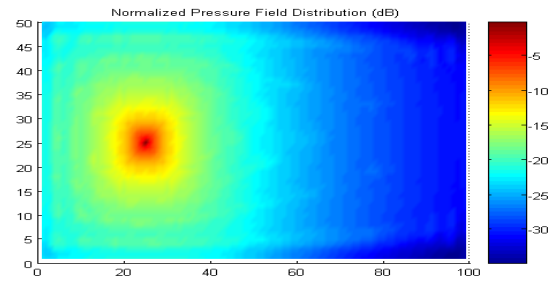


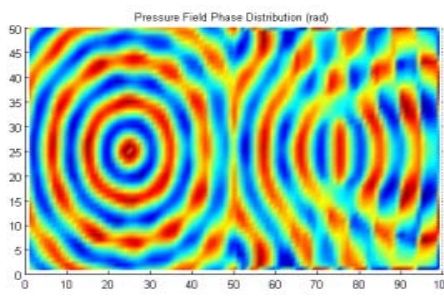
**Figure 3-2** Unit cells for acoustic metamaterial with (a) positive and (d) negative refractive index based on transmission line model



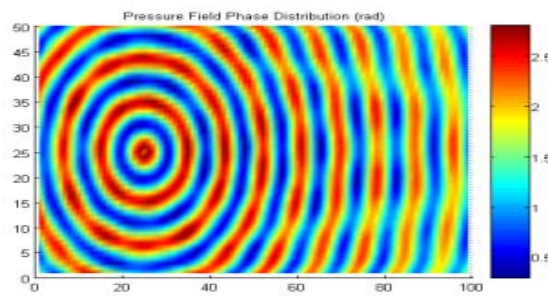
(a)



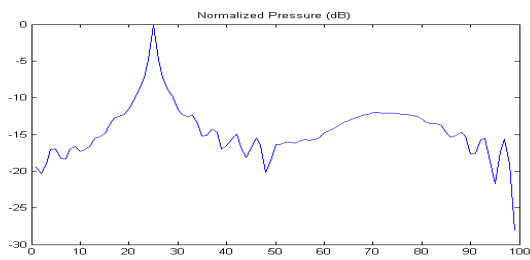
(b)



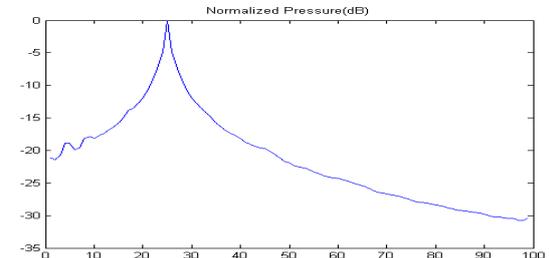
(c)



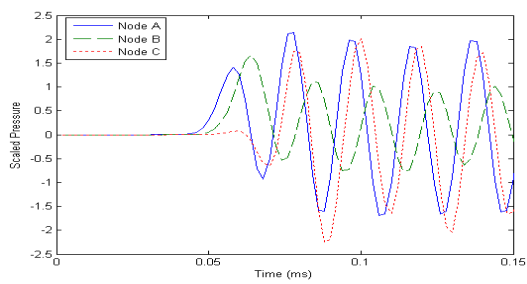
(d)



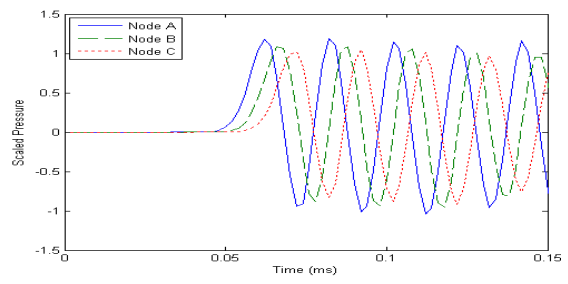
(e)



(f)



(g)



(h)

**Figure 3-3** Pseudo colormap of scaled pressure amplitude distribution due to a point source illuminating a 2D transmission model of the (a) PI/NI and (b) PI/PI interface. Phase distribution through (c) PI/NI and (d) PI/PI interface. Normalized pressure along the horizontal central line through the (e) PI/NI and (f) PI/PI interface model. Lineplot of scaled pressure on three nodes along the propagation direction in (g) PI/NI and (h) PI/PI interface.

The interface of PI/PI is also simulated as a comparison. The normalized pressure magnitude and phase distribution of the model is presented in Figure 3-3 (b) and (c). Away from the source, the cylindrical wavefront approaches plane wave fronts.

In Figure 3-3 (e) and (f), the pressure along the central line ( $y=25$ ) in the two cases are plotted respectively. In both plots, the source appeared as a peak with maximum value in node (25, 25). In the NI medium, a pressure magnitude peak around  $-12\text{dB}$  appear at (75, 25) while the pressure filed decays without no focusing in Figure 3-3 (f).

Figure 3-3 (g) and (h) shows the scaled pressure pulse as function of time at three different nodes A (45, 25), B (50, 25) and C (55, 25). In Figure 3-3 (g), compared with the pressure pulse at A, the one at B presents phase delay as result of longer distance from the source.

However, the pulse at C shows phase advance compared with the one at B even though C is further away from the point source. Therefore, the phase velocity is negative in the NI medium. However, in Figure 3-3(h), the comparison between three pulses clearly shows the advancement of the wave front when there is only PI medium.

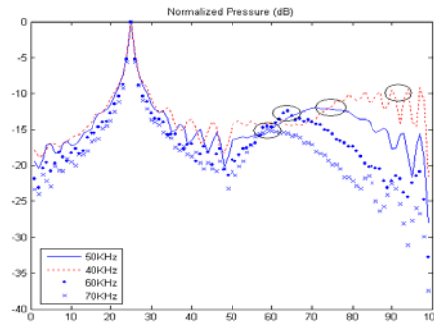
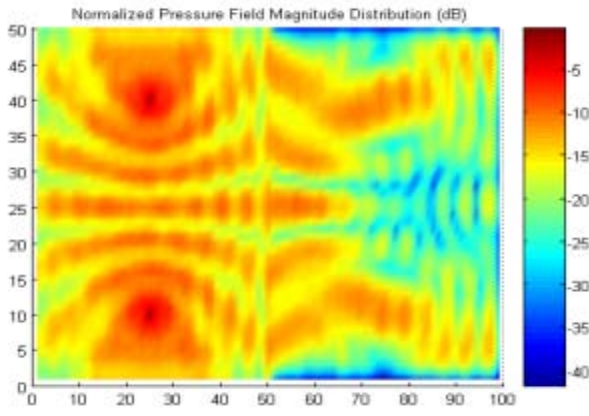


**Figure 3-4** Normalized pressure along the horizontal central line through the PI/NI interface model with source of different frequencies.

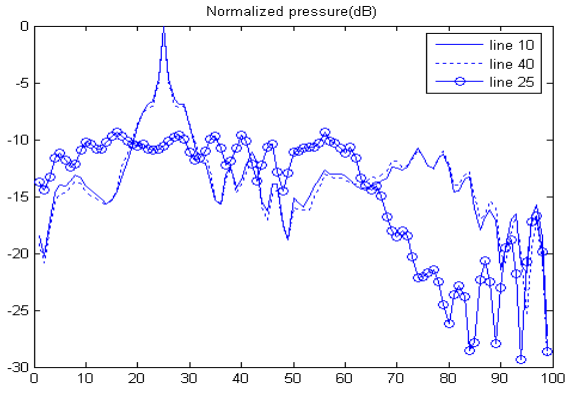
To investigate the influence of relative refractive index on focus property, a series of simulation are implemented at different frequencies. The normalized pressures along the central line through the source are plotted in Figure 3-4 with the source induced in the center of PI at node (25, 25).

At 50 kHz, the focusing point occurred at node (75, 25) in the center of the NI resulting from the index match. As frequency decreases to 40 kHz, the position of focus moves further away from the interface. On the other hand, at higher frequency 60 kHz and 70 kHz, the focus appears nearer to the interface.

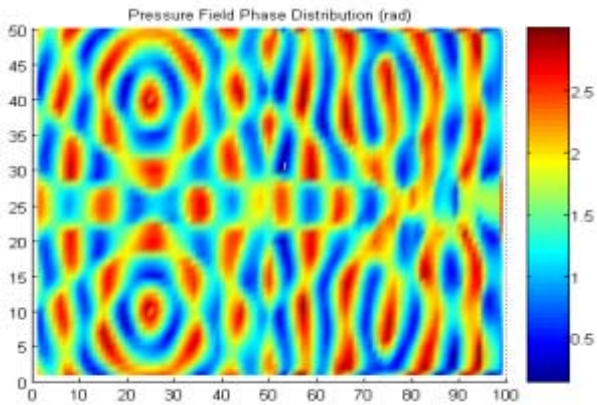
Owing to the flat interface, the vertical position of the source has no influence in the focusing mechanism. In order to demonstrate this property, the pressure field is calculated illuminated by two point sources. Two focuses are observed in Figure 3-5 (a). In Figure 3-5 (b), the line plots of the pressure field along horizontal direction present two peaks in amplitude



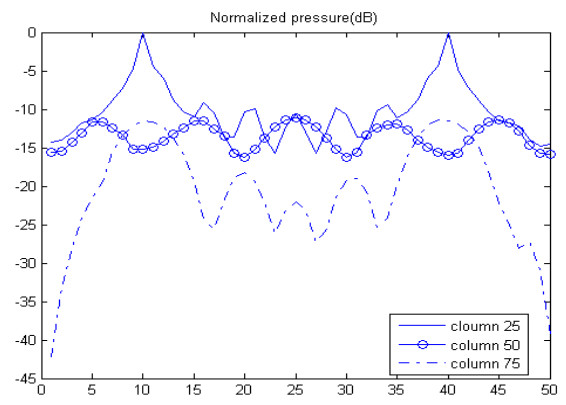
(a)



(c)



(b)



(d)

**Figure 3-5** Pseudo colormap of scaled pressure (a) amplitude and (b) phase distribution due to two point sources illuminating the 2D transmission line model of the PI/NI interface. Lineplot of pressure along three different (c) lines (d) and columns.

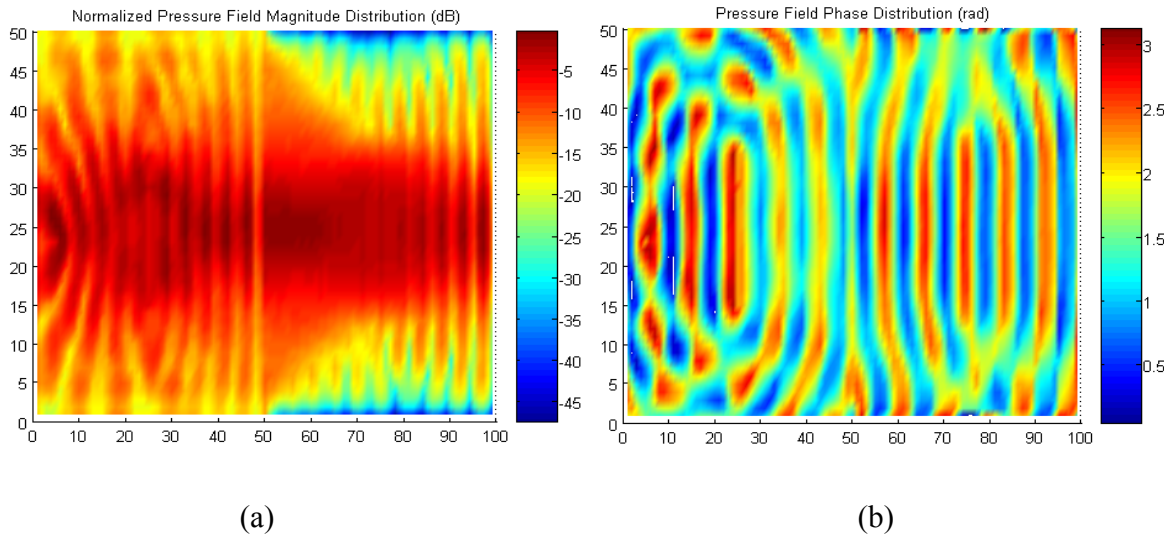


**Figure 3-6** Pseudo colormap of scaled pressure (a) amplitude and (b) phase distribution due to a beam sources illuminating the 2D transmission line model of the PI/NI interface

around column 75 corresponding to two focusing spots. In Figure 3-5 (d), the line plot shows the peak positions of the two sources and focuses along vertical direction. The open circles are the pressure at the PI/NI interface. The focusing points are observed in the same horizontal position as the corresponding sources due to the flat interface.

The imaging of a beam source by the negative index lens is also studied. The beam source is introduced by applying pressure field at ten nodes vertically in phase in the center of the PI part. In Figure 3-6 (a), the wave is convergent in the center of the NI part. In Figure 3-6 (b), phase distribution in the NI presents similar pattern as the one in the PI part.

## 3.4.2 Experimental Demonstration of Acoustic Lens with Negative Refractive Index

### 3.4.2.1 Experimental Setup and Data Acquisition

Figure 3-7 shows the experimental setup to study the focusing phenomena of the acoustic metamaterial. To prepare the sample, we machined a 2D array of periodically connected subwavelength Helmholtz resonators in an aluminum plate and the resonators are filled with water. As shown in previous work,<sup>47,48,49</sup> a main transmission channel with recurrent side branches, which are closed at the outer end, is analogous to a circuit of a series of inductors with shunt capacitors. On the other hand, when the side tubes inserted in the main channel is open on the outer end, the acoustic system can be described by a lumped network of a series of capacitors with shunt inductors. The left and right half parts in the sample are 2D periodic versions of those two different types of topology respectively. One unit cell from each half part is enlarged and shown in the two insets respectively.

The left half part is composed of a 2D array (40 by 40) of larger cavities connected with main channels. The volume of the cavity is around ten times of that of one section of the channels. Consequently, when an incident acoustic wave is applied onto the fluid in the channels, the pressure gradient through the channels is much greater than that inside the cavity. Hence, it is as if the fluid in the cavity were at rest relative to those in the channels.<sup>48</sup> So when the plug of fluid in the channels oscillates as a unit, there are adiabatic compressions and rarefactions of the fluid inside the larger cavity. Such an acoustic system is analogous to an inductor–capacitor

circuit as shown in the inset with the channels acting as a series of inductors ( $L_p$ ) and the cavity providing the stiffness element as capacitors ( $C_p$ ). The periodicity (3.175mm) of the sample is one-eighth of the wavelength at around 60 KHz frequency range. Table 3-1 shows the geometry of these two different unit cells. Given these values, the lumped circuit model is a valid approximation for the distributed acoustic system with only 10% error.<sup>50</sup> Following the approach of EM circuit analysis<sup>8,9,10</sup>, the effective density and compressibility of this network

can be expressed in the form as  $\rho_{eff,P} = \frac{L_p S_p}{d_p}$ ,  $\beta_{eff,P} = \frac{C_p}{S_p d_p}$ , where  $d_p$  is the periodicity,  $S_p$  is the cross section area of the channels. Both effective density and compressibility are positive.

Effective relative acoustic refractive index  $n_p$  can be determined by  $n_p = \frac{c_w \sqrt{L_p C_p}}{d_p}$ , where  $c_w$  is speed of sound in water. We call this half part as effective positive index medium.

The right half part of the sample is the dual configuration of the left half part, in which there is an array (40 by 40) of orifices connected with channels. The volume of one section of the main channel is designed as around ten times of that of the orifice. Since the fluid in the orifice is not confined, it experiences negligible compression while the fluid in the channels experience less movement in average compared with that in the orifice.<sup>48</sup> Consequently, when the fluid in the orifice oscillates as a unit, there are adiabatic compressions and rarefactions of the fluid inside the main channels. Such an acoustic system is described as a lumped network with a series of capacitors ( $C_N$ ) for the main channel part and a shunt inductor ( $L_N$ ) due to the orifice. The periodicity is the same as that in the left part, so the effective mass density and compressibility

can be similarly estimated as  $\rho_{\text{eff},N} = -\frac{S_N}{\omega^2 C_N d_N}$

$\beta_{\text{eff},N} = -\frac{1}{\omega^2 L_N d_N S_N}$ , where  $d_N$  is periodicity and  $S_N$  is the cross section area of connecting

channels. Both parameters are negative. The refractive index  $n_N = \frac{c_w}{v_\phi} = -\frac{c_w}{\omega^2 d_N \sqrt{L_N C_N}}$  is

negative. So this network structure acts as a medium exhibiting negative index (NI) of refraction.

The two half parts are designed with effective indices of equal and opposite value and matched impedance  $\sqrt{\rho_{\text{eff}} / \beta_{\text{eff}}}$  at the design frequency 60.5 kHz.

For experimental confirmation of ultrasound focusing in this acoustic metamaterial, we measured the pressure field through this PI/NI interface. The ultrasound waves were launched from a horn shaped transducer with a tip of 3 mm diameter in size. The tip is inserted into a hole drilled through the center of the PI part [(column, row) = (20, 20)] to illuminate the sample. A waveform generator (Tektronix AFG 310) is used to drive the transducer. The source generated a burst of sine waves with a width of 5 periods. To map the pressure field, a hydrophone was mounted on two orthogonal linear translation stages. By stepping the miniature hydrophone (RESON TC4038-1) to the positions above those through holes in the NI part and recording the pressure amplitude at every step, we acquired the spatiotemporal field distribution of the ultrasound wave focusing pattern. The pressure field is afterwards amplified by Stanford research systems model SR650 and captured using a digital

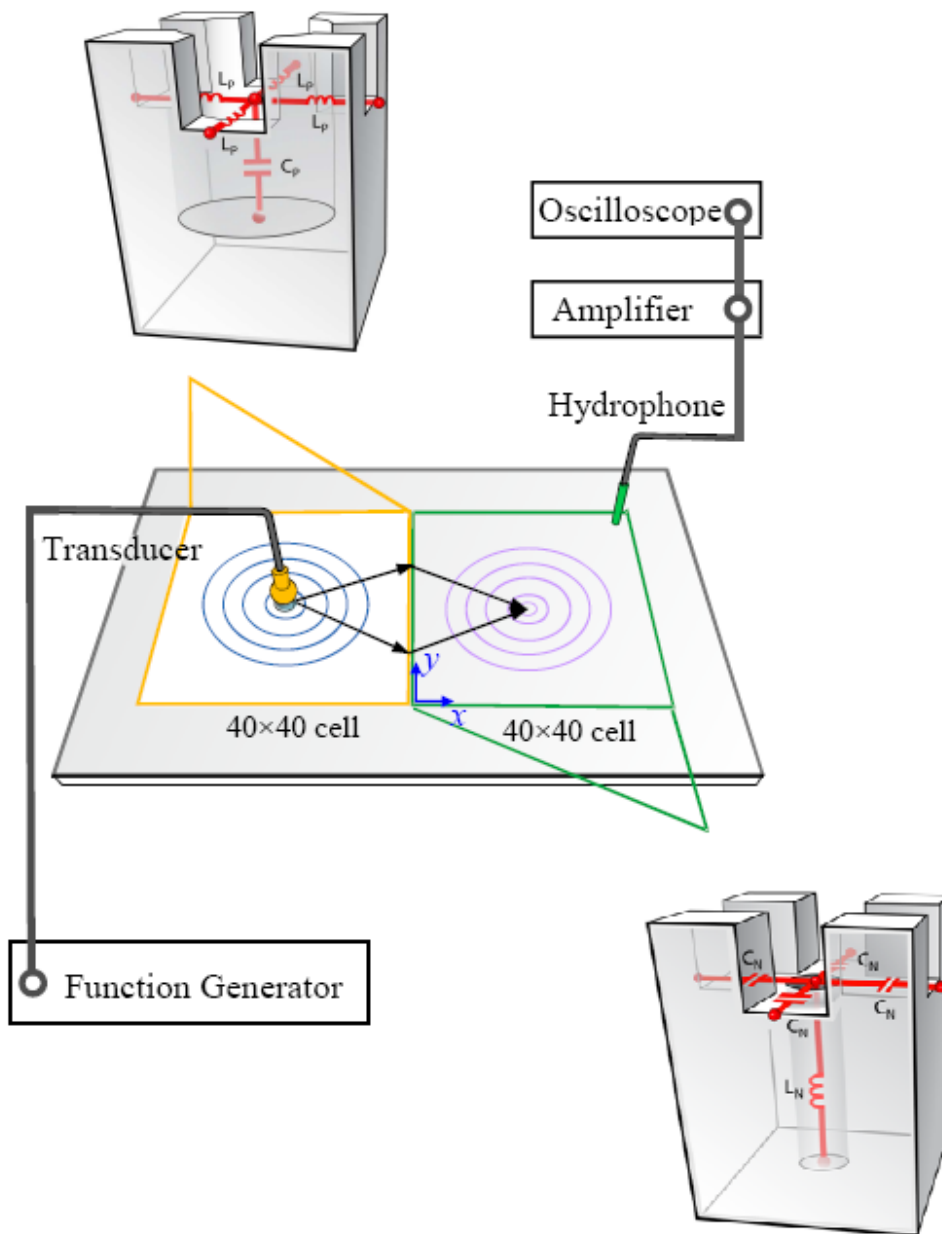


**Figure 3-7** Schematic showing the experimental setup. The sample with PI/NI interface is composed of an array of different designed Helmholtz resonators machined from an aluminum plate. A burst of monotonic signal with a width of five periods was used to drive the transducer as an underwater sound source in the center of the half part with positive index. One needle-sized

hydrophone detected the ultrasonic signals from the array of open holes in the negative index half part. Unit cells of each half part and the corresponding inductor–capacitor circuit analogy are shown in the insets. For the PI part in the top inset, the channels surrounding the cavity act as a series of acoustic inductors  $L_p$  and the cavity is a shunt capacitor  $C_p$ . The building block of the acoustic metamaterial in the bottom inset corresponds to a circuit with a series of acoustic capacitors  $C_N$  due to the channels and an acoustic inductor  $L_N$  due to the open hole in the middle

Table 3-1 Geometry parameters of the sample

	PI network	NI network
Periodicity (mm)	3.175	3.175
Cross-sectional area of the main channels (mm <sup>2</sup> )	1.23	4
Diameter of the through holes (mm)	N/A	1
Length of the through holes (mm)	N/A	0.96
Cavity Volume (mm <sup>3</sup> )	6.89	N/A

oscilloscope (Agilent DSO6104A) and then downloaded to a computer for post processing and analysis. The field pattern in the NI part at frequency of interest was obtained by Fourier transformation of the acquired pulse at each grid point, allowing the wave amplitude of each frequency component to be plotted as a function of position in the NI part. The limitations on the transducer working spectrum prevent us from probing the acoustic wave field below 60 kHz.

### 3.4.2.2 Results and Discussion

Figure 3-8 (a) shows the pressure field map in the NI part at 60.5 KHz with the PI/NI interface along  $x=0$ . The pressure amplitude is normalized to unity. A tight spot is observed in experiment as is evident from the plot. The pressure cross the focal plane along  $y$  direction is plotted in Figure 3-8 (c). The full width at half maximum (FWHM) was found to be 12.2mm, corresponding to a resolution of 0.5 wavelength in water.

For numerical verification, lumped circuit simulation of this acoustic network was performed by using commercial circuit simulator SPICE. Lumped circuit simulations were performed by using commercial circuit simulator SPICE to study the ultrasound focusing in this acoustic metamaterial network. The acoustic inductance and capacitance in the circuit are determined from the geometry of the sample. To match the experimental condition, the circuit model has the same unit cell number as the sample. A pulse of sine wave with a width of five periods is launched on the center of the PI part [(column, row) = (20, 20)] as in the experiment. A map of the field amplitude at each frequency of interest was obtained by Fourier transformation (FT) pulses at each nodes and reading the FT amplitudes. Comparison of Figure 3-8 (a) and (b) shows that the field plots found through simulation is in remarkable agreement with the experimental results. In Figure 3-8(c), the measured data in blue line is shifted to left by 3.175 mm for comparison purpose. The comparison demonstrates a very good match in the focus width between the measurement and the numerical simulation. In Figure 3-9, the measured

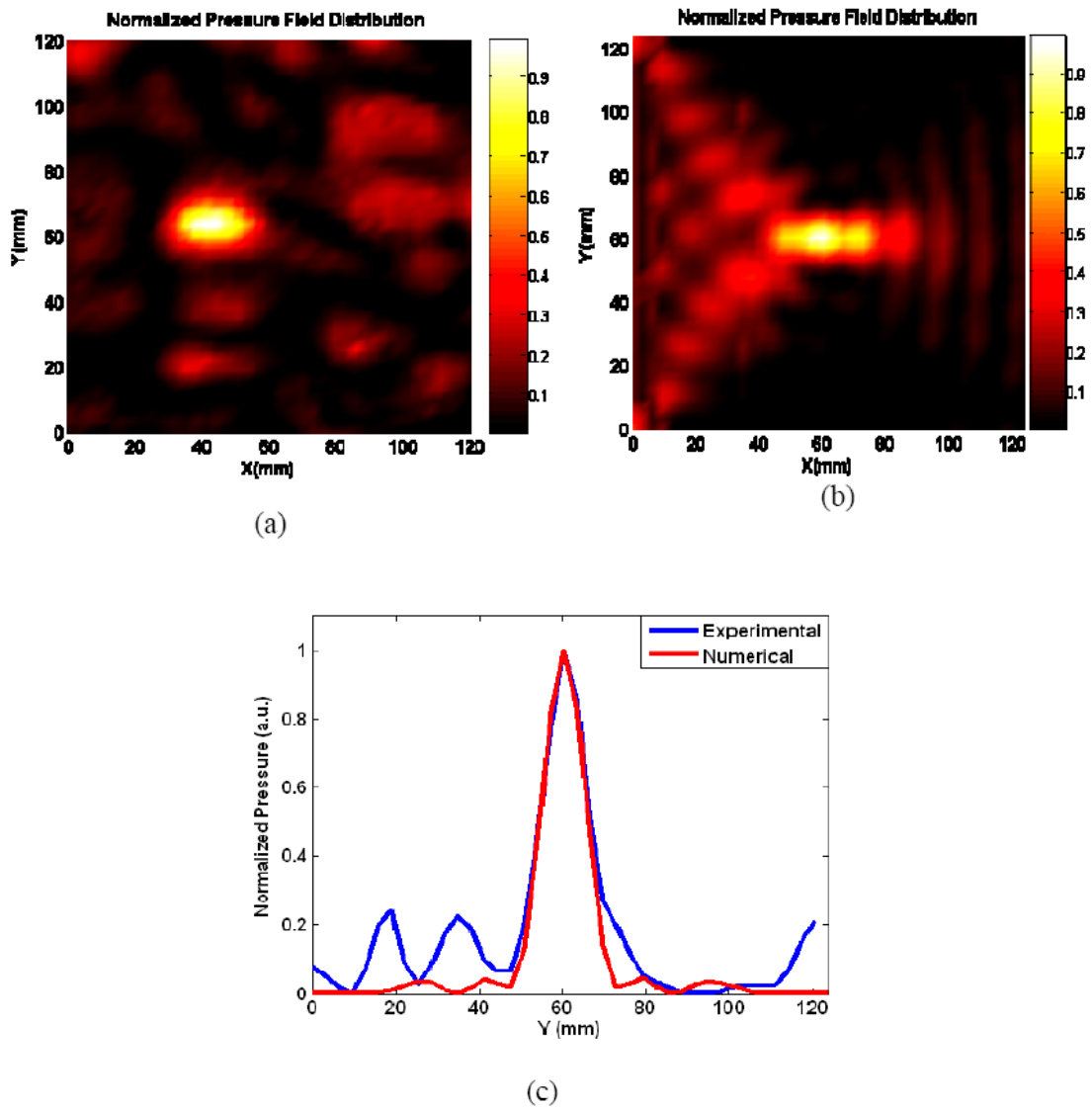


**Figure 3-8** Pseudo colormap of the normalized pressure field distribution at 60.5 KHz. (a) Measured and (b) simulated field map of the acoustic NI metamaterial and (c) Line plot of pressure field cross the focal plane parallel to interface.

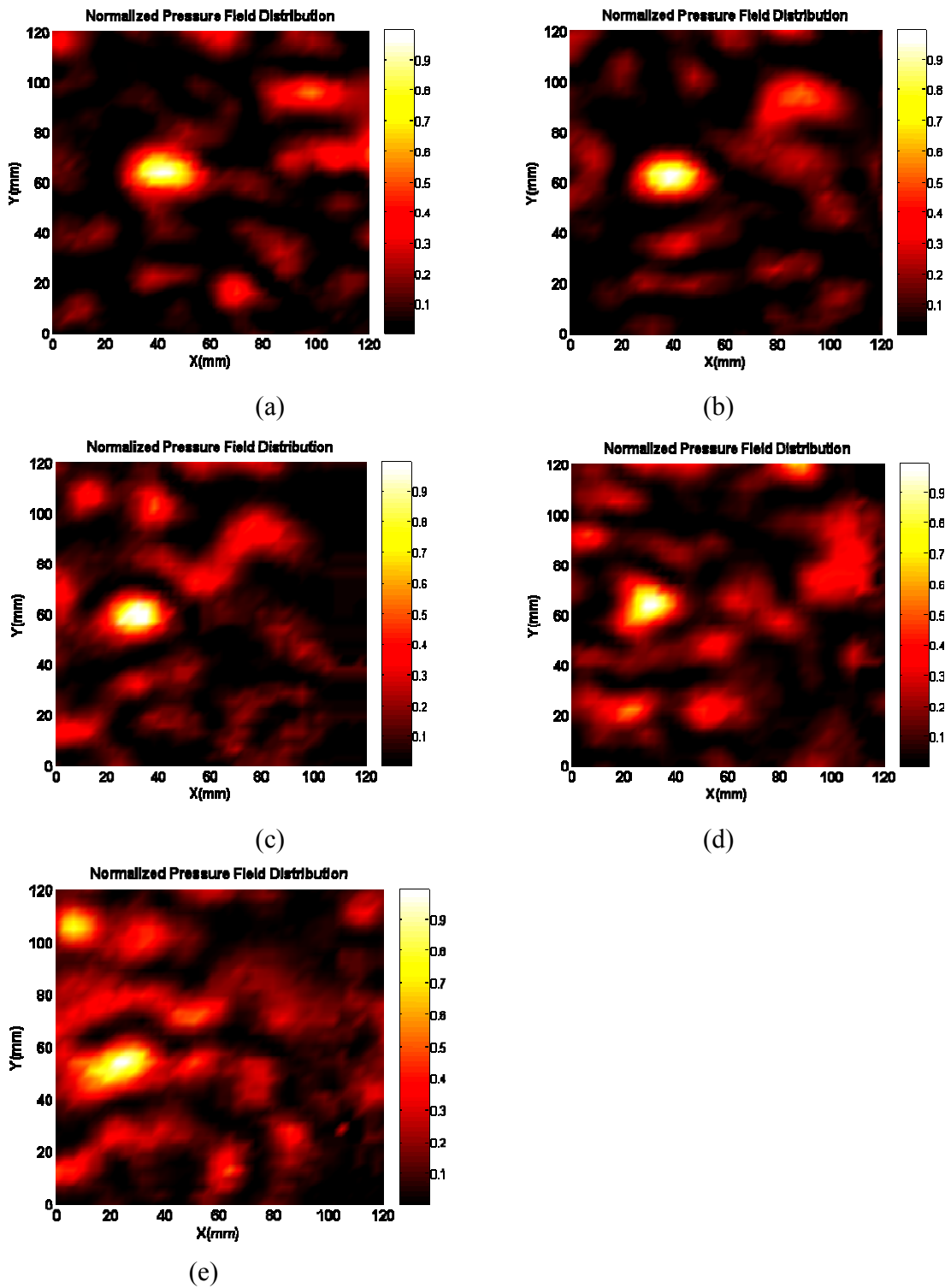
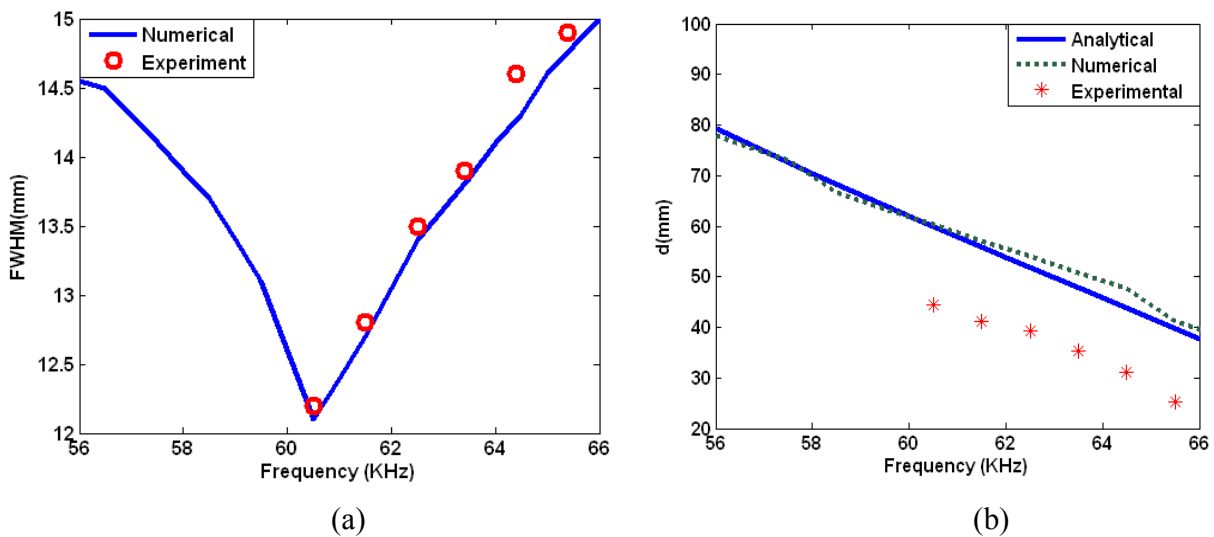


Figure 3-9 Pseudo colormap of measured pressure amplitude distribution at (a) 61.5 KHz (b)

62.5 KHz (c) 63.5 KHz (d) 64.5 KHz (e) 65.5 KHz

pressure fields at different frequencies are presented. The pressure amplitude is normalized to unity. Tight spots are observed in these pressure maps. We also plotted the full width at half maximum (FWHM) at different frequencies in Figure 3-10 (a). The optimal focus imaging is observed at 60.5 kHz from both experimental and numerical results. The FWHM increases with increasing frequency. The focal point moves closer to the PI/NI interface (at  $x=0$ ) at higher frequency.



**Figure 3-10** Measured and calculated FWHM of the focus as a function of frequency. Blue solid line is calculated using acoustic circuit model and red circles represent experimental data. (b) Measured and calculated focal length as a function of frequency. The analytical curve (blue solid line) is based on ray propagation and the green dashed line is numerical results from acoustic circuit model. Experimentally obtained data are shown by red circles.

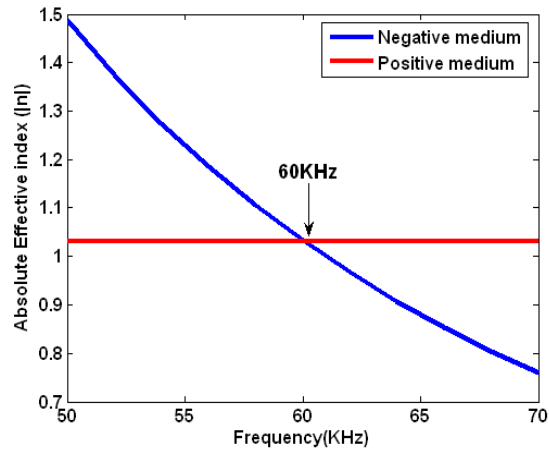


**Figure 3-11** The absolute value of effective refractive index as function of frequency. The relative refractive index is -1 at 60.5 kHz.

The focal length defined as the distance between focus and PI/NI interface is plotted in Figure 3-10 (b) as a function of frequency. Ray acoustics is utilized to estimate the focal length as shown in the blue solid line. The magnitude of the refractive index in the acoustic metamaterial decreases from 1.19 to 0.85 as the frequency increases from 56 to 66 KHz. And this analysis predicts that the negative refractive index approaches -1 relative to the PI part at 60.5 KHz. The decrease of the index magnitude over this frequency range causes the focal length decreasing from 79.27 to 37.6mm. The lumped circuit simulation gives the dashed green curve while the red stars show the measurement data. The three curves present a good match in trend. However, around 10 mm shift is observed.

In order to achieve high-quality focus imaging, the ratio of refractive index should be -1 at the PI/NI interface. Only when the index is matched, based on ray acoustics, the angle of refraction equals the angle of incidence for each ray such that all rays can be brought to the same

focal spot in the NI part. However, due to the loss and variation of the inductance and capacitance from their design values resulted from machining tolerance; the refractive index is not exactly matched in the measurement. Therefore, the distance between the focus and the interface varies for different incident angle as result of aberration <sup>8</sup>. Due to this index mismatch, we observed that the focal spot elongated along x direction while remain narrow along the direction parallel to the interface in the experiment. And the focus is in a position closer to the interface than the source. The best focusing resolution is observed at 60.5 KHz. We expect that the ratio of refractive index might approach -1 at lower frequency. However verification of this is beyond the operation frequency range of our transducer in the experiment. The slight material loss in the measurement also significantly degrades the focusing resolution as discussed in several papers. <sup>51,52</sup> It was noted that single PI/NI interface does not allow the enough growth of evanescent fields to achieve sub diffraction focusing <sup>8</sup> while sandwich structure (two PI/NI interfaces) offers better chance to overcome the diffraction limit.<sup>10</sup>

### **3.4.3 Conclusion**

In summary, the emission of a point source at kilohertz frequency was brought to a focus through the PI/NI interface because of the negative refraction in this ultrasonic metamaterial, which is expected to be a step toward a novel acoustic imaging lens. The resolution of 0.5 wavelength was recorded by focusing the acoustic field of a point source. This is not sub diffraction imaging, but among the best achievable passive acoustic imaging elements. The unit cell of the acoustic

network is only one eighth of the operating wavelength, making the lens in a compact size. Compared with conventional lenses, the flat thin slab lens takes advantages in that there is no need to manufacture the shapes of spherical curvatures and the focus position is insensitive to the offset of source along the axis. Also this negative index lens offers tunable focal length at different frequencies. More generally, this design approach may lead to novel strategies of acoustic cloak for camouflage under sonar.

## References

---

- <sup>1</sup> J. B. Pendry, “Negative refraction makes a perfect lens”, *Phys. Rev. Lett.* **85**, 3966 (2000).
- <sup>2</sup> D. R. Smith et al, “Composite medium with simultaneously negative permeability and permittivity”, *Phys. Rev. Lett.*, **84**, 4184 (2000).
- <sup>3</sup> R. A. Shelby, D. R. Smith and S. Schultz, “Experimental verification of a negative index of refraction”, *Science* 292, 77 (2001).
- <sup>4</sup> S. Foteinopoulou, E. N. Economou, and C. M. Soukoulis, “Refraction in media with a negative refractive index”, *Phys. Rev. Lett.*, **90**, 107402 (2003).
- <sup>5</sup> A. A. Houck, J. B. Brock and I. L. Chuang, “Experimental observations of a left-handed material that obeys snell's law”, *Phys. Rev. Lett.* **90**, 137401 (2003).

---

<sup>6</sup> H. J. Lezec, J. A. Dionne, H. A. Atwater, “Negative refraction at visible frequencies”, *Science* **20**,430 (2007).

<sup>7</sup> N. Fang, H. Lee, C. Sun, and X. Zhang, “Sub-diffraction-limited optical imaging with a silver superlens”, *Science* **308**, 534 (2005).

<sup>8</sup> G. V. Eleftheriades, A. K. Iyer, P. C. Kremer, “Planar negative refractive index media using periodically L-C loaded transmission lines”, *IEEE Trans. Microwave Theory and Tech.* **50**, 2702 (2002).

<sup>9</sup> A. K. Iyer, P. C. Kremer, G. V. Eleftheriades, “Experimental and theoretical verification of focusing in a large, periodically loaded transmission line negative refractive index metamaterial”, *Opt. Express* **11**, 696 (2003).

<sup>10</sup> A. Grbic, G. V. Eleftheriades’, “Overcoming the diffraction limit with a planar left-handed transmission-line lens”, *Phys. Rev. Lett.* **92**, 117403 (2004).

<sup>11</sup> C.Y. Qiu, X. D. Zhang and Z. Y. Liu, “Far-field imaging of acoustic waves by a two-dimensional sonic crystal”, *Phys. Rev. B* **71**, 054302 (2005).

---

<sup>12</sup> X. D. Zhang and Z. Y. Liu, “Negative refraction of acoustic waves in two-dimensional phononic crystals”, *Appl. Phys. Lett.* **85**, 341 (2004).

<sup>13</sup> S. X. Yang *et al.*, “Focusing of sound in 3D phononic crystal”, *Phys. Rev. Lett.* **93**, 024301(2004).

<sup>14</sup> M. Z. Ke *et al.*, “Negative-refraction imaging with two-dimensional phononic crystal”, *Phys. Rev. B* **72**, 064306 (2005).

<sup>15</sup> A. Sukhovich, L. Jing and J. H. Page, “Negative refraction and focusing of ultrasound in two-dimensional phononic crystals”, *Phys. Rev. B* **77**, 014301 (2008).

<sup>16</sup> Z. Liu, X. Zhang, Y. Mao *et al.*, “Locally resonant sonic materials”, *Science* **289**, 1734 (2000).

<sup>17</sup> J. Li and C. T. Chan, “Double-negative acoustic metamaterial”, *Phys. Rev. E* **70**, 055602 (2004).

<sup>18</sup> Z. Y. Liu, C. T. Chan, and P. Sheng, “Analytic model of phononic crystals with local resonances”, *Phys. Rev. B* **71**, 014103 (2005).

---

<sup>19</sup> Y. Q. Ding, Z.Y. Liu, C. Y. Qiu and J. Shi, “Metamaterial with simultaneously negative bulk modulus and mass density”, *Phys. Rev. Lett.* **99**, 093904 (2007).

<sup>20</sup> J. Li, Z. Liu, and C. Qiu, “Negative refraction imaging of acoustic waves by a two-dimensional three-component phononic crystal”, *Phys. Rev. B* **73**, 054302 (2006).

<sup>21</sup> N. Fang, D. J. Xi, J. Y. Xu, M. Ambrati, W. Sprituravanich, C. Sun, and X. Zhang, “Ultrasonic metamaterials with negative modulus”, *Nat. Mater.* **5**, 452 (2006).

<sup>22</sup> Veselago, V. G., “The electrodynamics of substances with simultaneously negative values of  $\mu$  and  $\epsilon$ ,” *Sov. Phys. Usp.*, Vol. 10, No. 4, 509 (1968).

<sup>23</sup> E. N. Economou and M. M. Sigalas, “Classical wave propagation in periodic structures: Cermet versus network topology”, *Phys. Rev. B* **48**, 13434 (1993).

<sup>24</sup> M. S. Kushwaha, P. Halevi, L. Dobrzynski, and B. Djafari-Rouhani, “Acoustic band structure of periodic elastic composites”, *Phys. Rev. Lett.* **71**, 2022 (1993).

<sup>25</sup> M. Kafesaki and E. N. Economou, “Multiple-scattering theory for three-dimensional periodic

---

acoustic composites”, *Phys. Rev. B* **60**, 11993 (1999).

<sup>26</sup> J. O. Vasseur, P. A. Deymier, B. Chenni, B. Djafari-Rouhani, L. Dobrzynski, and D. Prevost, “Experimental and Theoretical Evidence for the Existence of Absolute Acoustic Band Gaps in Two-Dimensional Solid Phononic Crystals”, *Phys. Rev. Lett.* **86**, 3012 (2001).

<sup>27</sup> Torres, M.; Montero de Espinoza, F.R.; Aragon, J.L. “Ultrasonic Wedges for Elastic Wave Bending and Splitting without Requiring a Full Band Gap”, *Phys. Rev. Lett.* **86**, 4282 (2001).

<sup>28</sup> F. Cervera, L. Sanchis, J. V. Sanchez-Perez, R. Martinez-Sala, C. Rubio, and F. Meseguer, “Refractive Acoustic Devices for Airborne Sound”, *Phys. Rev. Lett.* **88**, 023902 (2002).

<sup>29</sup> N. Garcia, M. Nieto-Vesperinas, E. V. Ponizovskaya, and M. Torres, “Theory for tailoring sonic devices: Diffraction dominates over refraction”, *Phys. Rev. E* **67**, 046606 (2003).

<sup>30</sup> Bikash C. Gupta and Zhen Ye, “Theoretical analysis of the focusing of acoustic waves by two-dimensional sonic crystals”, *Phys. Rev. E* **67**, 036603 (2003).

<sup>31</sup> M. Notonmi, “Theory of light propagation in strongly modulated photonic crystals: Refraction like behavior in the vicinity of the photonic band gap”, *Phys. Rev. B* **62** 10696 (2000).

- 
- <sup>32</sup> Luo, S. G. Johnson, J. D. Joannopoulos, and J. B. Pendry, “All-angle negative refraction without negative effective media”, *Phys. Rev. B* **65**, 201104 (2002).
- <sup>33</sup> E. Cubukcu, K. Aydin, E. Ozbay, S. Foteinopoulou, and C. M. Soukoulis, “Negative refraction by photonic crystals”, *Nature*(London) **423**, 604 (2003).
- <sup>34</sup> E. Cubukcu, et al “Subwavelength resolution in a two-dimensional photonic-crystal-based superlens”, *Phys.Rev.Lett.***91**, 207401(2003).
- <sup>35</sup> J. H. Page et al. “Phononic crystals”, *phys. stat. sol. (b)* 241, No. 15, 3454–3462 (2004).
- <sup>36</sup> J. P. Wolfe, *Imaging Phonons: Acoustic Wave Propagation in Solids* (Cambridge University Press, Cambridge, (1998).
- <sup>37</sup> X. D. Zhang and Z. Y. Liu, “Negative refraction of acoustic waves in two-dimensional phononic crystals”, *Appl. Phys. Lett.* **85**, 341 (2004).
- <sup>38</sup> C.Y. Qiu ,X. D. Zhang and Z. Y. Liu. “Far-field imaging of acoustic waves by a two-dimensional sonic crystal”, *Phys. Rev. B* **71**, 054302 (2005).

---

<sup>39</sup> S. Yang, J. H. Page, Z. Liu, M. L. Cowan, C. T. Chan, and P. Sheng, “Focusing of Sound in a 3D Phononic Crystal”, *Phys. Rev. Lett.* **93**, 024301 (2004).

<sup>40</sup> M. Ke, Z. Liu, C. Qiu, W. Wang, J. Shi, W. Wen, and P. Sheng, “ Negative refraction imaging with two-dimensional phononic crystals”, *Phys. Rev. B* **72**, 064306 (2005).

<sup>41</sup> A Sukhovich, L Jing, J.H. Page, “Negative refraction and focusing of ultrasound in two-dimensional phononic crystals”, *Phys. Rev. B*, **77**, 014301 (2008).

<sup>42</sup> V. Fokin, M. Ambati, C. Sun, and Xiang Zhang, “Method for retrieving effective properties of locally resonant acoustic metamaterials”, *Phys. Rev. B* **76**, 144302 (2007).

<sup>43</sup> Z. Liu, X. Zhang, Y. Mao, Y. Y. Zhu, Z. Yang, C. T. Chan, and P. Sheng, “Locally Resonant Sonic Materials”, *Science* **289**, 1734 (2000).

<sup>44</sup> Z. Liu, C. T. Chan, and P. Sheng, “Analytic model of phononic crystals with local resonances”, *Phys. Rev. B* **71**, 014103 (2005).

<sup>45</sup> Y. Wu, Y. Lai, and Z. Q. Zhang, “Effective medium theory for elastic metamaterials in two

---

dimensions”, *Phys. Rev. B* **76**, 205313 (2007).

<sup>46</sup> Y. Ding, Z. Liu, C. Qiu, and J. Shi, “Metamaterial with Simultaneously Negative Bulk Modulus and Mass Density”, *Phys. Rev. Lett.* **99**, 093904 (2007).

<sup>47</sup> L. E. Kinsler, *Fundamentals of Acoustics*, 1982, Wiley, New York

<sup>48</sup> G. W. Stewart, “Acoustic wave filters”, *Phys.Rev.***20**,528 (1922).

<sup>49</sup> W. P. Mason, “A study of the regular combination of acoustic elements, with applications to recurrent acoustic filters, tapered acoustic filters, and horns”, *Bell Syst. Tech. J.* **6**, 258 (1927).

<sup>50</sup> L.L.Beranek, *Acoustics*,1954,McGRAW-HILL,New York

<sup>51</sup> D. R. Smith *et al*, “Limitations on subdiffraction imaging with a negative refractive index slab”, *Appl. Phys. Lett.* **82** ,1506 (2003).

<sup>52</sup> N. Fang and X. Zhang, “Imaging properties of a metamaterial superlens”, *Appl. Phys. Lett.* **82**, 161 (2003).

## 4 BROADBAND ACOUSTIC CLOAK FOR ULTRASOUND WAVES

### 4.1 Introduction

Recently, a new design paradigm called conformal mapping and coordinate transformation has inspired a series of key explorations to manipulate, store and control the flow of energy, in form of either sound, elastic waves or light radiation. In electromagnetism, because of the coordinate invariance of Maxwell's equations, the space for light can be bent in almost arbitrary ways by providing a desired spatial distribution of electric permittivity  $\epsilon$  and magnetic permeability  $\mu$ .<sup>1,2</sup> A set of novel optical devices were proposed based on transformation optics<sup>3,4,5</sup>; they usually call for complicated medium with anisotropic and spatially varying permittivity and permeability tensor to accomplish the desired functionality. Recent advances in synthetic structured metamaterial<sup>6,7</sup> whose properties are determined by its subwavelength structure, offers the potential to physically implement these complicated media. By modifying the shape and arrangement of these subwavelength constituent elements, anisotropy and spatial variation can be achieved in the artificial metamaterials.

Among the most exciting examples is perhaps an electromagnetic cloak that can render the objects invisible. The first experimental demonstration of such a cloak was reported in microwave using structured metamaterial composed of metallic resonant rings<sup>8</sup>. However, the invisibility effect was only obtained in a narrow frequency range because of the strong dispersion inherent to the resonant elements used to build the cloak. In addition, such resonances led to undesired material absorption in the cloak. To mitigate these constrains, several different

schemes of cloaking utilizing non-resonant structure were proposed<sup>9,10,11,12,13</sup>. One example is a so-called carpet cloak which compresses the cloaked space into a thin sheet<sup>14,15</sup>. However, the waves travel faster through the carpet cloak than through the outer space, such a faster-than-light speed thereby sets a fundamental restriction for broadband application in ambient air. Therefore, the experiments of these carpet cloaks were so far conducted in a dielectric medium with higher index.

In contrast, cloaking of other classical waves such as acoustic waves do not suffer from such limitation for electromagnetic cloaks.<sup>16,17,18</sup> However, in general the elastodynamic equations do not have this invariance symmetry as proven by Milton et al<sup>19</sup>. Fortunately, acoustic waves in fluids follow such form invariance and several theoretical schemes of transformation have been proposed.<sup>20,21,22</sup> Theoretical analysis of an acoustic cloak<sup>23</sup> was reported based on the equivalence between transverse electric electromagnetic waves and acoustic waves in a two-dimensional (2D) geometry. Yet, this 2D acoustic cloak requires anisotropic mass density which is not common in naturally-occurring materials. Consequently the experimental studies of acoustic cloak have been hampered by the difficulty in creating suitable materials and so far remain challenging.

In this thesis, we overcome the above challenges in acoustic cloak design by introducing an acoustic transmission line approach. By taking the analogy between lumped acoustic elements and electronic circuit elements, this transmission line approach enabled a new class of acoustic metamaterials<sup>24</sup> and ultrasound focusing through a metamaterial network.<sup>25</sup> As a demonstration, we designed a 2D cylindrical cloak in order to hide an object in the center. This acoustic

cylindrical cloak is implemented by a 2D array of sub-wavelength cavities and connecting channels with spatially tailored geometry. The acoustic wave propagation through this discrete network can be described by a set of telegrapher's equations. This approach enables the realization of acoustic metamaterials with simple structure, ease of manufacturing and scaling, offering the potential to achieve a variety of acoustic devices based on transformation. Moreover, the acoustic cloak is expected to be low-loss and broadband with the use of non-resonant constituent elements.

## 4.2 Optical Transformation

### 4.2.1 Rules of Covariant and Contravariant Transformation

In mathematics and theoretical physics, covariance and contravariance refer to how coordinates change under a transformation. A covariant transformation is a rule that describes how certain physical entities change under a change of coordinate system and the inverse transformation is called as contravariant transformation. The general formulation of covariance and contravariance guarantees that any vector should be invariant under a coordinate transformation.

If  $\mathbf{e}^1, \mathbf{e}^2, \mathbf{e}^3$  are contravariant basis vectors of  $\mathbf{R}^3$  (not necessarily orthogonal nor of unit norm)

then the covariant basis vectors of their reciprocal system are:

$$\mathbf{e}_1 = \frac{\mathbf{e}^2 \times \mathbf{e}^3}{\mathbf{e}^1 \cdot (\mathbf{e}^2 \times \mathbf{e}^3)}; \quad \mathbf{e}_2 = \frac{\mathbf{e}^3 \times \mathbf{e}^1}{\mathbf{e}^2 \cdot (\mathbf{e}^3 \times \mathbf{e}^1)}; \quad \mathbf{e}_3 = \frac{\mathbf{e}^1 \times \mathbf{e}^2}{\mathbf{e}^3 \cdot (\mathbf{e}^1 \times \mathbf{e}^2)}. \quad (4-1)$$

Note that  $\mathbf{e}_i$  and  $\mathbf{e}^i$  are mutually orthonormal

$$\mathbf{e}^i \cdot \mathbf{e}_j = \delta_j^i \quad (4-2)$$

the contravariant coordinates of any vector  $\mathbf{v}$  can be obtained by

$$q_1 = \mathbf{v} \cdot \mathbf{e}_1; \quad q_2 = \mathbf{v} \cdot \mathbf{e}_2; \quad q_3 = \mathbf{v} \cdot \mathbf{e}_3 \quad (4-3)$$

Likewise, the covariant components of  $\mathbf{v}$  can be obtained

$$q^1 = \mathbf{v} \cdot \mathbf{e}^1; \quad q^2 = \mathbf{v} \cdot \mathbf{e}^2; \quad q^3 = \mathbf{v} \cdot \mathbf{e}^3 \quad (4-4)$$

So  $\mathbf{v}$  can be expressed as,

$$\mathbf{v} = q_i \mathbf{e}^i = q_1 \mathbf{e}^1 + q_2 \mathbf{e}^2 + q_3 \mathbf{e}^3 \quad \text{or} \quad \mathbf{v} = q^i \mathbf{e}_i = q^1 \mathbf{e}_1 + q^2 \mathbf{e}_2 + q^3 \mathbf{e}_3 \quad (4-5)$$

$$\text{Then,} \quad \mathbf{v} = (\mathbf{v} \cdot \mathbf{e}_i) \mathbf{e}^i = (\mathbf{v} \cdot \mathbf{e}^i) \mathbf{e}_i \quad (4-6)$$

Thus the vector can be easily converted between covariant to contravariant basis

$$q_i = \mathbf{v} \cdot \mathbf{e}_i = (q^j \mathbf{e}_j) \cdot \mathbf{e}_i = (\mathbf{e}_j \cdot \mathbf{e}_i) q^j \quad \text{and} \quad q^i = \mathbf{v} \cdot \mathbf{e}^i = (q_j \mathbf{e}^j) \cdot \mathbf{e}^i = (\mathbf{e}^j \cdot \mathbf{e}^i) q_j \quad (4-7)$$

If the contravariant basis vectors are orthonormal then they are equivalent to the covariant basis vectors

#### 4.2.2 Invariance in Electromagnetism

Assume the coordinate transformation as from a Cartesian coordinates  $x, y, z$  to a general system  $\phi_1, \phi_2, \phi_3$

$$\phi_1(x, y, z), \phi_2(x, y, z), \phi_3(x, y, z) \quad (4-8)$$

The length of a line element is given by

$$\begin{aligned} ds^2 &= dx^2 + dy^2 + dz^2 \\ &= T_{11} d\phi_1^2 + T_{22} d\phi_2^2 + T_{33} d\phi_3^2 + 2T_{12} d\phi_1 d\phi_2 + 2T_{13} d\phi_1 d\phi_3 + 2T_{23} d\phi_2 d\phi_3 \end{aligned} \quad (4-9)$$

Where  $T_{ij} = \frac{\partial x}{\partial \phi_i} \frac{\partial x}{\partial \phi_j} + \frac{\partial y}{\partial \phi_i} \frac{\partial y}{\partial \phi_j} + \frac{\partial z}{\partial \phi_i} \frac{\partial z}{\partial \phi_j}$

Define three units vectors  $\mathbf{u}_1, \mathbf{u}_2, \mathbf{u}_3$ , to point along the generalized  $\phi_1, \phi_2, \phi_3$  axes .The length of a vector along the axis direction can be interpreted as  $ds_i = T_i d\phi_i$ , where  $T_i^2 = T_{ii}$

Write the three component of the  $\mathbf{E}$  field in new general coordinate system

$$\mathbf{E}_1 = \mathbf{E} \cdot \mathbf{u}_1, \quad \mathbf{E}_2 = \mathbf{E} \cdot \mathbf{u}_2, \quad \mathbf{E}_3 = \mathbf{E} \cdot \mathbf{u}_3 \quad (4-10)$$

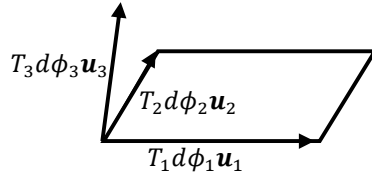


**Figure 4-1** Small element in the general coordinate system  $\phi_1, \phi_2, \phi_3$ .

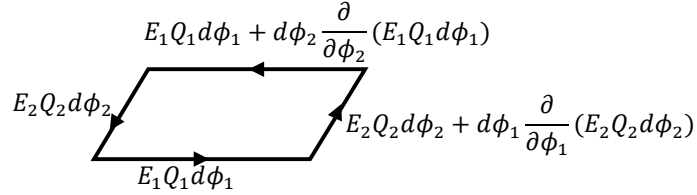


**Figure 4-2** Integration path for  $\mathbf{E}$ .

By stokes' theorem, the line integration of E field can be written as,

$$d\phi_1 \frac{\partial}{\partial \phi_1} (E_2 Q_2 d\phi_2) - d\phi_2 \frac{\partial}{\partial \phi_2} (E_1 Q_1 d\phi_1) = (\nabla \times \mathbf{E}) \cdot (\mathbf{u}_1 \times \mathbf{u}_2) T_1 d\phi_1 T_2 d\phi_2 \quad (4-11)$$

This equation can be further simplified

$$(\nabla \times \mathbf{E}) \cdot (\mathbf{u}_1 \times \mathbf{u}_2) T_1 T_2 = \frac{\partial \hat{E}_2}{\partial \phi_1} - \frac{\partial \hat{E}_1}{\partial \phi_2} = (\nabla_{\phi} \times \hat{\mathbf{E}})^3 \quad (4-12)$$

Where  $\hat{E}_1 = T_1 E_1, \hat{E}_2 = T_2 E_2, \hat{E}_3 = T_3 E_3$

The relation of the contravariant components and covariant components of  $\mathbf{H}$  is

$$\begin{bmatrix} H_1 \\ H_2 \\ H_3 \end{bmatrix} = \begin{bmatrix} \mathbf{u}_1 \cdot \mathbf{u}_1 & \mathbf{u}_1 \cdot \mathbf{u}_2 & \mathbf{u}_1 \cdot \mathbf{u}_3 \\ \mathbf{u}_2 \cdot \mathbf{u}_1 & \mathbf{u}_2 \cdot \mathbf{u}_2 & \mathbf{u}_2 \cdot \mathbf{u}_3 \\ \mathbf{u}_3 \cdot \mathbf{u}_1 & \mathbf{u}_3 \cdot \mathbf{u}_2 & \mathbf{u}_3 \cdot \mathbf{u}_3 \end{bmatrix} \begin{bmatrix} H^1 \\ H^2 \\ H^3 \end{bmatrix} = \Lambda^{-1} \begin{bmatrix} H^1 \\ H^2 \\ H^3 \end{bmatrix} \quad (4-13)$$

$$\text{Or } H^i = \sum_j^3 \Lambda^{ij} H_j \quad (4-14)$$

From definition

$$H_1 = H \cdot \mathbf{u}_1, \quad H_2 = H \cdot \mathbf{u}_2, \quad H_3 = H \cdot \mathbf{u}_3 \quad (4-15)$$

$$H = H^1 \mathbf{u}_1 + H^2 \mathbf{u}_2 + H^3 \mathbf{u}_3 \quad (4-16)$$

Use Faraday's law, the right side of (4-12) can be modified

$$\begin{aligned} & (\nabla \times \mathbf{E}) \cdot (\mathbf{u}_1 \times \mathbf{u}_2) T_1 T_2 \\ &= -\mu_0 \mu \frac{\partial H}{\partial t} \cdot (\mathbf{u}_1 \times \mathbf{u}_2) T_1 T_2 = -\mu_0 \mu \sum_j^3 \Lambda^{3j} \frac{\partial H_j}{\partial t} \mathbf{u}_3 \cdot (\mathbf{u}_1 \times \mathbf{u}_2) T_1 T_2 \end{aligned} \quad (4-17)$$

Define  $\hat{\mu}^{ij} = \mu \Lambda^{ij} |u_1 \cdot (u_2 \times u_3)| T_1 T_2 T_3 (T_i T_j)^{-1}$   $\hat{H}_j = T_j E_j$

$$(\nabla \times \mathbf{E}) \cdot (\mathbf{u}_1 \times \mathbf{u}_2) T_1 T_2 = -\mu_0 \sum_{j=1}^3 \hat{\mu}^{3j} \frac{\partial \hat{H}_j}{\partial t} \quad (4-18)$$

Substitute (4-12)

$$(\nabla_\phi \times \hat{E})^i = -\mu_0 \sum_{j=1}^3 \hat{\mu}^{ij} \frac{\partial \hat{H}_j}{\partial t} \quad (4-19)$$

Similarly

$$(\nabla_\phi \times \hat{H})^i = \epsilon_0 \sum_{j=1}^3 \hat{\epsilon}^{ij} \frac{\partial \hat{E}_j}{\partial t} \quad (4-20)$$

Where  $\hat{\epsilon}^{ij} = \epsilon \Lambda^{ij} |u_1 \cdot (u_2 \times u_3)| T_1 T_2 T_3 (T_i T_j)^{-1}$

Note that when the general coordinate system  $\phi_1, \phi_2, \phi_3$  is orthogonal

$$\Lambda^{ij} |u_1 \cdot (u_2 \times u_3)| = \delta_{ij} \quad (4-21)$$

So the Maxwell's equations are of the same form in any coordinate system but the values of permittivity and permeability will change. This implies that, mathematically, the description of the permittivity and permeability has the same effect on the electromagnetic fields as a coordinate transformation.

### 4.2.3 Transformation Media and Invisible Cloak

It is known that if light travels in a gradient index medium, where the refractive index changes as a function of position, the light ray will follow a curved path determined by the nature of the gradient. Therefore by controlling the permittivity and permeability distribution in space, the propagation path of electromagnetic wave can be controlled. The question is how to obtain the precise description of the medium property as function of position to achieve the desired redirection of optical rays.

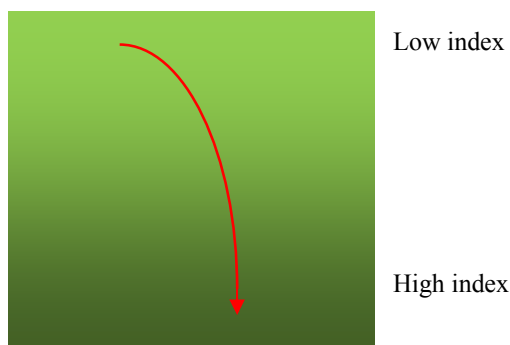


**Figure 4-3** Wave propagation in a gradient medium.

The coordinate invariance of Maxwell's equations we discussed in previous section enables one possible design strategy to provide the prescription of the gradient medium to control and manipulate wave propagation path. It was demonstrated that the arbitrary distortion of wave fields can be recorded as a coordinate transformation. On the other hand, the desired

transformation can be equivalently achieved by providing the transformation materials in the engineered space. Transformation media is defined as such that implement the same coordinate transformations effect in Maxwell's equations. The design approach is quite straightforward. Assume there are two different coordinate systems and two different spaces. In the first space, which is named as virtual space, the Maxwell equations are usually written in Cartesian coordinates in free space with a simple configuration of permittivity and permeability. Then we imagine the Cartesian coordinate lines were distorted and the deformed coordinates could be described by a coordinate transformation. The Cartesian grid in the virtual space will deform under the transformation and this deformed grid shows ray trajectories in the physical space. Next rewrite Maxwell's equations using the new coordinate system in the new space, called as physical space. In previous section, we presented that the Maxwell's equation are of the same form in any coordinate system but the values of permittivity and permeability will change under the transformation. By providing the straightforward prescription for a material, the fields in the physical space which take up the distorted configuration can be obtained. If we can make the material, we can accomplish the same result in terms of controlling the trajectories of the rays of light. This has spawned a new field called transformation optics, in pursuit of harness exotic optical device. For example, the waves can be focused as desired or steered to avoid scattering objects and flow around them like a fluid, recombined to their original trajectories.

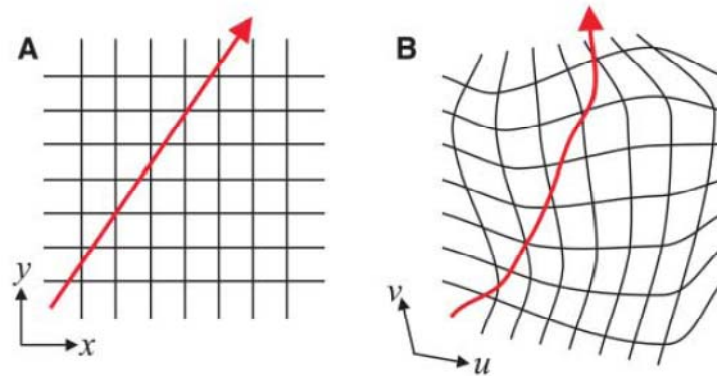


**Figure 4-4** (A) A field line in free space with the background Cartesian coordinate grid shown. (B) The distorted field line with the background coordinates distorted in the same fashion. <sup>1</sup>

Usually, the transformation will lead to complex material properties such as anisotropy and inhomogeneous that doesn't exist in nature. However, thanks for the development of metamaterial, an extraordinary range of electromagnetic properties can be engineered in artificially structured metamaterials, with a flexibility unmatched by any conventional material. An extraordinary range of electromagnetic properties can be engineered in artificially structured metamaterials, with flexibility unmatched by any conventional material. Taking full advantage of this enormous flexibility has led to a variety of application based on transformation optics, such as perfect lens,<sup>26</sup> and magnification.<sup>27</sup> Among all these applications, the invisible cloak might be one of the most interesting one.

Invisibility cloaks work by steering light around a region of space and recombine on the other side to the original trajectory, making any object inside that region and the cloak invisible. In effect, an invisibility cloak creates the illusion the light had passed through the empty volume of space. In order to do so, in two dimensional cases, the idea is to make a coordinate

transformation that takes a point in space and expands it into a cylinder the interior of which is invisible to an observer on the outside. So no radiation can get into the concealed volume, nor can any radiation get out. In two-dimensional (2D) a simple transformation that can realize this goal is to compress all fields in the region  $0 < r < R_2$  into the annular region  $R_1 < r < R_2$  in a cylindrical coordinate

$$r' = R_1 + r(R_2 - R_1)/R_2 \quad (4-22)$$

$$\theta' = \theta \quad (4-23)$$

$$z' = z \quad (4-24)$$

By coordinate transformation, we can obtain the prescription for the cloak in  $R_1 < r < R_2$  as

$$\frac{\mu_\phi}{\mu_0} = \frac{r}{r-R_1} \quad (4-25)$$

$$\frac{\mu_r}{\mu_0} = \frac{r-R_1}{r} \quad (4-26)$$

$$\frac{\varepsilon_z}{\varepsilon_0} = \left(\frac{R_2}{R_2-R_1}\right)^2 \frac{r-R_1}{r} \quad (4-27)$$

By using material with above prescription, the TM field will exclude all fields from the central region in the engineered space and such make the object together with the cloak invisible.

### 4.3 Acoustic cloak

It is undoubtedly of great interest to extend the design approach based on transformation-based solutions to waves in other systems, for example acoustic waves. The electromagnetic and other wave system shares the universal concepts of wave vector, wave impedance, and power flow.

And the manner in which permittivity and permeability control these in electromagnetics is closely analogous to that by material properties in other wave system. However, the special symmetry in Maxwell equations is an important element of the equivalence between coordinate transformations and material properties. The field equations for other waves may not usually process this property. It was demonstrated that in general the equation of motion in elastic media does not have form invariance. However, in 2D case, the acoustic waves in fluid and Maxwell equations with one single mode have identical form under certain variable exchange.

In 2D cylindrical coordinate with z invariance, the time harmonic acoustic equation for fluid with anisotropic but diagonal in the cylindrical coordinate are interpreted as

$$\frac{\partial P}{r \partial \phi} = -j\omega \rho_\phi u_\phi \quad (4-28)$$

$$\frac{\partial P}{\partial r} = -j\omega \rho_r u_r \quad (4-29)$$

$$\frac{1}{r} \frac{\partial}{\partial r} (r u_r) + \frac{1}{r} \frac{\partial u_\phi}{\partial \phi} = -j\omega \beta P \quad (4-30)$$

Where  $p$  is scalar pressure,  $u_r, u_\phi$  are particle velocity,  $\rho_r, \rho_\phi$  are density along  $r$  and  $\phi$  direction respectively,  $\beta$  is the compressibility. There is an only longitude wave in this anisotropic medium.

In the same z invariant cylindrical coordinate, mode Maxwell's equations for transverse magnetic (TM) mode are

$$\frac{\partial E_z}{r \partial \phi} = i\omega \mu_r H_r \quad (4-31)$$

$$\frac{\partial E_z}{\partial r} = -i\omega \mu_\phi H_\phi \quad (4-32)$$

$$\frac{1}{r} \frac{\partial}{\partial r} (r H_\phi) - \frac{1}{r} \frac{\partial H_r}{\partial \phi} = -i\omega \epsilon_z E \quad (4-33)$$

The medium has anisotropic permittivity and permeability, but the tensor only has diagonal component. Observing the above two sets of equations are equivalent under the following variable exchange

$$E_z \rightarrow -p \quad H_\phi \rightarrow v_r \quad H_r \rightarrow -v_\phi \quad \mu_r \rightarrow \rho_\phi \quad \mu_\phi \rightarrow \rho_r \quad \varepsilon_z \rightarrow \beta \quad (4-34)$$

In terms of boundary condition, in electromagnism, the normal component  $E_z$  and tangential component  $H_\phi$  and continuous, while at a fluid interface, the normal component of particle velocity  $v_r$  and pressure  $p$  are continuous. Thus the boundary conditions are preserved as well under the variable exchange. This implies that the 2D acoustic equations have the same form invariance under coordinate transformation as Maxwell's equations; consequently, we can apply the design approach of transformation optics approach in 2D acoustic scheme.

The invisible cloak can thus be realized acoustically if we can implement a gradient medium with anisotropic density

$$\frac{\rho_r}{\rho_b} = \frac{r}{r-R_1} \quad (4-35)$$

$$\frac{\rho_\phi}{\rho_b} = \frac{r-R_1}{r} \quad (4-36)$$

$$\frac{\beta}{\beta_b} = \left( \frac{R_2}{R_2-R_1} \right)^2 \frac{r-R_1}{r} \quad (4-37)$$

Where  $\rho_b$  ,  $\beta_b$  are the density and compressibility of the background medium.  $R_2$  and  $R_1$  are the radius of the inner and outer boundary of the 2D cloak.

#### 4.4 Numerical Simulation of Acoustic Cloak Based on Transmission Line Model

In order to build the acoustic cloak as described by (4-35)-(4-37), acoustic transmission line approach is employed by cascading the unit cell in Figure 4-5 (d) in a lattice configuration which is diagonal in a cylindrical basis. The distributed acoustic system corresponding to the circuit unit cell can be implemented by one large cavity in the center with four channels connecting to the four neighboring blocks, which will be discussed in more details in the following section.

In such a two-dimensional network, the cloak is approximated by sixteen homogeneous concentric cylinders. The effective anisotropic density and compressibility in these rings was set as a 16-step piecewise constant value as an approximation of the continuous medium. From the first to the fourth layers, the unit cell size along radial direction is  $\lambda/7$ ,  $\lambda/8$ ,  $\lambda/9$  and  $\lambda/9$  ( $\lambda$  is the wavelength in water at 60 kHz) respectively. Afterwards, the cylinder layers are evenly spaced with the distance equal to  $\lambda/10$  along the radial direction. On the other hand, the first cylinder near the inner lining of the cloak is divided to 32 units around the circumference. To keep the size of the constituent element smaller than  $\lambda/10$  along circumferential direction, starting from the second layer, the number of cells is doubled to 64, and further increased to 128 from the sixth layer. Software SPICE is used to simulate the pressure field through the lumped acoustic circuit. The calculation domain is presented in Figure 4-5(a). A point source is incident on an object ( $0.67\lambda$  in diameter) surrounded by a cloaking shell of thickness  $1.6\lambda$ . The cloaked object is put in center of water with circular boundary.

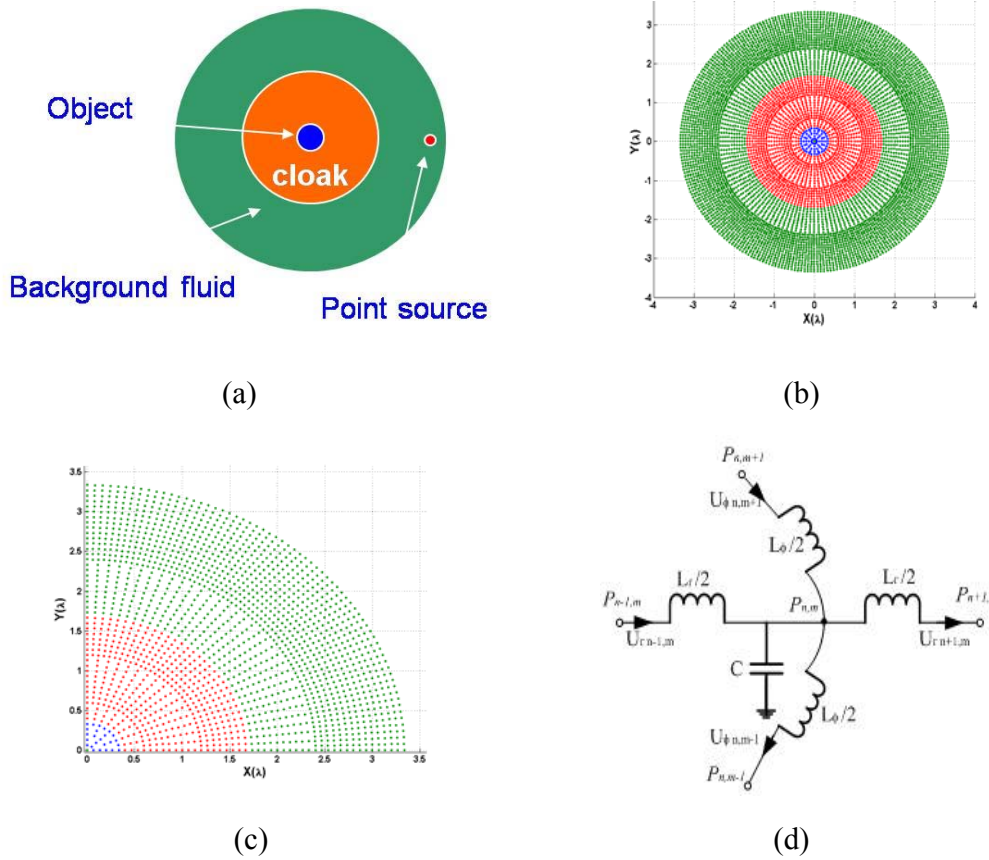


**Figure 4-5** (a) Computational domain (b) mesh model (c) one quarter of the mesh model (d) circuit unit at each mesh node.

Figure 4-6 (a) and (b) show the scaled pressure field amplitude for the cases with and without cloak respectively. The  $x$  and  $y$  coordinate is normalized by the wavelength in water. Comparison shows the wave is guided around the object in the shell and merged behind the object with obvious reduction in back scattering. Nearly zero amplitude field is observed inside the cloak as expected. Continuous medium simulations of 2D cylindrical cloak were performed by COMSOL Multiphysics finite element based solver. Figure 4-6 (c) and (d) are simulation results for when there is cloak and when there is only object respectively.

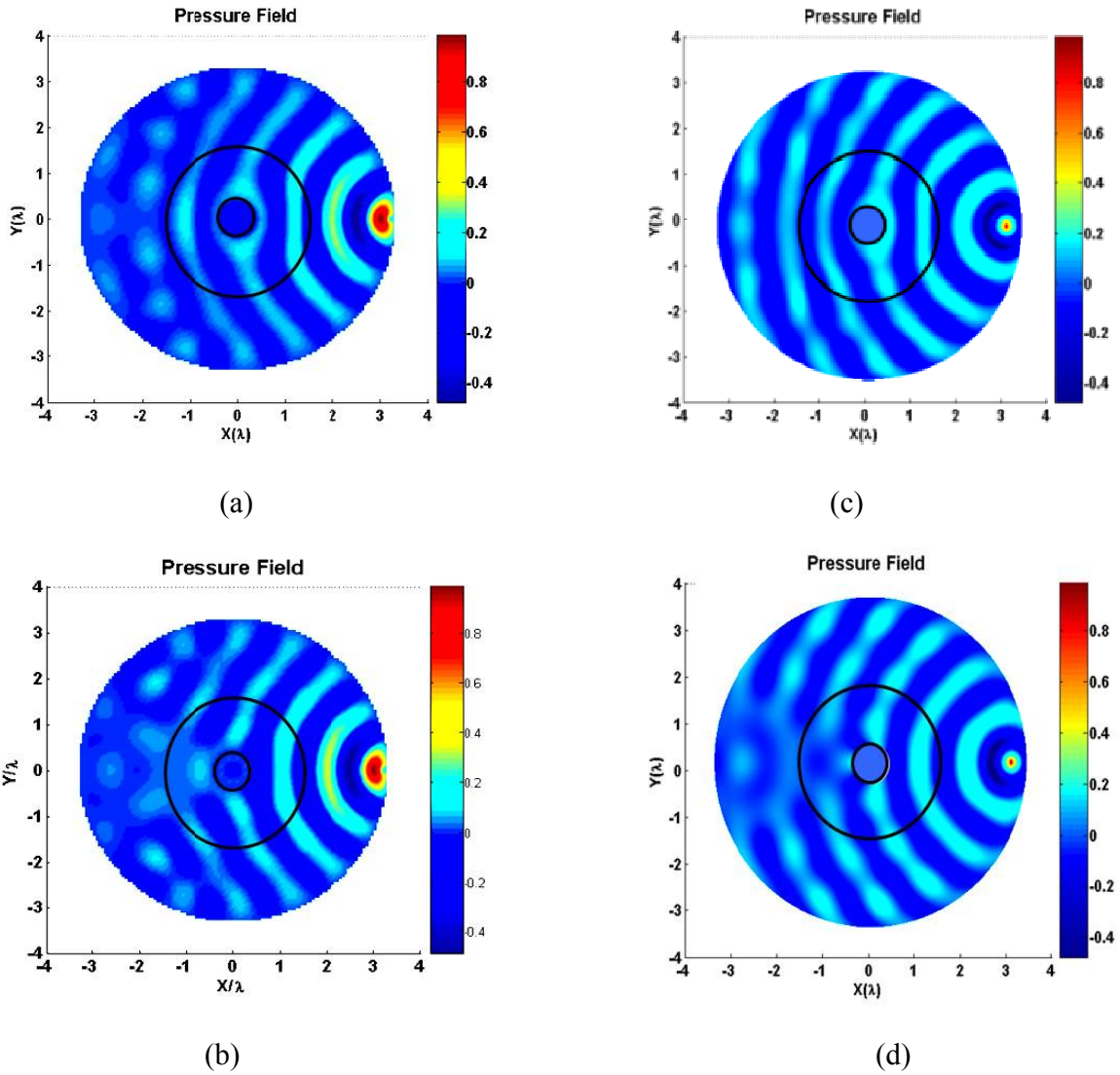


**Figure 4-6** Pseudo colormap of scaled pressure field distribution due to a point source with cloak by (a) lumped circuit and (b) FEM simulation. Pressure field distribution without cloak by (c) lumped circuit and (d) FEM simulation. The black circle marks the outer boundary of the cylindrical cloak.

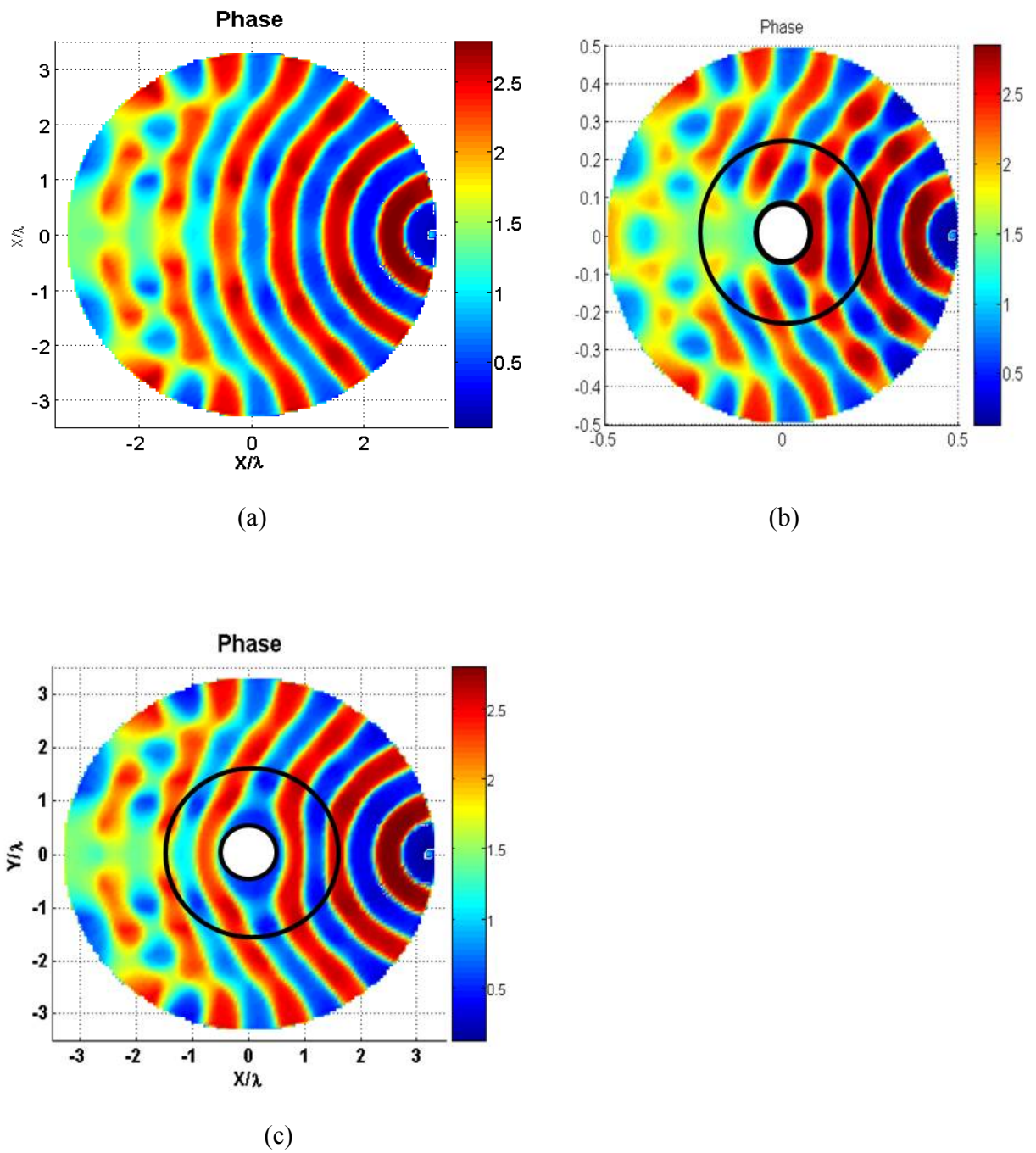


**Figure 4-7** Pseudo colormap of phase field distribution due to a point source (a) in a free field and (b) with a scattering object (c) with a cloaked object. The black circle marks the outer boundary of the cylindrical cloak.

Comparison with FEM model demonstrates that the discretized cloak based on lumped circuit model can force the incident wave energy to bend around the central object. This allows for a practical realization of the acoustic cloak. In continuous model, there is less distortion is observed compared with lumped circuit simulation. One reason is reflection from the boundary in circuit model. In FEM, a perfect match layer is used to achieve zero reflection from the boundary. On the other hand, the mesh is much finer in FEM model. Another reason is additional absorption loss which degrades cloaking performance is added in the circuit model as a small resistor connected to each inductor.

Figure 4-7(a) presents the phase distribution of the free field when there is no object or cloak. When an object is put in the center of the field, obvious scattering is observed. However, there is object is put inside the cloak, it is observed that the field behind the cloaked object is exactly same with the one when there is only free field.

We numerically demonstrated a 2D acoustic shell cloaking by lumped acoustic transmission line design. The artificial anisotropic acoustic medium is built by an array of designed Helmholtz resonators. The simulation results proved that the acoustic wave can be stretched and guided through the cloak without penetrating into the object.

## 4.5 Irregular Transmission Line Network

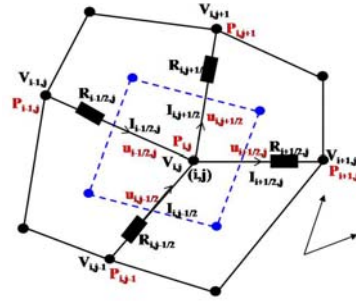


**Figure 4-8** One unit cell for a nonorthogonal transmission line

In order to conform the transmission line network to more general geometry and boundaries, the regular Cartesian lattice is further extended to irregular nonorthogonal structured grids. Further, it is often desirable to have a refined lattice in localized regions. With uniform lattice, this results in global refinement of the mesh density, leading to unnecessary increase in the computational effort and memory resources. This can be solved by nonuniform grids.

Consider a locally curvilinear coordinate system, the linear acoustic wave equations still holds

$$\rho \frac{du}{dt} = -\nabla p$$

$$\nabla \cdot (\rho_0 \vec{u}) = -\frac{1}{c_0^2} \frac{\partial p}{\partial t} \quad (4-38)$$

Use cell of arbitrary parallelepipeds shown in black lines to generate a lumped circuit network. The pressure is collocated at the grid cell vertices black nodes while the particle velocity is defined along edges of cells.

For the first equation which is linear Euler's equation, use the finite difference expression for

the space derivatives and assume harmonic acoustic wave  $e^{i\omega t}$

$$p_{i,j} - p_{i+1,j} = -i\omega\rho_{i,j}u_{i+1/2,j}g_{i+1/2,j} \quad (4-39)$$

$$p_{i,j-1} - p_{i,j} = -i\omega\rho_{i,j}u_{i,j-1/2}g_{i,j-1/2} \quad (4-40)$$

$$p_{i,j} - p_{i,j+1} = -i\omega\rho_{i,j}u_{i,j+1/2}g_{i,j+1/2} \quad (4-41)$$

$$p_{i-1,j} - p_{i,j} = -i\omega\rho_{i,j}u_{i-1/2,j}g_{i-1/2,j} \quad (4-42)$$

Where  $g_{m,n}$  is the edge length shown as black lines.

The second continuity equation can be written in integral form use Gauss's theorem

$$(4-43)$$

This equation presents that the net flow with which mass flows into the volume through its surface must equals the rate with which the mass within the volume increases. And the adiabatic tells  $p = \rho c^2$ .

Define a dual cell associated with each vertices where the pressure defines; which is indicated in dotted blue lines. Consider a small parallelepiped volume

$$dV_{i,j} = S_{i,j}\Delta z \quad (4-44)$$

Where  $S_{i,j}$  is the area of the dual cell inside the dotted blue lines.  $\Delta z$  is the thickness of the volume with z direction perpendicular to the plane. The continuity equation can be written in following discrete form

$$\begin{aligned}
& u_{i+1/2,j} \cdot \rho_{i,j} \cdot l_{i+1/2,j} \cdot \cos \phi_{i+1/2,j} \cdot \Delta z - u_{i,j-1/2} \cdot \rho_{i,j} \cdot l_{i,j-1/2} \cdot \cos \phi_{i,j-1/2} \cdot \Delta z \\
& u_{i,j+1/2} \cdot \rho_{i,j} \cdot l_{i,j+1/2} \cdot \cos \phi_{i,j+1/2} \cdot \Delta z - u_{i-1/2,j} \cdot \rho_{i,j} \cdot l_{i-1/2,j} \cdot \cos \phi_{i-1/2,j} \cdot \Delta z \\
& = -i \frac{\omega}{c^2} p_{i,j} \cdot S_{i,j} \cdot \Delta z = -i \omega \rho_{i,j} \beta_{i,j} p_{i,j} \cdot S_{i,j} \cdot \Delta z
\end{aligned} \tag{4-45}$$

We want to use a lumped circuit network to simulate the above acoustic equations. The circuit consists of serial of impedance and shunt admittance. The telegraph's equations for this circuit network are

$$-I_{i+1/2,j} + I_{i,j+1/2} + I_{i-1/2,j} - I_{i,j-1/2} = V_{i,j} \cdot Y_{i,j} \tag{4-46}$$

$$V_{i,j} - V_{i+1,j} = I_{i+1/2,j} \cdot R_{i+1/2,j} \tag{4-47}$$

$$V_{i,j} - V_{i,j+1} = I_{i,j+1/2} \cdot R_{i,j+1/2} \tag{4-48}$$

$$V_{i-1,j} - V_{i,j} = I_{i-1/2,j} \cdot R_{i-1/2,j} \tag{4-49}$$

$$V_{i,j-1} - V_{i,j} = I_{i,j-1/2} \cdot R_{i,j-1/2} \tag{4-50}$$

The two sets of equations are exact duality of each other under the variable exchange

$$i \omega \beta_{i,j} S_{i,j} \Leftrightarrow Y_{i,j} \tag{4-51}$$

$$\frac{i \omega \rho_{m,n} g_{m,n}}{l_{m,n} \cos \varphi_{m,n}} \Leftrightarrow R_{m,n} \tag{4-52}$$

$$p_{i,j} \Leftrightarrow -V_{i,j} \tag{4-53}$$

$$\mathbf{u}_{m,n} \cdot \mathbf{l}_{m,n} \cdot \cos \varphi_{m,n} \Leftrightarrow -I_{m,n} \tag{4-54}$$

This circuit model can be extended to simulate electromagnetic wave with single polarization, for example TM mode. Collocate the  $\vec{E}$  component at grid cell vertices while

define the  $\vec{H}$  component tangent to the edge of the cells. Apply the same discretization approach to integral form of Faraday's equation and Ampere's law

$$\oint \vec{H} \cdot d\vec{l} = \frac{\partial}{\partial t} \int \vec{D} \cdot d\vec{S} \quad (4-55)$$

$$\oint \vec{E} \cdot d\vec{l} = -\frac{\partial}{\partial t} \int \vec{B} \cdot d\vec{S} \quad (4-56)$$

$$H_{i+1/2,j} \cdot l_{i+1/2,j} + H_{i,j-1/2} \cdot l_{i,j-1/2} - H_{i-1/2,j} \cdot l_{i-1/2,j} - H_{i,j+1/2} \cdot l_{i,j+1/2} = i\omega \epsilon E_{i,j} \cdot S_{i,j} \quad (4-57)$$

$$E_{i,j} \Delta z - E_{i,j+1} \Delta z = i\omega \mu H_{i,j+1/2} \cdot g_{i,j+1/2} \cdot \Delta z \cdot \cos \phi_{i,j+1/2} \quad (4-58)$$

$$E_{i,j} \Delta z - E_{i+1,j} \Delta z = -i\omega \mu H_{i+1/2,j} \cdot g_{i+1/2,j} \cdot \Delta z \cdot \cos \phi_{i+1/2,j} \quad (4-59)$$

$$E_{i-1,j} \Delta z - E_{i,j} \Delta z = -i\omega \mu H_{i-1/2,j} \cdot g_{i-1/2,j} \cdot \Delta z \cdot \cos \phi_{i-1/2,j} \quad (4-60)$$

$$E_{i,j-1} \Delta z - E_{i,j} \Delta z = i\omega \mu H_{i,j-1/2} \cdot g_{i,j-1/2} \cdot \Delta z \cdot \cos \phi_{i,j-1/2} \quad (4-61)$$

The equation set is also equivalent with the circuit equations under the variable change

$$E_{i,j} \sim V_{i,j} \quad i\omega \epsilon S_{i,j} \sim Y_{i,j} \quad (4-62)$$

$$H_{i,j-1/2} \cdot l_{i,j-1/2} \sim I_{i,j-1/2} \quad R_{i+1/2,j} = \frac{i\omega \mu g_{i+1/2,j} \cos \phi_{i+1/2,j}}{l_{i+1/2,j}} \quad (4-63)$$

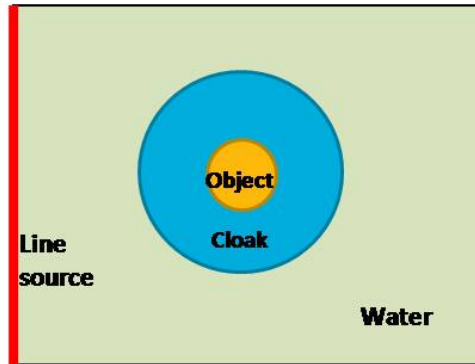
$$H_{i,j+1/2} \cdot l_{i,j+1/2} \sim I_{i,j+1/2} \quad R_{i-1/2,j} = \frac{i\omega \mu g_{i-1/2,j} \cos \phi_{i-1/2,j}}{l_{i-1/2,j}} \quad (4-64)$$

$$H_{i+1/2,j} \cdot l_{i+1/2,j} \sim -I_{i+1/2,j} \quad R_{i,j-1/2} = \frac{i\omega \mu g_{i,j-1/2} \cos \phi_{i,j-1/2}}{l_{i,j-1/2}} \quad (4-65)$$

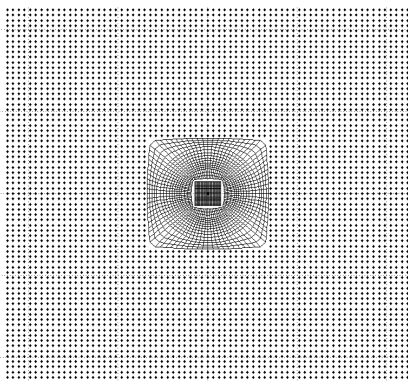
$$H_{i-1/2,j} \cdot l_{i-1/2,j} \sim -I_{i-1/2,j} \quad R_{i,j+1/2} = \frac{i\omega \mu g_{i,j+1/2} \cos \phi_{i,j+1/2}}{l_{i,j+1/2}} \quad (4-66)$$

The nonorthogonal circuit network is employed to simulate a cylindrical acoustic cloak in a background medium with square boundary, which is water here. At each node, there are four serial inductors and one shunt capacitors. The mesh of the background water is divided into two parts. One part closer to the cloak is discretized by nonorthogonal mesh. On the other hand, the background is meshed by uniform square mesh away from the cloak. The cloak is meshed by nodes along the diagonal direction of a cylindrical coordinate. Similar to the background medium, the object is composed of nonuniform mesh closer to the cloak and square mesh in the center. In Figure 4-9 (c), the red dots marked the nodes of the dual cells. The circuit cells shown in Figure 4-9 (d) and (e) are the employed for cloak and the square mesh respectively.

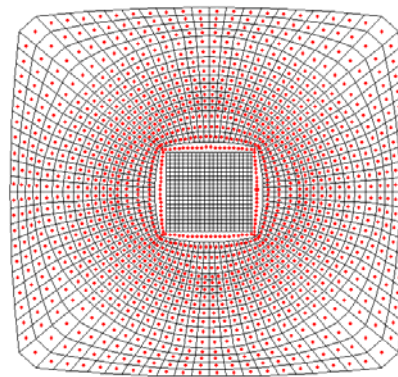
A plane acoustic wave filed impinges from the left side boundary of calculating domain. The radius of object is one wavelength and the acoustic impedance of object is set as seven times of the water. The thickness of cloak is 1.6 wavelengths. The pressure field at steadystate is shown in Figure 4-10 (a). Nearly zero amplitude is observed inside the cloak. The phase distribution is shown in Figure 4-10 (b). Inside the cloak shell, the wave is bent around the object as merged behind the object. The wave is recombined behind the cloaked object to original plane wave front. To keep the circuit stable, small number of resistor is added into the circuit in serial with the inductors. This resulted in strong acoustic intensity attenuation as observed in Figure 4-10 (a). The distortion of the phase front near the four corners of the cloak is mainly caused by the coarse nonorthogonal mesh surrounding the cloak. Due to the limit of the software, we cannot further refine this part of mesh.



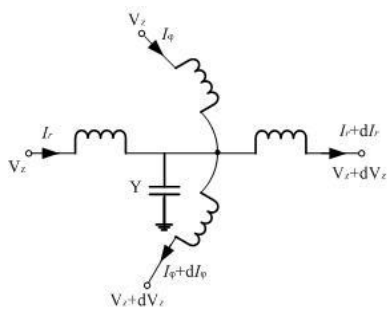
(a)



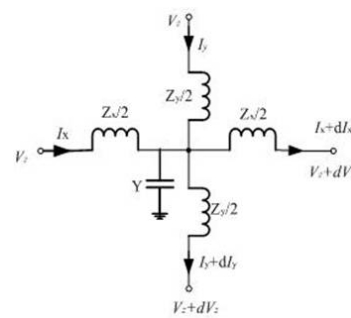
(b)



(c)



(d)



(e)

**Figure 4-9** (a) Computational domain (b) mesh model (c) and center part of the mesh model (d) one circuit unit at each mesh node for cylindrical and (e) rectangular mesh.

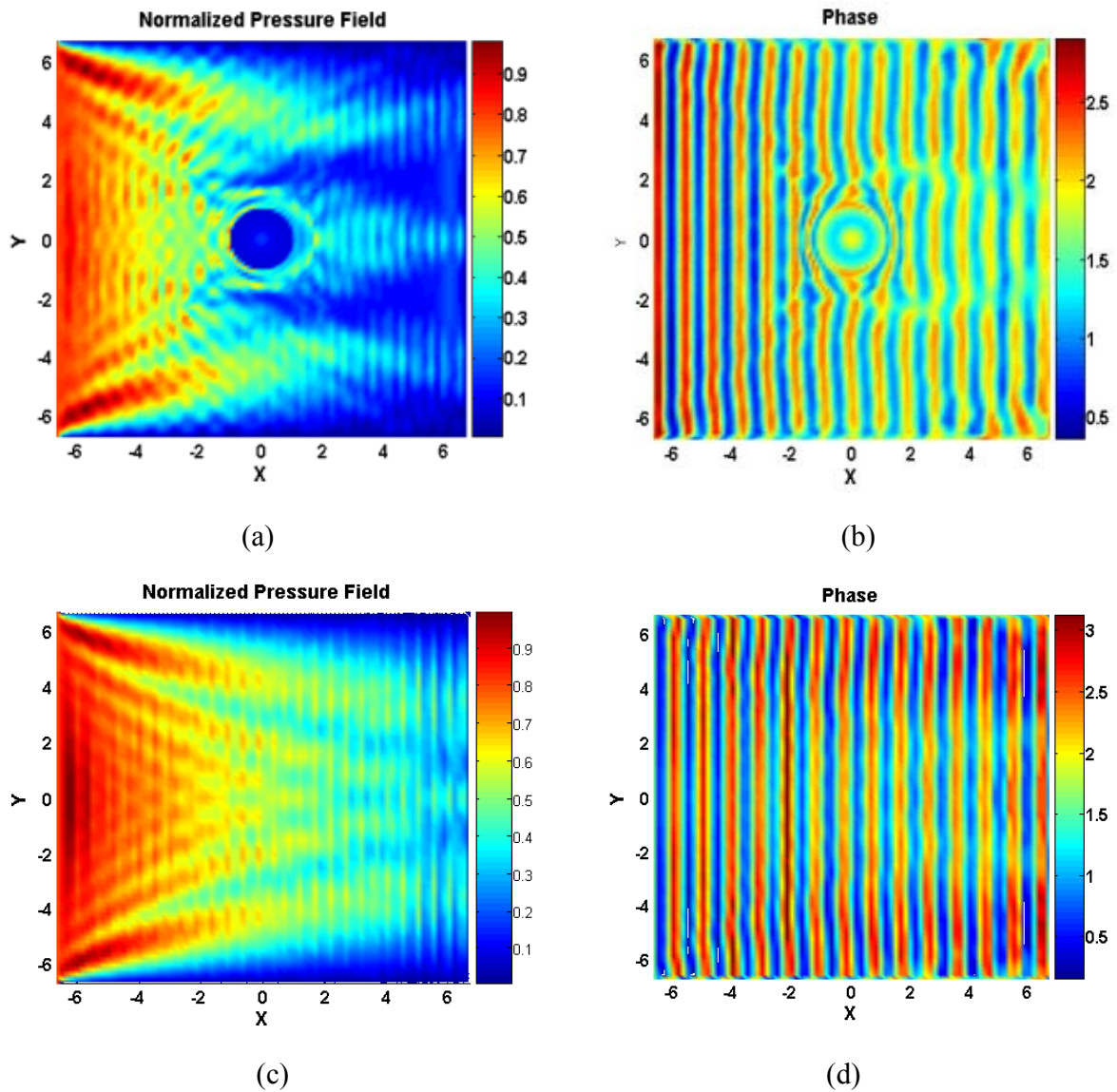


**Figure 4-10** Pseudo colormap of (a) a scaled pressure field amplitude and (b) phase distribution in the vicinity of the cloaked object (c) a scaled pressure field amplitude and (d) phase distribution in a free water space.

Figure 4-10 (c) and Figure 4-10 (d) show the pressure field amplitude and phase distributions at steady state of a free water space with the same mesh nodes as in Figure 4-10(a). Same field attenuation is observed in Figure 4-10 (c) while the much less distortion in phase

front is presented in Figure 4-10 (d) compared with Figure 4-10 (b).

## 4.6 Experimental Study of Acoustic Cloak Based on Transmission Line Model

### 4.6.1 Experimental Setup and Data Acquisition

In our design, the 2D acoustic metamaterial cloak is designed to squeeze the cylindrical region  $0 < r < R_2$  into an annular region  $R_1 < r' < R_2$  where  $r$  and  $r'$  are the radial coordinate in the original and transformed system respectively. The acoustic waves are thus excluded from the extended volume and smoothly bent inside the cloak, with no perturbation of exterior field. We choose the inner and outer radius of the cloak as  $R_1 = 13.5\text{mm}$ ,  $R_2 = 54.1\text{mm}$ . Because of the form invariance of the 2D acoustic wave equation, this given warping of space can be achieved by providing the desired distribution of the mass density and compressibility in the annular region interpreted as

$\frac{\rho_r}{\rho_w} = \frac{r}{r-R_1}$      $\frac{\rho_\phi}{\rho_w} = \frac{r-R_1}{r}$      $\frac{\beta}{\beta_w} = \left(\frac{R_2}{R_2-R_1}\right)^2 \frac{r-R_1}{r}$ . To facilitate the experimental realization of the cloak, we used the simplified functional form of the material parameters as  $\frac{\rho_r}{\rho_w} = 0.5$

$\frac{\rho_\phi}{\rho_w} = 0.5 \left(\frac{r-R_1}{r}\right)^2$      $\frac{\beta}{\beta_w} = 2 \left(\frac{R_2}{R_2-R_1}\right)^2$  as plotted in Figure 4-12 (b) which can keep the same wave behavior inside the cloak due to the scalar wave nature of the 2D acoustic wave in fluid .

The acoustic metamaterial cloak with the above material specification is physically synthesized by a planar network of acoustic circuits machined in an aluminum plate as shown in Figure 4-12 (a). These building blocks are cascaded in a lattice configuration which is diagonal in a cylindrical basis. In such a topology, the cloak is approximated by sixteen homogeneous concentric cylinders. From the first to the fourth layers, the unit cell size along radial direction is  $\lambda/7$ ,  $\lambda/8$ ,  $\lambda/9$  and  $\lambda/9$  ( $\lambda$  is the wavelength in water at 60 kHz) respectively. Afterwards, the

cylinder layers are evenly spaced with the distance equal to  $\lambda/10$  along the radial direction. On the other hand, the first cylinder near the inner lining of the cloak is divided to 32 units around the circumference. To keep the size of the constituent element smaller than  $\lambda/10$  along circumferential direction, starting from the second layer, the number of cells is doubled to 64, and further increased to 128 from the sixth layer. The geometry of the sample is listed in table 1. For all the unit cells, the depth and width of the channels  $w_r, t_r, w_\phi, t_\phi$  are constant value of 0.5mm. The inner radius of the cloak is 13.5mm. We noted that with the same design approach, cloak with larger inner radius is feasible, but with much larger number of unit cells needed to build the cloak.

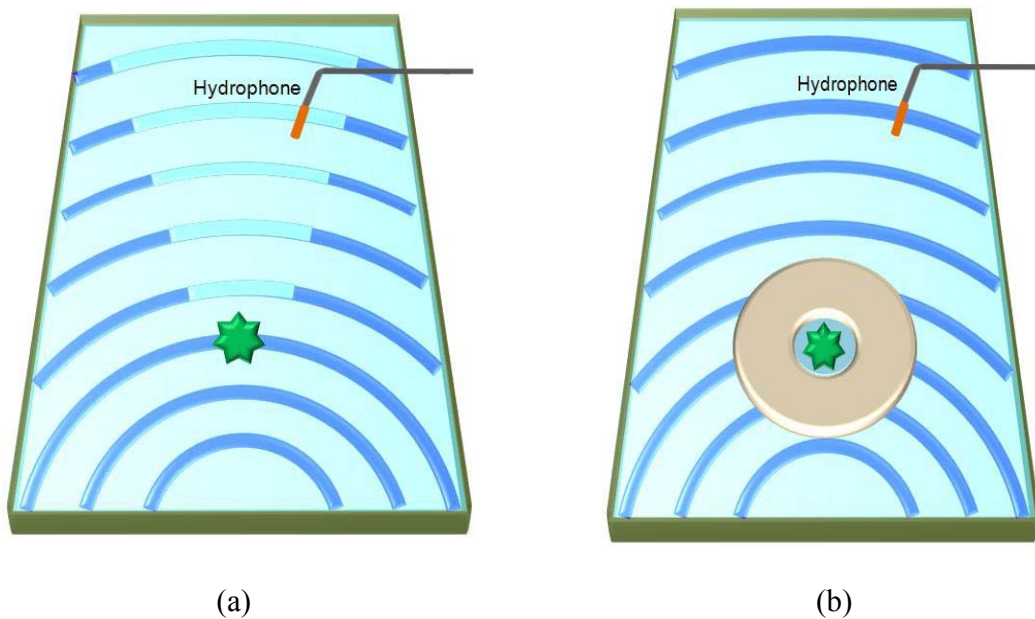
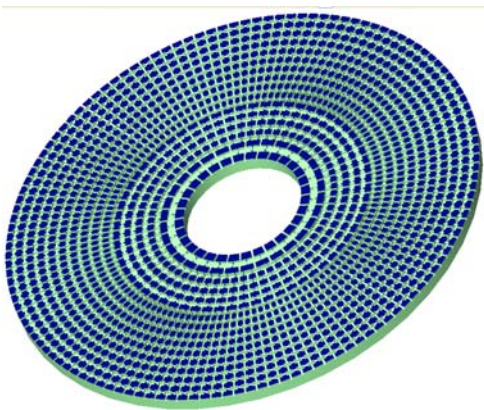


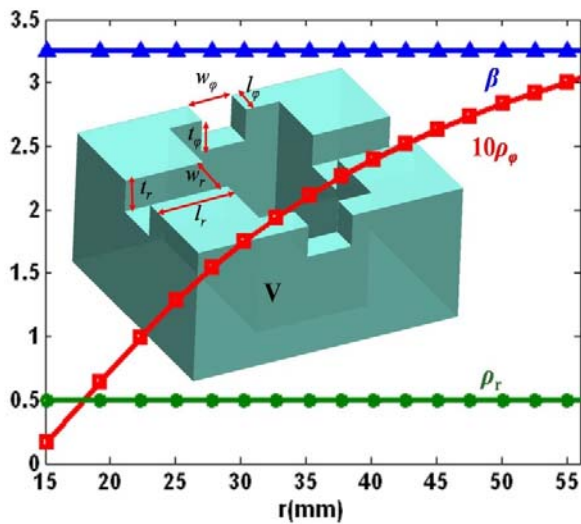
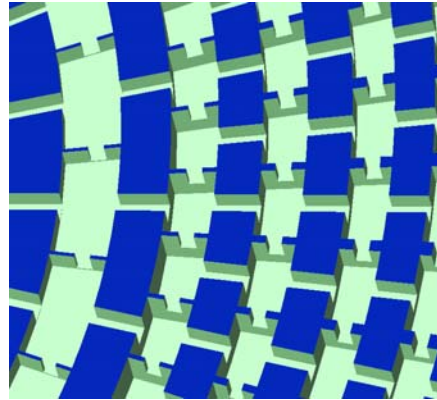
**Figure 4-11** Schematic diagram of the experimental setup. A burst of monotonic signal with a width of twenty periods was used to drive the transducer as an underwater point source in the water tank. One needle-sized hydrophone detected the ultrasonic signals in the immediate environment of (a) the object and (b) the cloaked object.

In our experiment, the water-filled network structure behaves as an effective anisotropic medium for incoming underwater ultrasound. In each unit cell as shown in Figure 4-12 (b), the cavity with large volume in center works as an acoustic capacitor whereas the channels connecting it to the four neighboring cavities act as serial inductors<sup>28,29,30</sup>. As each unit cell is only around one-tenth of the wavelength at operating frequency of 60 kHz, the network can be characterized as an effective medium with correspondence between effective density and serial inductance ( $L_r, L_\phi$ ) and between compressibility and shunt capacitance (C). The relation can be interpreted in forms of  $\rho_{eff,r} = \frac{L_r S_r}{\Delta r}$ ,  $\rho_{eff,\phi} = \frac{L_\phi S_\phi}{r \Delta \phi}$  and  $\beta_{eff} = \frac{C}{S_r \Delta r}$ . This analogy effectively describes the realization of the metamaterial cloak with the spatially varying parameter profile by tailoring the geometry of the corresponding building blocks as listed in Figure 4-12 (c). Please note that the effective mass density  $\rho_{eff,r}$  is mainly a measure of response through water flow in the narrow channels to the pressure gradients along the radial direction. Since the volume of water in such narrow channels is very small with respect to the whole unit cell, the effective mass density along the radial direction for the building block appears to be smaller than the density of bulk water, which is rather a constant. A similar argument can be applied for the effective density  $\rho_{eff,\phi}$  along the angular direction. Therefore the anisotropy of mass density is readily introduced in our metamaterial cloak. On the other hand, the effective medium displays an effective dynamic compressibility larger than that of filling water, because it depends on the compliance of the large cavity in between the connecting channels. The combination of the above low effective density and large compressibility give rise to a large sound speed (about 5.5 times of the speed of sound in water) along angular direction at the inner boundary of the cloak, without

relying on resonance. Such a large speed is critical for rerouting the paths of underwater sound around the cloaked object without significant scattering. Such non-resonant scheme is not yet achieved in the optical cloaking experiments.



(a)



(b)

Layer	$l_r$ (mm)	$l_\phi$ (mm)	$V$ (mm <sup>3</sup> )
1	2.05	0.10	3.00
3	1.37	0.22	2.29
5	1.24	0.41	2.06
7	1.24	0.30	2.06
9	1.24	0.41	2.06
11	1.24	0.52	2.06
13	1.24	0.63	2.06
15	1.24	0.74	2.06

(c)

**Figure 4-12** A 2D acoustic cloak for underwater ultrasound waves. (a) The configuration of the acoustic cylindrical cloak synthesized by an acoustic transmission line, namely serial inductors

and shunt capacitors. The inset is the expanded view of the network. The cavities with large volume work as shunt capacitors and those cavities are connected by narrow channels that act as the serial inductors. (b) One building block of the acoustic circuit, each unit cell consists of one large cavity in the center with channels connecting to the four neighboring blocks. The reduced cloaking parameters are used in the design. The density  $\rho_r$ , compressibility  $\beta$  have constant values and  $\rho_\phi$  increases as radius changes from  $R_1=13.5\text{mm}$  to the  $R_2=54.1\text{mm}$ . (c) The geometry parameters of the building blocks in the layers with odd number are presented in the table. The depth and width  $t_r, w_r$  and  $t_\phi, w_\phi$  of the channels along radial and angular directions have constant values of 0.5mm.

To demonstrate the shielding phenomena, the sample in Figure 4-13 is placed in a water tank to measure the pressure fields in the immediate environment of the cloaked object to compare with those without cloak. The tank edge is filled with absorbing rubber to reduce reflection. Because of the high impedance contrast between water and air as well as between water and glass, the system provides a 2D waveguide to confine the ultrasound wave propagation. Figure 4-14 presents the pressure field distribution at 60 kHz without any object in the water tank. The side of the cloak machined with the network structure is placed against the bottom of the tank. The cloak has a thickness of 3mm with the depth of the cavities smaller than 1.36 mm. The water inside the cloak is connected to the surrounding water which is 1.5 mm deep through the channels along the radial direction around the outer boundary of the cloak.

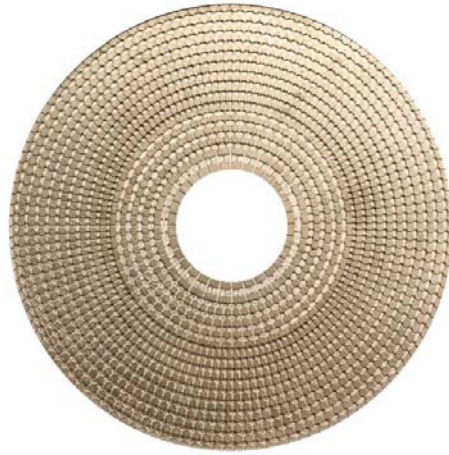


**Figure 4-13** 2D acoustic cloak based on acoustic circuit network

The ultrasound signal from a spherical shape transducer is launched to the water as a point source. A waveform generator (Tektronix AFG 310) is used to drive the transducer. The source generated a burst of sine waves with a width of 20 periods. The pressure field around the cloak sample in the water is detected by a miniature hydrophone (RESON TC4038-1), amplified by Stanford research systems model SR650 and captured using a digital oscilloscope (Agilent DSO6104A) and then downloaded to a computer for post processing and analysis. The hydrophone is attached to a motorized translation stage. The control program of a customized LabVIEW scans across the data acquisition region by moving the hydrophones in a small increment 3mm to record the spatiotemporal distribution of the pressure field. The snapshot of the field pattern can be plotted as a function of position. To verify the broad operational bandwidth of the acoustic cloak, the transducer is excited over a discrete set of frequencies to illuminate the sample. The transducer operating spectrum limits us to test the frequency range

from 52 kHz to 64 kHz.

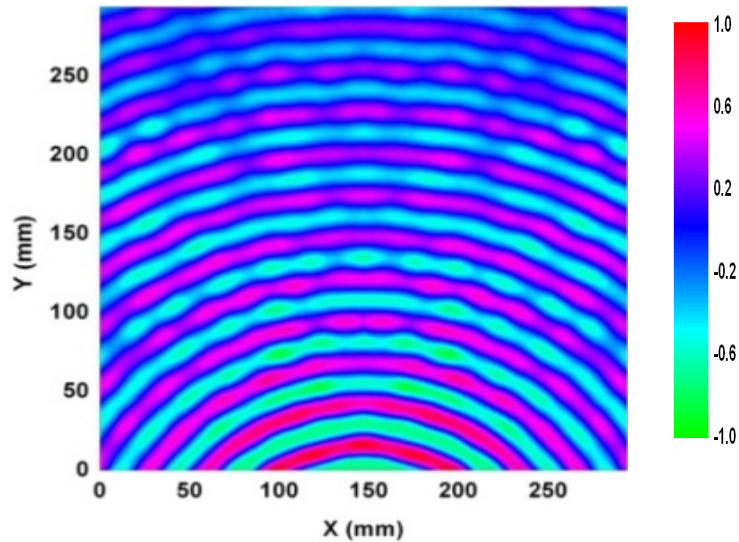
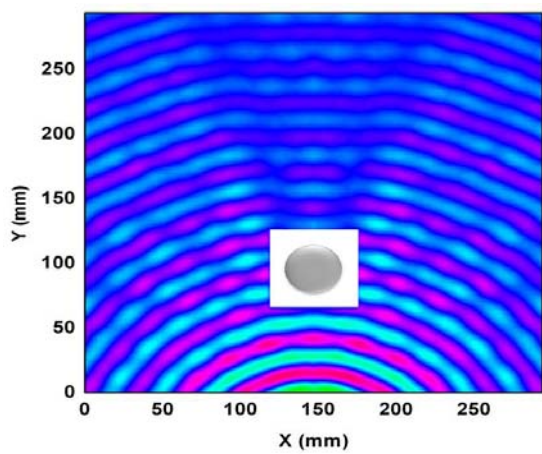


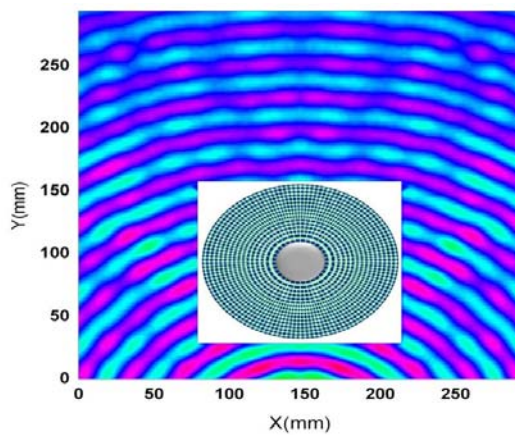
**Figure 4-14** Measured acoustic wave field distribution with a point source at 60 kHz in the water tank without any objects

#### 4.6.2 Results and Discussion

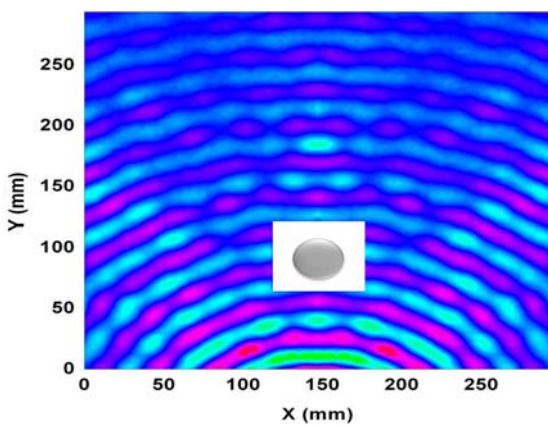
For experimental confirmation of the cloaking performance, we placed an object in a water tank and compared the wavefronts of propagating ultrasound in our measurement, with or without the presence of our cloak as shown in Figure 4-11. The object is a steel cylinder with size equal to the inner radius of the cloak. The side of the cloak machined with the metamaterial network was placed against the bottom of the tank in order to seal water inside. The ultrasound waves were launched from a spherical shaped transducer as a point source with distance of 165mm (about 6.5 wavelengths) away from the center of the cloak. To map the pressure field, a hydrophone was mounted on a horizontal linear translation stages to scan in x-y directions. By stepping the hydrophone in small increments of 3mm and recording the acoustic pulse signal from the water



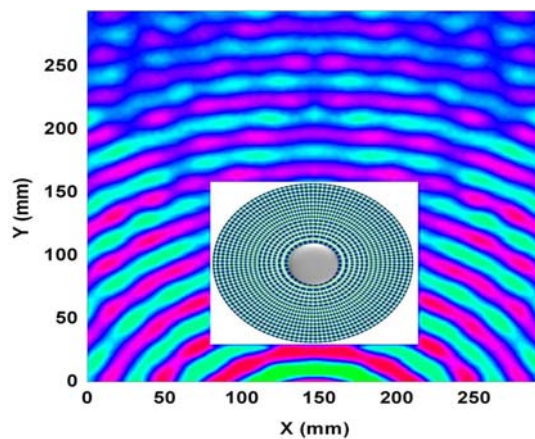
(a)



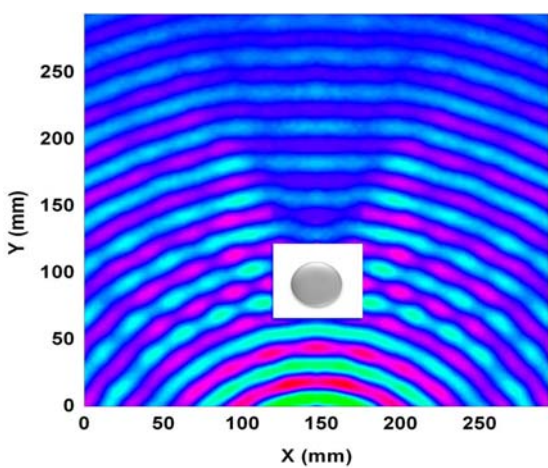
(d)



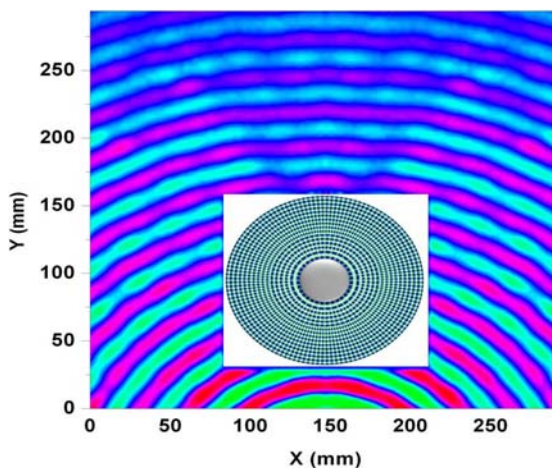
(b)



(e)



(c)



(f)

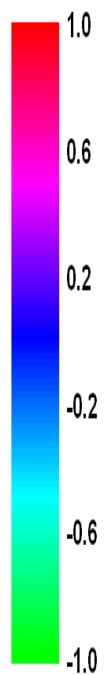


**Figure 4-15** Measured pressure field mappings of the bare steel cylinder and the cloaked steel cylinder illuminated with a point ultrasound source. The cloak lies in the center of the water tank and surrounds the steel cylinder. The scattering field patterns of the bare steel cylinder at (a) 60 kHz (b) 52 kHz and (c) 64 kHz. The pseudo colormaps in the immediate environment of the cloaked steel cylinder at (d) 60 kHz (e) 52 kHz and (f) 64 kHz.

at every step, we acquired the 2D spatial field distribution of the ultrasound wave scattering pattern.

It is evident in our experiment that the presence of steel cylinder alone in the water tank produces considerable scattering and shadowing at 60 kHz as shown in Figure 4-15 (a). By surrounding the steel cylinder with the metamaterial cloak in Figure 4-15 (d), however, the wave trajectory was restored behind the cloak with diminutive distortion in the cylindrical wavefronts, making the cloak and the hidden cylinder invisible under the hydrophone. Very small attenuation of the transmitted fields is observed on the exit side of the cloak, demonstrating the low-loss nature of the metamaterial cloak based on transmission line model.

To demonstrate the broadband nature of our designed cloak, the acoustic wave field distributions at 52 kHz and 64 kHz are presented in Figure 4-15 (b) (c) (e) (f) for both cases with and without cloak. The field maps from these measurements present similar cloaking behavior with those at 60 kHz. This is not surprising since our metamaterial cloak is constructed by non-resonant elements. Theoretically, the cloak is expected to operate over a wide frequency range of 40 to 80 kHz. In fact, at frequency below 40 kHz, the scattering from the object with

radius of 13.5mm become negligible. At the same time, the effectiveness of cloak at high frequency is restricted by two factors. The first is the breakdown of the effective medium approximation at 120 kHz when the unit cell is comparable to one quarter of wavelength. By using smaller size of unit cells, this limit can be lifted to higher frequency. The other limit is the cutoff frequency at 80 kHz due to the low-pass topology of the circuit network. By modifying the geometry of the building block, this cutoff frequency can be potentially extended. However, in the current experiment we can only verify the cloaking behavior from 52 to 64 kHz in the experiment due to the limited operating frequency range of the transducer. Figure 4-16 presented the acoustic wave field maps at different frequency to demonstrate the cloaking functionality. The scattering shadow caused by the steel cylinder as shown in Figure 4-16 (a-d) is reduced by the surrounding cloak in Figure 4-16(e-h) at frequency 54, 56, 58 and 62 kHz respectively.

To further quantify the reduction of scattering and shadowing of the cloaked object, we conducted a set of measurements over different frequencies. The peak values of pressure along the wavefronts behind the cloak were obtained using a MATLAB program to process the experimental data. To facilitate the comparison of the cloaking performance, we defined the averaged visibility of an object as  $\bar{\gamma} = \sum_{j=1}^n \gamma_j$ , where  $\gamma_j = \frac{P_{\max,j} - P_{\min,j}}{P_{\max,j} + P_{\min,j}}$ ,  $P_{\max,j}$  and  $P_{\min,j}$  are the maximum and minimum peak values along the wavefront numbered by  $j$ . This can be compared to the traditional measurement of so-called scattering cross-sectional area, but performed for the convenience of the near field measurement and limited field of view in our experiment setup. Figure 4-17 (a) shows one example of the measured peak pressure at 60 kHz

along one wavefront on the exit side of the object for both cases with and without cloak. This wavefront is near the boundary of the cloak between  $y = 100\text{mm}$  and  $y = 170\text{mm}$ . In Figure 4-17 (b), the averaged visibility of the cloaked object over all the wavefronts on the exit side is compared with the one with only bare cylinder. The comparison clearly indicates that the cloak preserves good shielding effectiveness over a broad frequency range even with impedance mismatch at the outer interface of the cloak. We can read the visibility of 0.62 for the bare steel cylinder, whereas the visibility of the cloaked steel cylinder is reduced to 0.32 at 60 kHz, showing significant reduction in scattering and shadowing. The reduced visibility of the cloaked object is further confirmed by 2D numerical simulation using commercial finite-element method software COMSOL. In the finite element model, the cloak is approximated by sixteen layers of homogeneous cylinders with reduced cloaking parameters. In order to match the measured visibility at 60 kHz, a small attenuation of 5.8dB/m is empirically determined and added in the simulated cloak model. The good agreement between the numerical and experimental results indicates the effectiveness of our low-loss metamaterial over a wide range of frequency.

As a control experiment, we measured the field pattern scattered by a steel cylinder with the same dimension as the cloak but with no network structure at 60 kHz. The result is shown in Figure 4-18, strong scattering and large shadow area are observed behind the cylinder. The visibility of this cylinder is 1.38, which is much larger than 0.32 for the cloaked object whereas the hidden object in center has visibility of 0.56. This demonstrates that the steel cylinder without the designed structure actually causes more significant scattering than the smaller cylinder which

is hidden inside the cloak. Only with the machined building blocks, the cylindrical cloak can guide the acoustic wave to reform the wavefronts on the exit side.

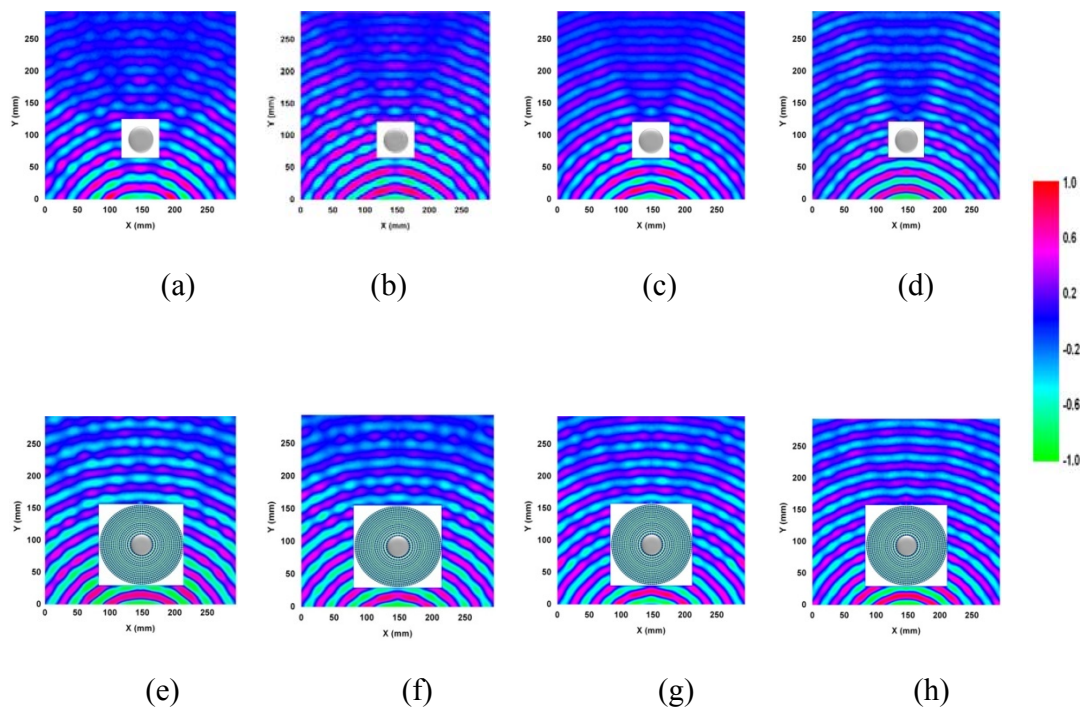


**Figure 4-16** Measured acoustic wave field mappings of two cases: with bare steel cylinder at (a) 54 kHz (b) 56 kHz (c) 58 kHz and (d) 62 kHz and when the steel cylinder is surrounded by the metamaterial cloak at (e) 54 kHz (f) 56 kHz (g) 58 kHz and (h) 62 kHz.

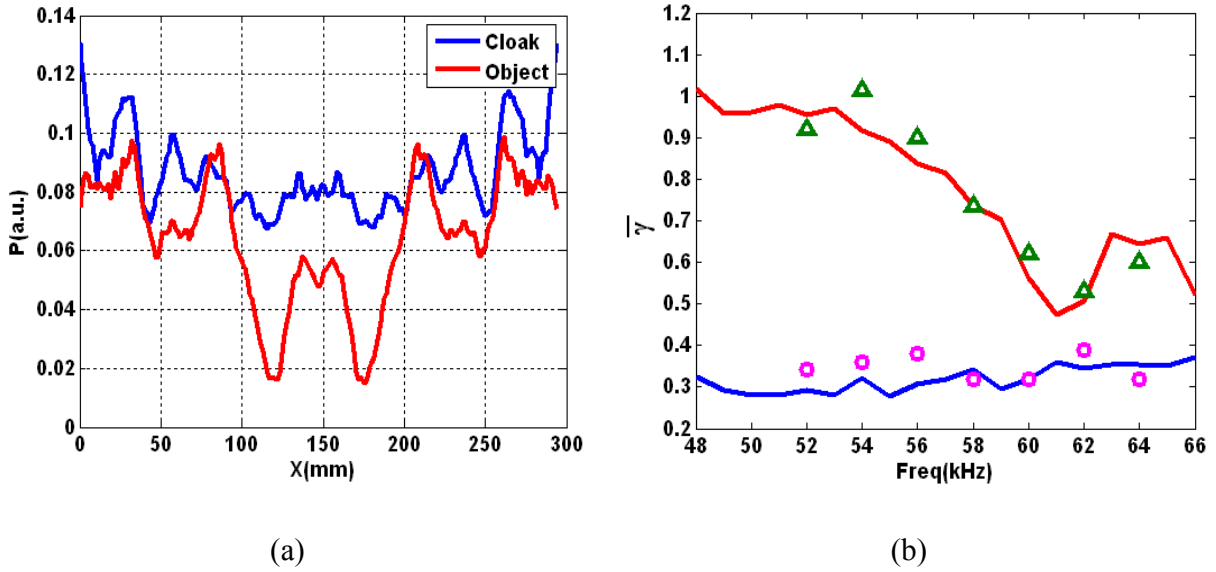


**Figure 4-17** Frequency dependence of the averaged visibility of the steel cylinder with and without the acoustic cloak. (a) The measured peak values of the pressure field along the wavefront lies between  $y=100$  mm and  $y=170$  mm with and without cloak at 60 kHz (b) Plot of the averaged visibility. The blue and red solid lines are calculated averaged visibility for the cases with and without cloak respectively. The 2D simulation performed using finite-element-based solver COMSOL Multiphysics. The experimental results measured with and without cloak are marked by the magenta circles and green triangular respectively.

To further demonstrate the effectiveness of our acoustic anisotropic metamaterial based on lumped circuit network, we simulated the acoustic wave propagation through the acoustic circuit network to compare with the results using finite element method (FEM) software COMSOL. In the FEM model, the cloak is approximated by 16 layers of homogeneous cylinders with the reduced cloaking parameters. In the circuit model, the cloak, hidden cylinder and the background

water are all discretized and simulated by the circuit network. The number of unit cells for the cloak is set as same as the sample in the experiment. Comparison of Figure 4-19 (a) and (b) indicates a good match between those two numerical approaches. More distortion is observed in the circuit model in Figure 4-19 (b). This is mainly due to the difference in the boundary conditions. In COMSOL model, perfect matched layer is utilized to have zero reflection from the boundary, while in the circuit model the matching resistors are used to terminate the cells in the boundary.

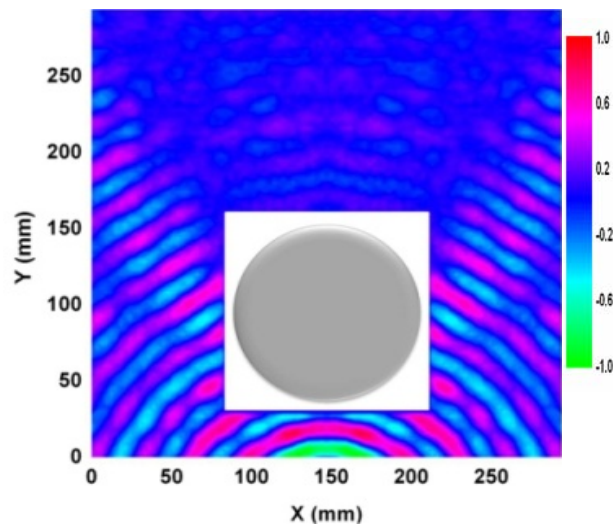


**Figure 4-18** Measured acoustic wave field distribution in the vicinity of a steel cylinder with the same geometry as the cloak

In Figure 4-20, the scattering from the cloaked object and the bare object to different directions is simulated using COMSOL at frequency 60 kHz. The plot indicates that the backscattering from the cloaked object is strongly reduced and also the forward scattering is considerably lower than that of the bare object. Due to the limited size of the water tank, we cannot measure the field between the source and the sample to study the backscattering. Refer to Appendix D for

numerical study using FEM.

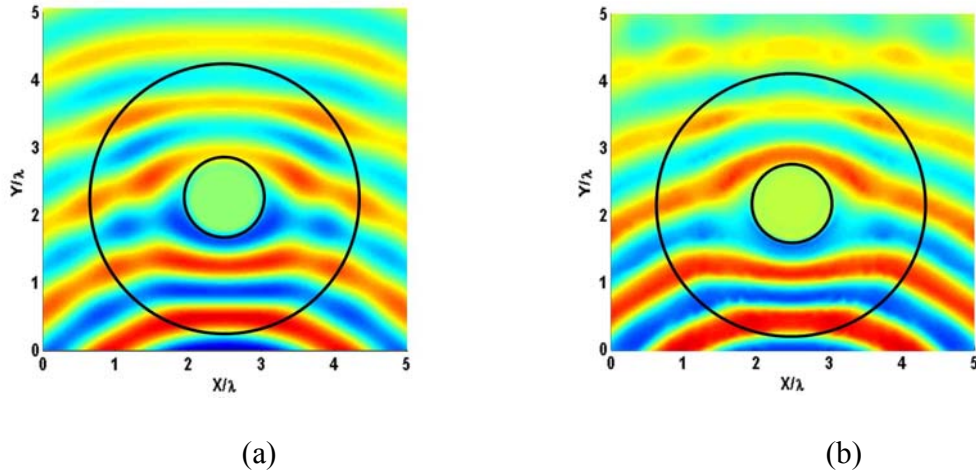


**Figure 4-19** 2D simulations for the acoustic cloak with reduced material parameters with black lines indicating the inner and outer boundary of the cylindrical cloak. (a) The FEM simulation by software COMSOL. The cloak is approximated by 16-step piecewise homogeneous cylinders. (b) Lumped circuit model simulation of the cylindrical cloak performed by software SPICE.

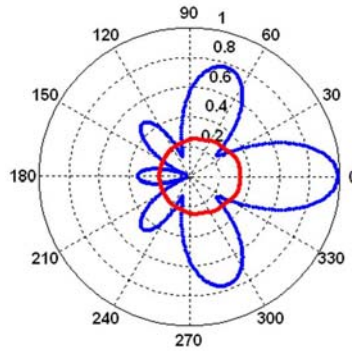


**Figure 4-20** Simulated scattered pressure field to different directions from the cloaked object (red line) and the bare object (blue line) at frequencies 60 kHz. The plots are normalized to the maximum value of the scattered pressure field of the bare object. The plane wave that illuminates the cloaked/bare object travels in the direction  $\varphi = 0$ .

### 4.6.3 Conclusion

In conclusion, we have demonstrated a 2D acoustic cloak that can significantly reduce the visibility of the hidden object from underwater acoustic waves. This underwater acoustic cloak can be readily implemented by a network of anisotropic acoustic transmission line. Such a new class of acoustic metamaterial is built from non-resonant elements and offers a wide range of effective density and compressibility that are not available by the constituent materials over a broad frequency range. Moreover, this transmission line approach may have potential applications for a myriad of fascinating devices beyond cloaking based on coordinate transformation.

### References

---

<sup>1</sup> Pendry J B, Schurig D and Smith D R, “Controlling Electromagnetic Fields”, *Science* **312**, 1780 (2006).

<sup>2</sup> U. Leonhardt, “Optical Conformal mapping”, *Science* **312**, 1777 (2006).

<sup>3</sup> A. V. Kildishev, V. M. Shalaev, “Engineering space for light via transformation Optics”, *Opt. Lett.* **33**, 43 (2008).

<sup>4</sup> M. Rahm, S. A. Cummer, D. Schurig, J. B. Pendry, “Optical Design of Reflectionless Complex Media by Finite Embedded Coordinate Transformations”, D. R. Smith, *Phys. Rev. Lett.* **100**, 063903 (2008).

---

<sup>5</sup> M. Rahm et al., “Transformation-optical design of adaptive beam bends and beam expanders”, *Opt. Express* **16**, 11555 (2008).

<sup>6</sup> Smith, D. R., Padilla, W. J., Vier, D. C., Nemat-Nasser, S. C. & Schultz, S. “Composite medium with simultaneously negative permeability and Permittivity”. *Phys. Rev. Lett.* **84**, 4184 (2000).

<sup>7</sup> Smith, D. R., Pendry, J. B. & Wiltshire, M. C. K. “Metamaterials and negative refractive index”. *Science* **305**, 788\_792 (2004).

<sup>8</sup> Schurig D *et al*, “Metamaterial Electromagnetic Cloak at Microwave Frequencies” , *Science* **314**, 977 ( 2006 ).

<sup>9</sup> Cai, W., Chettiar, U. K., Kildishev, A. V. & Shalaev, V. M. , “Optical cloaking with metamaterials”, *Nature Photon.* **1**, 224–227 (2007)

<sup>10</sup> Alu, A. & Engheta, N., “ Multifrequency optical invisibility cloak with layered plasmonic shells”, *Phys. Rev. Lett.* **100**, 113901 (2008).

<sup>11</sup> Leonhardt, U. & Tyc, T. Broadband invisibility by non-euclidean cloaking. *Science* **323**,

---

110–112 (2009).

<sup>12</sup> Li Jensen and Pendry J. B., “Hiding under the Carpet: A New Strategy for Cloaking”, *Phys Rev Lett.* **101**, 203901 (2008).

<sup>13</sup> Alitalo, P., et al., *Appl. Phys. Lett.* **94**, 014103 (2009).

<sup>14</sup> R. Liu, *et al.*,” Broadband Ground-Plane Cloak”, *Science* **323**, 366 (2009).

<sup>15</sup> J. Valentine *et al.*, “An optical cloak made of dielectrics”, *Nature Material* **2461**, (2009).

<sup>16</sup> Cummer SA *et al.*, “Scattering theory derivation of a 3D acoustic cloaking shell”, *Phys Rev Lett.* **100**, 024301(2008).

<sup>17</sup> S.Zhang et al , “Cloaking of matter waves”, *Phys.Rev. Lett* **100**, 123002 (2008).

<sup>18</sup> M. Farhat, S. Enoch, S. Guenneau, and A. B. Movchan, “Broadband Cylindrical Acoustic Cloak for Linear Surface Waves in a Fluid”, *Phys.Rev. Lett.* **101**, 134501 (2008).

<sup>19</sup> Milton G W, Briane M and Willis J R, “On cloaking for elasticity and physical equations with a transformation invariant form”, *New J. Phys.* **8**, 248 (2006).

- 
- <sup>20</sup> Pendry J .B .and Li Jensen, “An acoustic metafluid: realizing a broadband acoustic cloak”, *New J. Phys.* **10** 115032 (2008).
- <sup>21</sup> Chen H and Chan C T, “Acoustic cloaking in three dimensions using acoustic metamaterials”, *Appl. Phys. Lett.* **91**, 183518 (2007).
- <sup>22</sup> Cheng Y, Yang F, Xu J Y and Liu X J, *Appl. Phys. Lett.* **92**, 151913 (2008).
- <sup>23</sup> S. A. Cummer and D. Schurig, “One path to acoustic cloaking”, *New J. Phys.* **9**, 45 (2007).
- <sup>24</sup> N. Fang, D. Xi, J. Xu et al., “Ultrasonic Metamaterials with Negative Modulus”, *Nature Materials*, **5**,452-456 (2006).
- <sup>25</sup> S. Zhang, L.Yin, and N. Fang, “Focusing Ultrasound with an Acoustic Metamaterial Network”, *Phys. Rev. Lett.* **102**, 194301 (2009).
- <sup>26</sup> U. Leonhardt and T. G. Philbin, “General relativity in electrical engineering,” *New J. Phys.* **8**, 247 (2006).
- <sup>27</sup> D. Schurig, J. B. Pendry, and D. R. Smith, “Transformation-designed optical elements,” *Opt. Express* **15**, 14772- 14782 (2007).

---

<sup>28</sup> G. W. Stewart, “Acoustic wave filters”, *Phys.Rev.***20**,528 (1922).

<sup>29</sup> L.L.Beranek, *Acoustics*, 1954, McGRAW-HILL,New York.

<sup>30</sup> L. E. Kinsler, *Fundamentals of Acoustics*, 1982, Wiley,New York.

## 5 SUMMARY AND FUTURE WORK

### 5.1 Summary

A novel approach was designed in this thesis to build an acoustic metamaterial for different applications. Since the inception of the term metamaterials, acoustic metamaterials have been explored theoretically but there has been little headway on the experimental front. In this work, we demonstrated that a distributed acoustic system can be effectively described by the analogous lumped circuit model in which the behavior of the current resembles the motion of the fluid. Based on this analogy, an acoustic metamaterial can be implemented by a two-dimensional transmission line network to realize negative refractive index and further inhomogeneous anisotropic density and compressibility.

In one application, a PI/NI interface is constructed by a two-dimensional array of acoustic circuit network. The ultrasound waves from a point source were brought to a focus point through the NI metamaterial lens. The unit cell of the acoustic network is only one eighth of the operating wavelength, making the lens in a compact size. Compared with conventional lenses, the flat thin slab lens takes advantages in that there is no need to manufacture the shapes of spherical curvatures and the focus position is insensitive to the offset of source along the axis. Also this negative index lens offers tunable focal length at different frequencies.

Another more interesting metamaterial device, acoustic cloak, is studied both numerically

and experimentally in this thesis. This underwater acoustic cloak is constructed by a network of anisotropic acoustic transmission line. As a result of the non-resonant nature of the building blocks, this acoustic cloak can significantly reduce the visibility of the hidden object over a wide range of frequency. Moreover, this transmission line approach may have potential applications for a myriad of fascinating devices beyond cloaking based on coordinate transformation.

## **5.2 Future work**

Amazing progress has been made in metamaterial over the past few years. This new concept provides great opportunities in the design and development of exotic functional materials and devices. Many applications in optical and acoustic wave fields have been proposed and demonstrated. In ultrasound, the realization of high-resolution acoustic imaging is a key for nondestructive testing and medical screening. The negative index metamaterial provides an unprecedented opportunity for high-resolution ultrasound imaging. The loss in current circuit model is one of the key limitations from beating the diffraction limit. To decrease the size of the building blocks, which is essential to achieve sub-wavelength resolution, new fabrication method could be employed.

The new design paradigm of transformation optics offers enormous way to control the wave propagation by providing a desired spatial distribution of material parameters. Beyond cloaking, a myriad of fascinating devices can be investigated in the future, such as power concentrator,

wave bends and beam expanders. Also, there is much more ground to investigate for the future such as nonlinear, optic-acoustic device.

The current circuit model is the first-order linear approximation of the corresponding distributed acoustic system. With the increase of the acoustic energy, higher-order and nonlinear effect should be taken into account to make the analogy more accurate.

## APPENDIX A: LUMPED CIRCUIT MODEL

Following the development of electrical filters, G.W. Stewart studied showed the combination of tubes and resonators could be devised in a way very similar to electrical circuit filter. In the model, the acoustic elements are much smaller than the wavelength such that the wave motion in these subwavelength elements need not be considered.

In 1927, W.P.Mason gave a more rigorous study of the regular combination of acoustic elements with considering the wave propagation in the elements. Also viscosity and heat conduction dissipation are taken into account.

### ***Model I:***

#### *Mason's full-wave model*

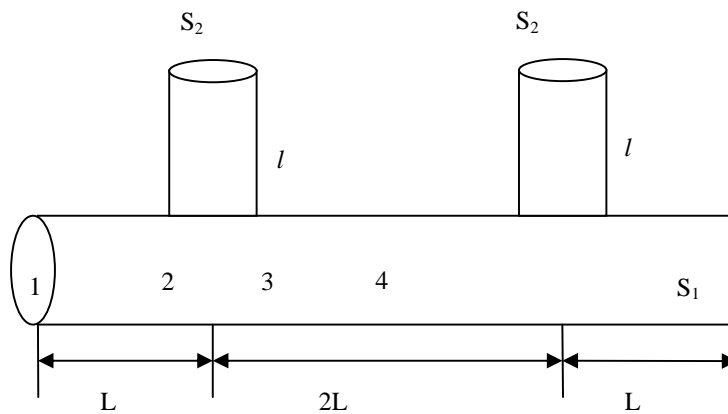


**Figure A1** Acoustic transmission line

Consider a main conduction tube with equally spaced side branches, assuming the width of the junction is much smaller than the wavelength and hence the pressure is constant in the side

branch and the main branch over the portion in the immediate contact with the side branch. Also, the sum of the volume displacement at a junction of tubes is zero.

We can derive the equations

$$\begin{bmatrix} p_4 \\ U_4 \end{bmatrix} = \begin{bmatrix} \cosh \Gamma & -\frac{Z_0}{S_1} \sinh \Gamma \\ -\frac{S_1}{Z_0} \sinh \Gamma & \cosh \Gamma \end{bmatrix} \begin{bmatrix} p_1 \\ U_1 \end{bmatrix}$$

Where  $\cosh \Gamma = (\cosh 2\alpha_1 L + \frac{Z_{L1} S_2}{2Z_s S_1} \sinh 2\alpha_1 L)$

$$Z_0 = Z_{L1} \sqrt{\frac{1 + \frac{Z_{L1} S_2}{2Z_s S_1} \tanh \alpha_1 L}{1 + \frac{Z_{L1} S_2}{2Z_s S_1} \coth \alpha_1 L}}$$

If the side branch is closed at one end

While if the side branch is open at one end

### Stewart's lumped circuit model

Consider an acoustic wave transmission line consisting of equal acoustic impedances in series, divided into sections by acoustic impedances in what might be termed shunt branches.

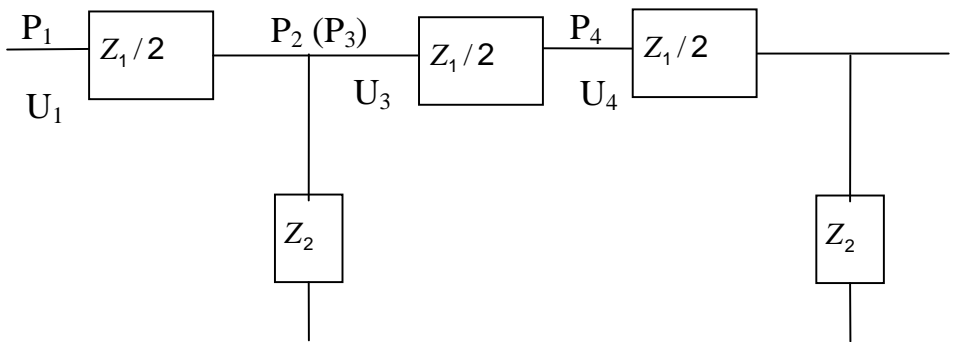


**Figure A2** Stewart's lumped circuit model

We can derive the transfer matrix for such periodic lumped model as

$$\begin{bmatrix} p_4 \\ U_4 \end{bmatrix} = \begin{bmatrix} 1 + \frac{Z_1}{2Z_2} & -(Z_1 + \frac{Z_1^2}{4Z_2}) \\ -\frac{1}{Z_2} & 1 + \frac{Z_1}{2Z_2} \end{bmatrix} \begin{bmatrix} p_1 \\ U_1 \end{bmatrix}$$

If the side branch is closed at one end  $Z_1 = i\omega L_2 = i\omega\rho_0 2L / S_1$   $Z_2 = 1/i\omega C_2 = \rho_0 c^2 / i\omega 2LS_2$

While if the side branch is open at one end  $Z_1 = 1/i\omega C_1 = \rho_0 c^2 / i\omega 2LS_1$   $Z_2 = i\omega L_2 = i\omega\rho_0 l / S_2$

There is a problem with the above equations when the side branch is open at one end and the main tube is assumed as acoustic capacitor. Assume one section of the main tube has volume  $V$ , so  $C = \frac{V}{\rho_0 c^2}$ . When we write out the transfer matrix, we divided the section into half, so each half  $\frac{C}{2} = \frac{V}{2\rho_0 c^2}$ . On the other hand, the half capacitances appears in series, and the total capacitance should be  $\frac{C}{4} = \frac{V}{4\rho_0 c^2}$ . So there are different answers as to the total capacitance.

*Model II*

*Mason's full-wave model*

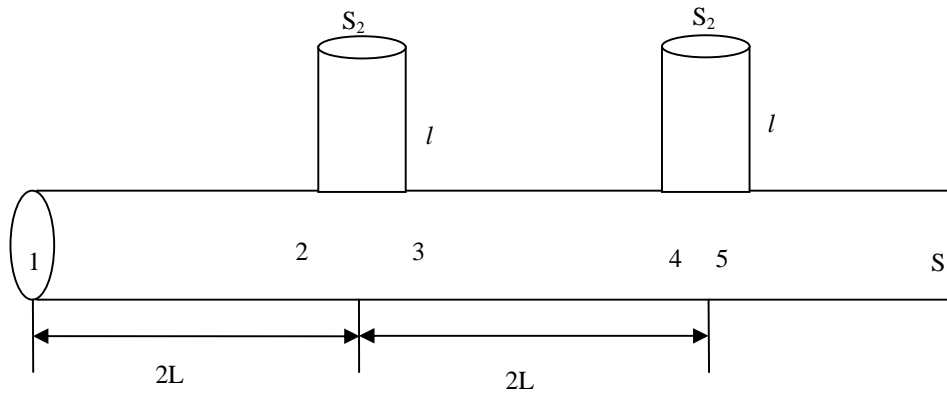


**Figure A3** Acoustic transmission line

In this model, we did not divide the main tube into half within one section, so similarly we can derive

$$\begin{bmatrix} p_4 \\ U_4 \end{bmatrix} = \begin{bmatrix} A_{11} & A_{12} \\ A_{21} & A_{22} \end{bmatrix} \begin{bmatrix} p_1 \\ U_1 \end{bmatrix}$$

$$A_{11} = \cosh 2\alpha_1 L \cosh 2\alpha_1 L + \sinh 2\alpha_1 L \sinh 2\alpha_1 L + \frac{Z_{l1} S_2}{Z_3 S_1} \cosh 2\alpha_1 L \sinh 2\alpha_1 L$$

$$A_{12} = -\frac{Z_{L1}}{S_1} \sinh 2\alpha_1 L \cosh 2\alpha_1 L - \frac{Z_{L1}}{S_1} \cosh 2\alpha_1 L \sinh 2\alpha_1 L - \left(\frac{Z_{L1}}{S_1}\right)^2 \frac{S_2}{Z_s} \sinh 2\alpha_1 L \sinh 2\alpha_1 L$$

$$A_{21} = -\frac{S_1}{Z_{L1}} \sinh 2\alpha_1 L \cosh 2\alpha_1 L - \frac{S_2}{Z_s} \cosh 2\alpha_1 L \cosh 2\alpha_1 L - \frac{S_1}{Z_{L1}} \cosh 2\alpha_1 L \sinh 2\alpha_1 L$$

$$A_{22} = \cosh 2\alpha_1 L \cosh 2\alpha_1 L + \frac{Z_{L1} S_2}{Z_s S_1} \sinh 2\alpha_1 L \cosh 2\alpha_1 L + \sinh 2\alpha_1 L \sinh 2\alpha_1 L \quad Z_{L1} = \rho_0 c_0 \quad \alpha_1 = ik$$

If the side branch is closed at one end  $Z_s = i\rho_0 c_0 \tan kl$

While if the side branch is open at one end  $Z_s = -i\rho_0 c_0 \cot kl$

*Stewart's lumped circuit model*

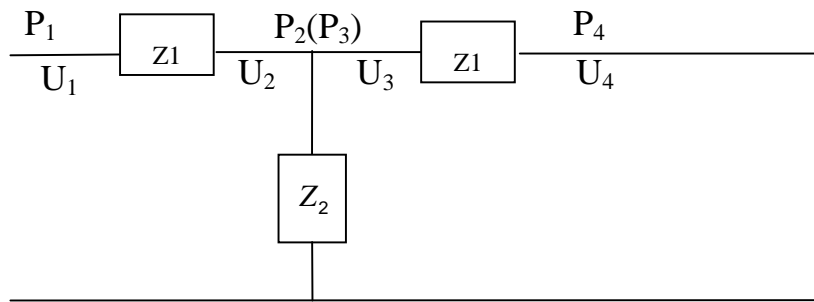


**Figure A4** Stewart's lumped circuit model

$$\begin{bmatrix} P_4 \\ U_4 \end{bmatrix} = \begin{bmatrix} 1 + \frac{Z_1}{Z_2} & -(2Z_1 + \frac{Z_1^2}{Z_2}) \\ -\frac{1}{Z_2} & 1 + \frac{Z_1}{Z_2} \end{bmatrix} \begin{bmatrix} P_1 \\ U_1 \end{bmatrix}$$

If the side branch is closed at one end  $Z_1 = i\omega L_2 = i\omega\rho_0 2L/S_1$   $Z_2 = 1/i\omega C_2 = \rho_0 c^2 / i\omega S_2$

While if the side branch is open at one end  $Z_1 = i\omega L_1 // \frac{1}{i\omega C_1} = i\omega L_1 / (1 - \omega^2 L_1 C_1) = \frac{i\rho 2L\omega / S_1}{1 - 4L^2\omega^2 / c^2}$

$$Z_2 = i\omega L_2 = i\omega\rho_0 l / S_2$$

The problem with this model is P1 and P4 are not in symmetrical positions.

### **Model III**

*Mason's full-wave model*

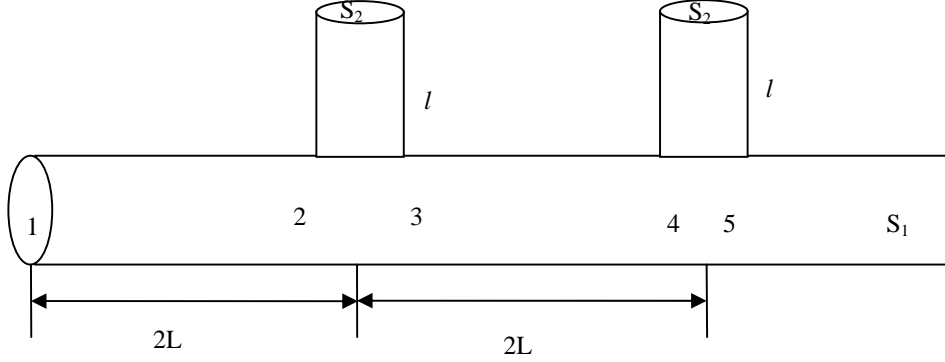


**Figure A5** Acoustic transmission line

$$\begin{bmatrix} p_3 \\ U_3 \end{bmatrix} = \begin{bmatrix} A_{11} & A_{12} \\ A_{21} & A_{22} \end{bmatrix} \begin{bmatrix} p_1 \\ U_1 \end{bmatrix}$$

$$\begin{bmatrix} p_3 \\ U_3 \end{bmatrix} = \begin{bmatrix} \cosh 2\alpha_1 L & -\frac{Z_{L1}}{S_1} \sinh 2\alpha_1 L \\ -\frac{S_1}{Z_{L1}} \sinh 2\alpha_1 L - \frac{S_2}{Z_s} \cosh 2\alpha_1 L & \cosh 2\alpha_1 L + \frac{Z_{L1} S_2}{Z_s S_1} \sinh 2\alpha_1 L \end{bmatrix} \begin{bmatrix} p_1 \\ U_1 \end{bmatrix}$$

$$A_{11} = \cosh 2\alpha_1 L$$

$$A_{12} = -\frac{Z_{L1}}{S_1} \sinh 2\alpha_1 L$$

$$A_{21} = -\frac{S_1}{Z_{L1}} \sinh 2\alpha_1 L - \frac{S_2}{Z_s} \cosh 2\alpha_1 L$$

$$A_{22} = \cosh 2\alpha_1 L + \frac{Z_{L1} S_2}{Z_s S_1} \sinh 2\alpha_1 L$$

$$\alpha_1 = ik \quad Z_{L1} = \rho_0 c_0$$

If the side branch is closed at one end  $Z_s = i\rho_0 c_0 \tan kl$

While if the side branch is open at one end  $Z_s = -i\rho_0 c_0 \cot kl$

*Stewart's lumped circuit model*

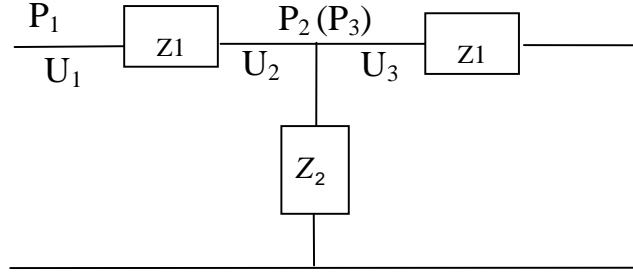


**Figure A6** Stewart's lumped circuit model

$$\begin{bmatrix} p_3 \\ U_3 \end{bmatrix} = \begin{bmatrix} 1 & -Z_1 \\ -\frac{1}{Z_2} & 1 + \frac{Z_1}{Z_2} \end{bmatrix} \begin{bmatrix} p_1 \\ U_1 \end{bmatrix}$$

If the side branch is closed at one end  $Z_1 = i\omega L_2 = i\omega\rho_0 2L / S_1$

While if the side branch is open at one end  $Z_1 = i\omega L_1 // \frac{1}{i\omega C_1} = i\omega L_1 / (1 - \omega^2 L_1 C_1) = \frac{i\rho 2L\omega / S_1}{1 - 4L^2\omega^2 / c^2}$   
 $Z_2 = i\omega L_2 = i\omega\rho_0 l / S_2$

Derivation of lumped element from Mason's full-wave model

$$\begin{bmatrix} p_3 \\ U_3 \end{bmatrix} = \begin{bmatrix} \cosh 2\alpha_1 L & -\frac{Z_{L1}}{S_1} \sinh 2\alpha_1 L \\ -\frac{S_1}{Z_{L1}} \sinh 2\alpha_1 L - \frac{S_2}{Z_s} \cosh 2\alpha_1 L & \cosh 2\alpha_1 L + \frac{Z_{L1} S_2}{Z_s S_1} \sinh 2\alpha_1 L \end{bmatrix} \begin{bmatrix} p_1 \\ U_1 \end{bmatrix}$$

$$\begin{bmatrix} p_3 \\ U_3 \end{bmatrix} = \begin{bmatrix} 1 & -Z_1 \\ -\frac{1}{Z_2} & 1 + \frac{Z_1}{Z_2} \end{bmatrix} \begin{bmatrix} p_1 \\ U_1 \end{bmatrix}$$

Compare the above two transfer matrix, to make the lumped model a good approximation for the full-wave analysis. We will need the following four conditions.

$$\cosh 2\alpha_1 L \approx 1 \tag{1}$$

$$-\frac{Z_{L1}}{S_1} \sinh 2\alpha_1 L = -Z_1 \tag{2}$$

$$-\frac{S_1}{Z_{L1}} \sinh 2\alpha_1 L - \frac{S_2}{Z_s} \cosh 2\alpha_1 L = -\frac{1}{Z_2} \tag{3}$$

$$\cosh 2\alpha_1 L + \frac{Z_{L1} S_2}{Z_s S_1} \sinh 2\alpha_1 L = 1 + \frac{Z_1}{Z_2} \tag{4}$$

Substitute (2) (3) into (4)

$$\cosh 2\alpha_1 L + \frac{Z_{L1} S_2}{Z_s S_1} \sinh 2\alpha_1 L = 1 + (\sinh 2\alpha_1 L)^2 + \frac{Z_{L1} S_2}{Z_s S_1} \sinh 2\alpha_1 L \cosh 2\alpha_1 L \quad (5)$$

If  $2\alpha_1 L$  is very small, in other words, when the periodicity is subwavelength size

$$\text{and use } \cosh x = 1 + \frac{x^2}{2!} + \frac{x^4}{4!} + \frac{x^6}{6!} \dots \quad \sinh x = x + \frac{x^3}{3!} + \frac{x^5}{5!} + \frac{x^7}{7!} \dots$$

$$\text{so } \cosh 2\alpha_1 L = 1 \quad \sinh 2\alpha_1 L = 2\alpha_1 L \rightarrow 0$$

we can rewrite (1)-(5) equations as

$$\cosh 2\alpha_1 L \approx 1 \quad (6)$$

$$Z_1 = i\omega\rho_0 \frac{2L}{S_1} \quad (7)$$

$$Z_2 = \frac{1}{i\omega \frac{2LS_1}{\rho_0 c_0^2}} \parallel \frac{Z_s}{S_2 \cosh 2\alpha_1 L} \quad (\text{In parallel}) \quad (8)$$

$$\cosh 2\alpha_1 L + \frac{Z_{L1} S_2}{Z_s S_1} \sinh 2\alpha_1 L = 1 + \frac{Z_1}{Z_2} \quad (9)$$

$$\begin{aligned} \cosh 2\alpha_1 L + \frac{Z_{L1} S_2}{Z_s S_1} \sinh 2\alpha_1 L &= 1 + (\sinh 2\alpha_1 L)^2 + \frac{Z_{L1} S_2}{Z_s S_1} \sinh 2\alpha_1 L \cosh 2\alpha_1 L \\ \Rightarrow \cosh 2\alpha_1 L + \frac{Z_{L1} S_2}{Z_s S_1} \sinh 2\alpha_1 L &= \cosh 2\alpha_1 L + \frac{Z_{L1} S_2}{Z_s S_1} \sinh 2\alpha_1 L \\ \Rightarrow 1 + \frac{Z_{L1} S_2}{Z_s S_1} \sinh 2\alpha_1 L &= 1 + \frac{Z_{L1} S_2}{Z_s S_1} \sinh 2\alpha_1 L \end{aligned} \quad (10)$$

This means when  $2\alpha_1 L$  is very small, the equation (4) is automatically satisfied. The above equation suggest the lumped circuit model based on the Mason's full wave solution as such: the series impedance is always an inductor; the shunt admittance is the capacitance with the volume of the one section of the main tube in parallel with the admittance of the side branch. This derivation is valid for both cases when the end of the side branch is open or closed.

Error analysis:

$$\cosh x \approx 1 \quad \text{when } \text{lattice} = \frac{\lambda}{19.8}, \text{ error is within 5\%}$$

$$\sinh x \approx x \quad \text{when } \text{lattice} = \frac{\lambda}{11.6}, \text{ error is within 5\%}$$

## **APPENDIX B: FRESNEL LENS DESIGN BY ACOUSTIC TRANSMISSION LINE**

### **ABSTRACT**

We proposed an approach to construct a 2D Fresnel lenses by acoustic network. This lens is composed of an array of Helmholtz resonators. The resonance at individual resonators results in effective focusing even the plate has subwavelength thickness. The FEM simulation results presented the ultrasonic wave propagation through the lenses together with the resulting diffraction pattern.

### **INTRODUCTION**

The Fresnel lens was first proposed as viable alternatives to conventional spherical lenses for optical focusing and has been widely studied<sup>1-7</sup>. Planar focusing lens for acoustic wave was designed according to the Fresnel zone plate theory<sup>8-9</sup>. Since the lens has simple configuration; it can be fabricated with easy and inexpensive technique. However, the efficiency of Fresnel lenses reported so far is low.

In this section, we numerically investigated the planar acoustic Fresnel lens composed of a 1D array of Helmholtz resonators using FE method. The Helmholtz resonators are filled with different medium, dividing plate into 29 Fresnel zones. The acoustic wave fields at different frequencies are compared from the simulation results.

## FRESNEL LENSES DESIGN BY ACOUSTIC NETWORK

The spherical wavefront from a point source  $S$  as shown in Fig.B1 (a) can be divided into series annular regions called Fresnel zones<sup>10</sup>. When there is no Fresnel zone plate, the amplitude of wave field at observation point  $P$  from each zone alternates between positive and negative values. This means that the contributions from adjacent zones are out-of-phase and tend to nullify each other. If we remove either all the even or all the odd zones, we will observe a tremendous increase in irradiance at  $P$ . Fresnel zone plate is designed to pass only the odd (even) zones and obstructs the even (odd) zones. Fig.B1 (b) shows the configuration of planar 1D Fresnel lens we designed. The lens is composed of an array of Helmholtz resonators. The resonators which resonate at 50 KHz in pass even zone are filled with water. The cells in odd zone are filled with air to induce large impedance mismatch, resulting large reflection to obstruct vibration. In Fig.B1 (a), the edge of the  $m$ th zone ( $R_m$  from center) is marked by point  $A_m$ , distance from the plate to source  $\rho_0$  and distance from the plate to the image  $r_0$ . Since the wave travels through  $m$ th zone must be out of phase with the center zone by  $m\lambda/2$ , so

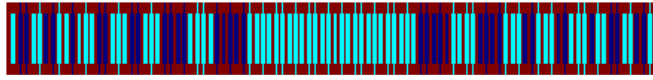
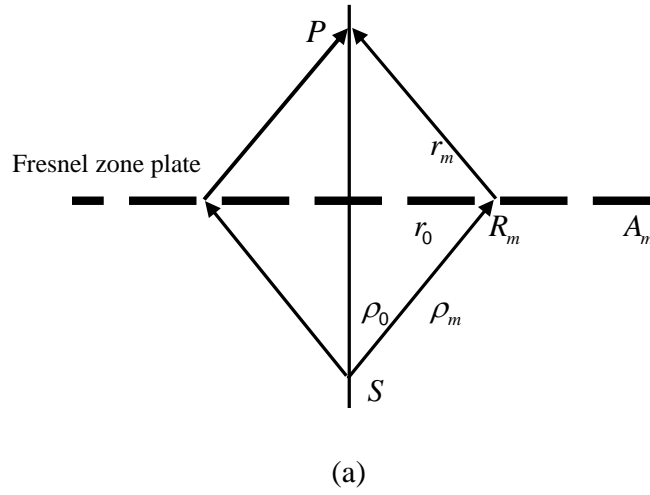
$$(\rho_m + r_m) - (\rho_0 + r_0) = m\lambda/2 \quad (1)$$

Where  $\rho_m = (R_m^2 + \rho_0^2)^{1/2}$  and  $r_m = (R_m^2 + r_0^2)^{1/2}$  expand both equations, since  $R_m$  is comparatively small, we get

$$\rho_m = \rho_0 + \frac{R_m^2}{2\rho_0} \quad r_m = r_0 + \frac{R_m^2}{2r_0} \quad (2)$$

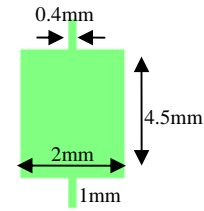
Substitute (2) into (1), we obtain

$$\frac{1}{\rho_0} + \frac{1}{r_0} = \frac{m\lambda}{R_m^2} \quad (3)$$



	Aluminum	$\rho_1=2700 \text{ kg/m}^3$	$v_1=6260$
	Water	$\rho_2=1000 \text{ kg/m}^3$	$v_2=1483$
	Air	$\rho_3=1.21 \text{ kg/m}^3$	$v_3=344$

(b)



(c)

**Figure B1** (a) Schematic diagram of zone plate focusing (b) Configuration of acoustic Fresnel lens (c) Designed unit Helmholtz resonators

$\rho_0$  and  $r_0$  are interrelated by the same equation as for lens  $\frac{1}{\rho_0} + \frac{1}{r_0} = \frac{1}{f}$ , where focal length  $f$  is defined as  $f = \frac{R_m^2}{m\lambda}$  when  $\rho_0 \rightarrow \infty$  the source of light is put so far away from the plate that the incoming wave can be regarded as a plane wave .

$$R_m^2 = mr_0\lambda \quad (4)$$

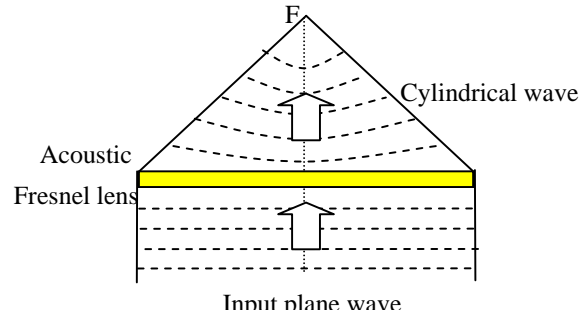


**Figure B2** Computational model

## RESULTS AND DISCUSSION

Figure B2 shows the simulation model. FEM (finite-element method) is employed to study the focusing of the designed Fresnel plate lens. A collimated acoustic wave is incident on the plate, which is put inside water medium. The focus point  $F$  is expected on the other side of the plate. When there is no focusing plate, the pressure field in  $F$  is the sum of each half wavelength zone

$$P = P_1 + P_2 + \dots + P_{29}$$

and each term is approximately equal. Since each term has  $\pi$  phase difference, the pressure at  $F$  would be  $\frac{P_1}{2}$ , whereas with the zone plate in place,  $P \approx 7P_1$ . The intensity of acoustic field is increased by a factor of 196. Since the resonance effect in pass zone, we expect the proposed plate yield a very high efficiency.

The focus is assumed at  $r_0 = 100\text{mm}$ . We calculate the position of each zone by equation  $R_m^2 = mr_0\lambda$ , setting  $\lambda = 30\text{mm}$  (wavelength at 50 KHz in water). The dependence of focus position on frequency is studied. A series simulations have been studied at 40, 50, 60 and 70 KHz. Figure 3 (a)-(d) presented the pressure field distribution above the plate, which is 550mm width along

horizontal axis. The  $y$  axis is the distance from the plate. We observe the focuses above the plate along the central axis. Plane wave pattern is also presented resulting from the penetration of acoustic wave through this thin plate. The focus position is found at  $y = 75, 115, 150, 175 \text{ mm}, x = 0 \text{ mm}$  at 40, 50, 60 and 70 KHz respectively. The pressure intensity cross the focus as function of  $x$  is plotted in Fig 3 (f) - (i). A conventional Fresnel zone plate is also studied as comparison. There is an array of through holes in the aluminum plate, constituting the pass zones. The acoustic wave field through the zone plate put inside water is shown in Fig 3 (e). Since the thickness of the metal plate is only  $0.23\lambda$  same as the Fresnel lens based on acoustic network, the plane wave penetration through the plate is dominate. The amplitude of the focus is comparable with the side lobe as shown in Fig 3 (j). More than 50dB pressure level difference is found between pass and obstruct zones in Fresnel zone plate based on acoustic network in Fig3 (k) at 50 KHz.

The focal length of the lens changes with source frequency  $r_0 = \frac{R_m^2}{m\lambda_0} = \eta f$ . The design set  $r_0 = 100 \text{ mm}$  and  $\lambda = 30 \text{ mm}$ , so  $\eta = 3e3 \text{ m}^2$ . Figure 4 compared the analytical prediction of focus length with numerical results. As shown in the figure, focal length increases with frequency. As frequency increases, there are more numerical errors from the FEM model. For the same mesh model, the accuracy will decrease with increasing frequency. As frequency was shifted away from resonance frequency 50 KHz for the pass zone, the efficiency of the lens decayed.

## CONCLUSION

In this paper, planar Fresnel lens is built by an array of designed Helmholtz resonators. The Helmholtz resonators are filled with different medium, forming pass and obstruct zones. The

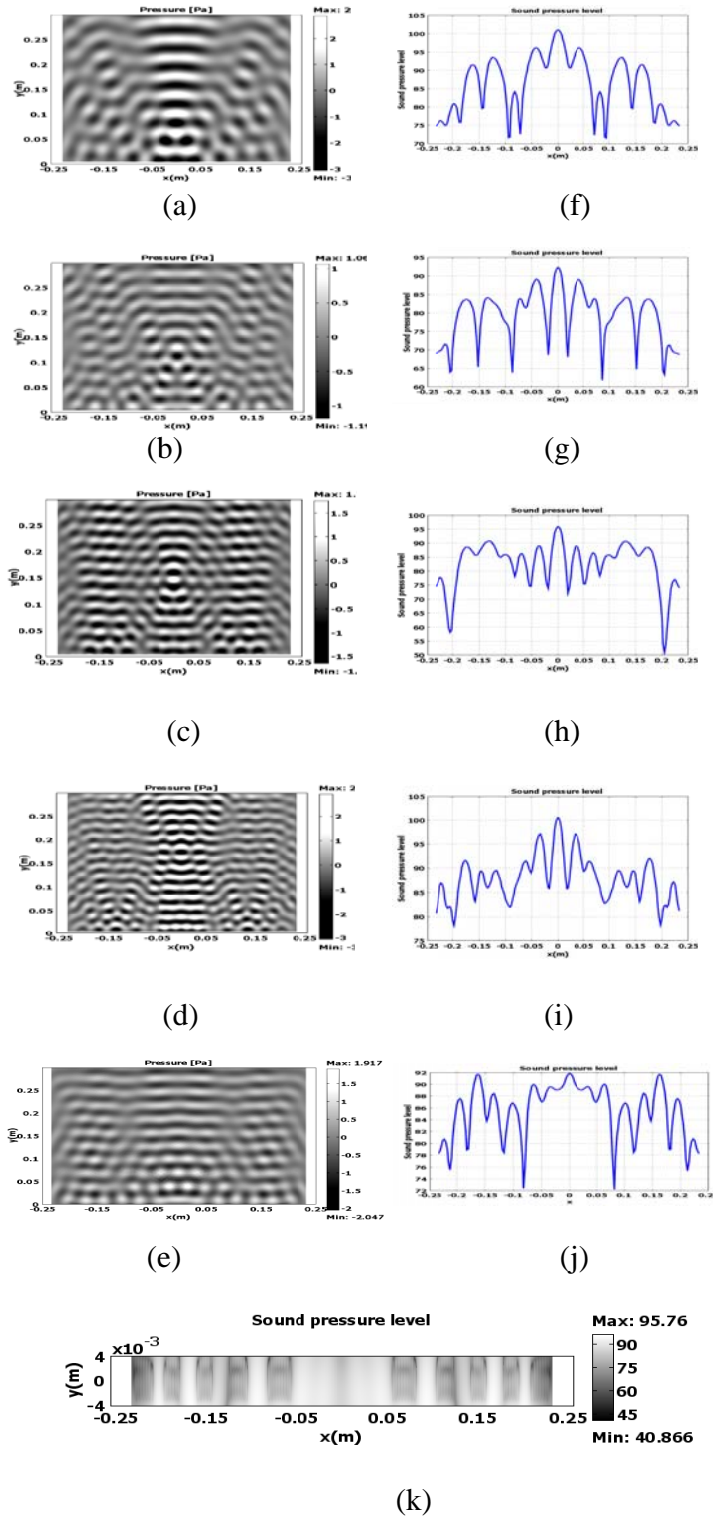


**Figure B3** A cross section of pressure field distribution through the Fresnel lens based on acoustic network at (a) 40 KHz (b) 50 KHz (c) 60 KHz (d) 70 KHz and through a metal Fresnel

lens at (e) 50 KHz. The line plot of pressure level cross focus at (e)  $y = 75\text{mm}$  at 40 KHz (f)  $y = 115\text{mm}$  at 50 KHz (g)  $y = 150\text{mm}$  at 60 KHz (h)  $y = 175\text{mm}$  at 70 KHz for Fresnel network lens and (j)  $y = 115\text{mm}$  at 50 KHz for the metal Fresnel lens (k) the sound pressure level in Fresnel network lens composed of an array of resonators at 50 kHz

simulation results demonstrated that a plane pressure wave is focused through the planar structure. Compared with conventional Fresnel lens with the same thickness, the focus effect is more efficient through those based on acoustic network design .The focal length of the lens can be tuned at different frequency as well.

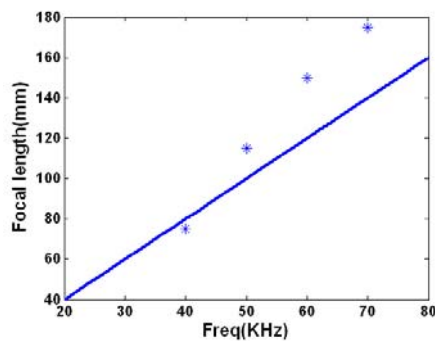


**Figure B4** Focal length as a function of frequency

## References

1. G. Hatakoshi and S. Tanaka, “Grating lenses for integrated optics”, *Opt. Lett.* **2**, 142-144 (1978).
2. T. Suhara, K. Kobayashi, H. Nishihara, and J. Koyama, “Graded-index Fresnel lenses for integrated optics”, *Applied Optics* **21**, 1966-1971(1982).

3. K. Rastani, A. Marrakchi, S. F. Habiby, W. M. Hubbard, H. Gilchrist, and R. E. Nahory, “Binary phase Fresnel lenses for generation of two-dimensional beam arrays”, *Appl. Opt.* **30**, 1347-1354 (1991).
4. J. S. Patel and K. Rastani, “Electrically controlled polarization-independent liquid-crystal Fresnel lens arrays”, *Opt. Lett.* **16**, 532-534(1991).
5. H. Ren, Y.H. Fan, and S.T. Wu., “Tunable Fresnel lens using nanoscale polymer-dispersed liquid crystals”, *Appl. Phys. Lett.* **83**, 1515-1517(2003).
6. Y.H. Fan, H. Ren, and S.T. Wu, “Electrically switchable Fresnel lens using a polymer-separated composite film”, *Opt. Express* **13**, 4141-4147(2005).
7. L.C. Lin, H.C. Jau, T.H. Lin, and A.Y.Fuh, “Highly efficient and polarization-independent Fresnel lens based on dye-doped liquid crystal”, *Opt. Express* **15**, 2900-2906(2007)
8. K Yamada, T Sugiyama and H Shimuzi, “Theoretical Considerations on Acoustic Field Formed by Fresnel Zone Type Focusing Radiator,” *Jpn J Appl Phys* **26**, 180-182(1987).
9. Hadimioglu, B. et al., “High-efficiency Fresnel acoustic lenses”, *Ultrasonics Symposium* **1**, 579 – 582(1993).
10. Eugene Hecht , “Optics”, Addison Wesley 2002
11. Shin Chuen Chan *et al.*, “Finite element analysis of multilevel acoustic Fresnel lenses”, *Ultrasonics, Ferroelectrics and Frequency Control, IEEE Transactions* **43**, 670 – 677(1996).

## **APPENDIX C: NEGATIVE INDEX LENS BASED ON METAL-INSULATOR-METAL (MIM) WAVEGUIDES**

In this appendix, we calculated the dispersion curves of several different waveguide designs. Negative refraction at visible frequencies is proved experimentally in designed metal-insulator-metal (MIM) waveguides recently<sup>1</sup>. From our simulation, negative refractive index is found in Ag-Si<sub>3</sub>N<sub>4</sub>-Ag planar waveguides with 50nm dielectric core. As the dielectric core thickness is increased to 200nm, a matched mode is found to across the negative slope branch of the waveguide with 50nm core. In waveguide Ag-Si<sub>3</sub>N<sub>4</sub>-PMMA-Ag with 50nm Si<sub>3</sub>N<sub>4</sub> and 150nm PMMA, there are also two mode branch which cross the negative slope of the Ag-Si<sub>3</sub>N<sub>4</sub>-Ag planar waveguides with 50nm dielectric core. Electromagnetic field distributions of two cascaded waveguides are simulated by 3D FDTD method. The center positioned waveguide with 50nm Si<sub>3</sub>N<sub>4</sub> core is made of crescent shape to investigate the focus effect of the MIM waveguides. Several samples are fabricated by depositing 100nm silver with curved shape on 50nm Si<sub>3</sub>N<sub>4</sub> membrane.

### ***MIM simulation***

We investigate the dispersion curve property of several planar waveguides. Transfer matrix approach was used to simulate the transmission behavior of a multilayer stack of films (Figure 1). The approach is based on matrix formulation of field amplitudes in terms of Fresnel coefficients. A recurrence formula relating field amplitudes in successive layers is expressed as:

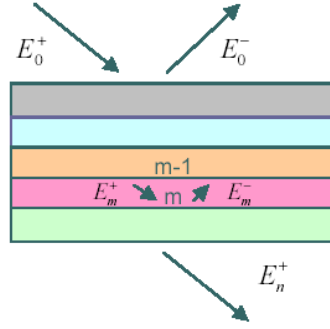


**Figure C1** Transfer matrix approach for an optical system with multilayer stack of films.

$$\begin{pmatrix} E_{m-1}^+ \\ E_{m-1}^- \end{pmatrix} = \frac{1}{t_m} \begin{pmatrix} \exp(-i\gamma_m) & r_m \exp(-i\gamma_m) \\ r_m \exp(i\gamma_m) & \exp(i\gamma_m) \end{pmatrix} \begin{pmatrix} E_m^+ \\ E_m^- \end{pmatrix} \quad (1)$$

where  $E_m^+$   $E_m^-$  denote the field amplitude of the forward and backward propagating wave in the  $m^{\text{th}}$  layer respectively (Note that there is no backward propagating wave in the  $n^{\text{th}}$  layer, i.e.  $E_n^- = 0$ ).  $t_m, r_m$  are Fresnel transmission and reflection coefficients at the interface between  $(m-1)^{\text{th}}$  and  $m^{\text{th}}$  layer, respectively.  $\gamma_{m=d_{m-1}k_{m-1}}$  is the phase factor,  $d_m$  and  $k_m$  are thickness and wave vector of  $m^{\text{th}}$  layer respectively.

From the recurrence relation, an expression for transmission (T) and reflection (R) can be computed as:

$$\begin{pmatrix} E_0^+ \\ E_0^- \end{pmatrix} = \begin{pmatrix} a & b \\ c & d \end{pmatrix} \begin{pmatrix} E_n^+ \\ 0 \end{pmatrix} \quad (2)$$

$$T = \frac{E_n^+}{E_0^+} = \frac{1}{a} \quad (3)$$

$$R = \frac{E_0^-}{E_0^+} = \frac{c}{a} \quad (4)$$

where  $\begin{pmatrix} a & b \\ c & d \end{pmatrix} = (C_1)(C_2)\dots(C_n)$ ; and  $(C_m) = \frac{1}{t_m} \begin{pmatrix} \exp(-i\gamma_m) & r_m \exp(-i\gamma_m) \\ r_m \exp(i\gamma_m) & \exp(i\gamma_m) \end{pmatrix}$

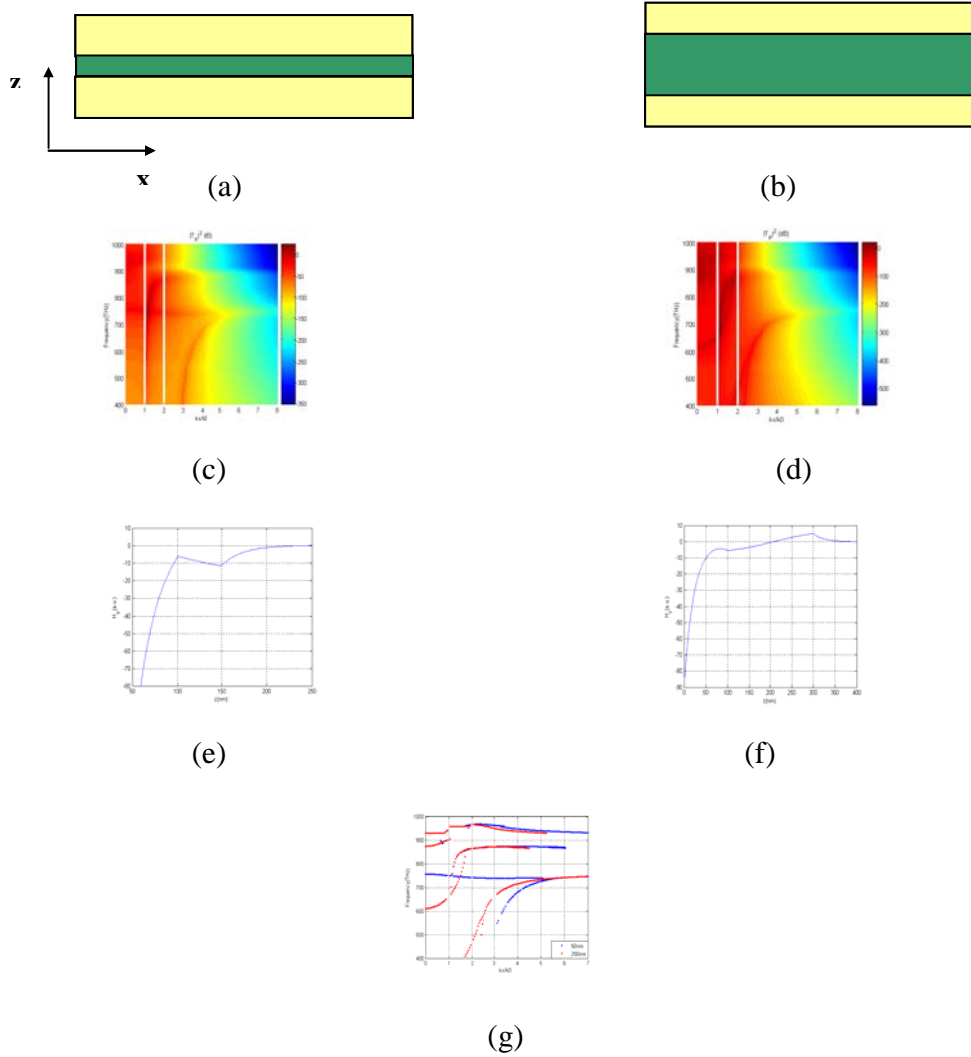


**Figure C2** (a) An Ag-Si<sub>3</sub>N<sub>4</sub>-Ag with 50nm dielectric core and (b) an Ag-Si<sub>3</sub>N<sub>4</sub>-Ag with 200nm dielectric core .Computed isotherm contour of transmission  $|T_p|^2$  of (c) the waveguide with 50nm dielectric core and (d) of the waveguide with 200nm dielectric core. Hy field distribution along z axis of (e) the waveguide with 50nm dielectric core and (f) of the waveguide with 200nm dielectric core. (g) Dispersion curve of Ag-Si<sub>3</sub>N<sub>4</sub>-Ag waveguide with 50nm and 200nm dielectric core.

The calculated transmission of two Ag-Si<sub>3</sub>N<sub>4</sub>-Ag waveguides with 50nm and 200nm dielectric core is shown in Fig.C2 (c) and (d). The transmission of P-polarized light is investigated. Several bright lines are observed in Fig.C2(c) and (d), which corresponds to propagation mode of the waveguides. The Hy field distribution normal to the layers are shown in Fig. C2 (e) and 2(f) for 50nm and 200 nm dielectric core respectively. Two discontinuity points are observed on both curves in the positions of the two boundaries of Si<sub>3</sub>N<sub>4</sub> with Silver. In Fig.C2(g), dispersion curves of two Ag-Si<sub>3</sub>N<sub>4</sub>-Ag waveguides are presented. From frequency 700THz to 700THz, the blue dispersion curve of Ag-Si<sub>3</sub>N<sub>4</sub>-Ag waveguides with 50nm dielectric core exhibits a negative slope. There is one matched mode from the cross of the dispersion curve of the two waveguides at 750 KHz and  $k_x / k_0 = 1.5$ .

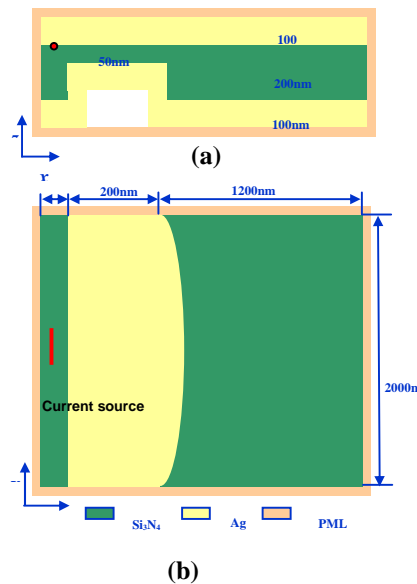


**Figure C3** (a) cross section and (b) corresponding plane view of the cascaded waveguides

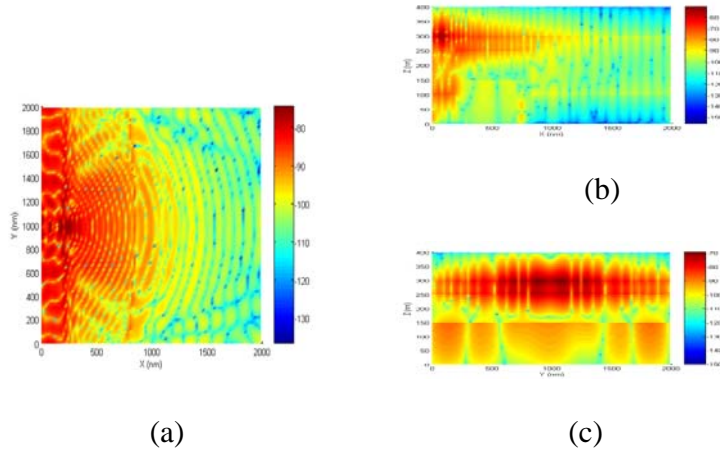


**Figure C4**  $E_z$  Field distribution in the cascaded waveguides on (a)  $xy$ -plane at  $z=233\text{nm}$ ; (b)  $xz$ -plane at  $y=1000\text{nm}$  (c)  $yz$ -plane at  $x=600\text{nm}$

Fig.C3 shows the cross section and top view of the waveguides. An Ag-Si<sub>3</sub>N<sub>4</sub>-Ag waveguides with 50nm dielectric core is positioned between two Ag-Si<sub>3</sub>N<sub>4</sub>-Ag waveguides with 200nm dielectric core. The center waveguide was designed with curved boundary shape on left side.

Three-dimensional FDTD method is employed to calculate the wave propagation through the cascaded waveguides. The  $E_z$  Field distributions in the waveguides in fig 3 are presented in figure 4. A one-fifth wavelength long current source  $J_z$  at  $\lambda=400\text{nm}$  is applied in the top boundary of the dielectric and Ag. In Fig.C4 (a), the  $E_z$  Field distribution on  $xy$ -plane at  $z=233\text{nm}$  is shown. The  $E_z$  field is propagating through the waveguide with quite a lot loss around 20dB after through the center 50nm dielectric core. Fig.C4 (b) shows  $E_z$  Field on the  $xz$ -plane at  $y=1000\text{nm}$ . The dark red point shows the source position. The field decays in Si<sub>3</sub>N<sub>4</sub>

along the propagation path. Also  $E_z$  decays vertically in Silver layer. The  $E_z$  field over  $yz$ -plane at  $x=600\text{nm}$  is shown as in Fig.C4 (c). The cross section is cut through the part with 50nm dielectric core, which is clearly observed from 250nm to 300nm in the figure. The field decays in the bottom and top 100nm silver part. Around 95dB  $E_z$  field is presented outside the waveguide from 0 to 150 nm where there is air. It suggested that 100nm silver cladding might not be enough to ensure complete opacity.

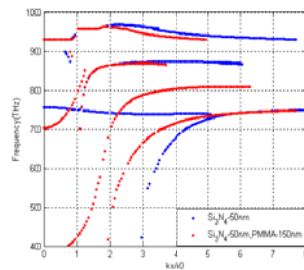


**Figure C5** Dispersion curve of Ag-Si<sub>3</sub>N<sub>4</sub>-Ag with 50nm dielectric core (blue dots) and Ag-Si<sub>3</sub>N<sub>4</sub>-PMMA-Ag (red dots) with 50nm Si<sub>3</sub>N<sub>4</sub> and 150nm PMMA

Instead of 200nm Si<sub>3</sub>N<sub>4</sub>, two layers of 50 nm Si<sub>3</sub>N<sub>4</sub> and 150nm PMMA are used as core for the positive waveguide part. This design offers an easy way for fabrication and flexibility for the thickness of the dielectric part. Dispersion curves of Ag-Si<sub>3</sub>N<sub>4</sub>-PMMA-Ag with 50nm Si<sub>3</sub>N<sub>4</sub> and 150nm PMMA is shown in figure5 in red dots. The blue dots presented the dispersion curve of Ag-Si<sub>3</sub>N<sub>4</sub>-Ag with 50nm dielectric core. There are two cross points in figure showing there are two possible matched modes in these two waveguides from 700THz-800THz.

Fig.C6 shows the cross section and top view of the waveguides. An Ag-Si<sub>3</sub>N<sub>4</sub>-Ag waveguides with 50nm dielectric core is positioned between two Ag-Si<sub>3</sub>N<sub>4</sub>-PMMA-Ag

waveguides with 50nm Si<sub>3</sub>N<sub>4</sub> and 150nm PMMA as core. The center waveguide was designed with curved boundary shape on left side.

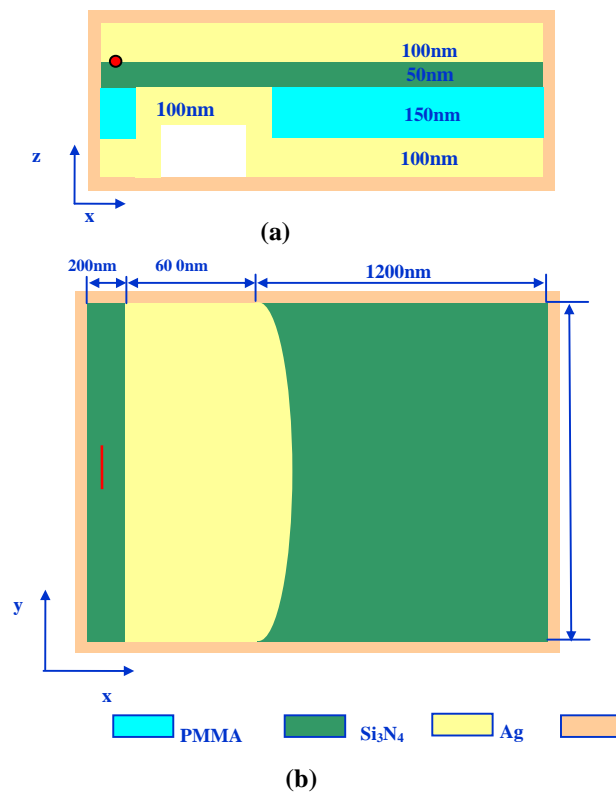


**Figure C6** (a) cross section and (b) corresponding plane view of the cascaded waveguides

The  $E_z$  Field distributions in the waveguides are presented in Fig.C7. A one-fifth wavelength long current source  $J_z$  at  $\lambda = 400nm$  is applied in the top boundary of the dielectric and Ag. In Fig.C7 (a), the  $E_z$  Field distribution on  $xy$ -plane at  $z=280nm$  is shown. Compared with fig 4(a), less boundary feature is shown on the left side of the Ag-Si<sub>3</sub>N<sub>4</sub>-Ag to Ag-Si<sub>3</sub>N<sub>4</sub>-PMMA-Ag in fig7 (a). Fig.C7 (b) shows  $E_z$  Field on the  $xz$ -plane at  $y=1000nm$ . More leakage of the field in air

from  $x=300\text{nm}$  to  $x=800\text{nm}$  is presented. The  $E_z$  field over  $yz$ -plane at  $x=600\text{nm}$  is shown as in Fig.C7 (c). Around 95dB  $E_z$  field is presented below the waveguide in air. It proved again that 100nm silver cladding might not be enough to ensure complete opacity.

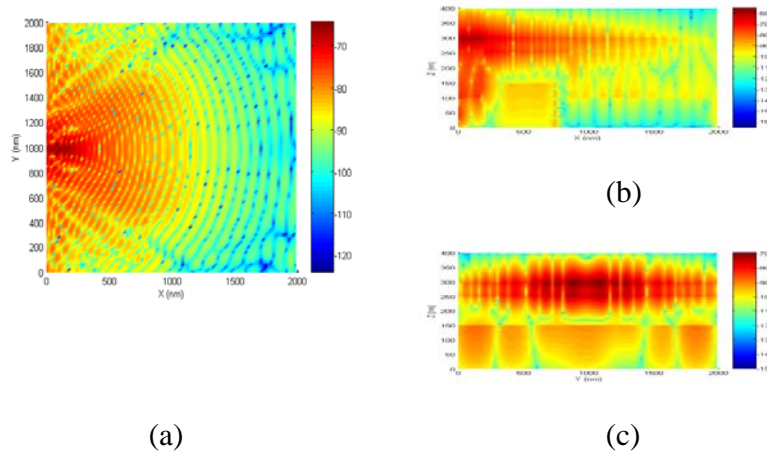


**Figure C7**  $E_z$  Field distribution in the cascaded waveguides on (a)  $xy$ -plane at  $z=280\text{nm}$ ;  
(b)  $xz$ -plane at  $y=1000\text{nm}$  (c)  $yz$ -plane at  $x=600\text{nm}$

### 3D FDTD model

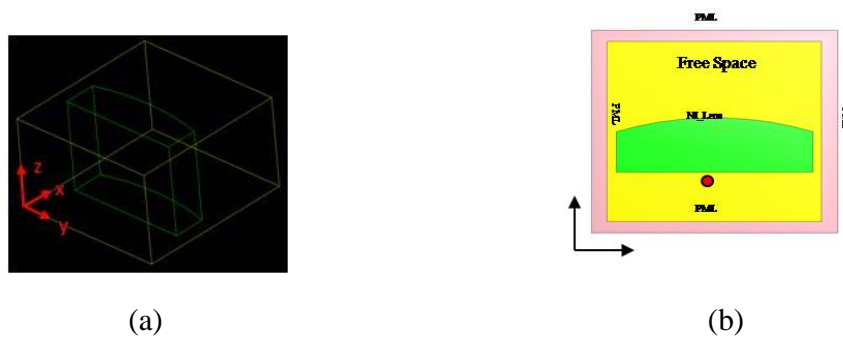


**Figure C8** (a) Geometry for the 3D-FDTD model (b) top view<sup>Current</sup> of the 3D model

Three-dimensional FDTD model is employed to simulate the electromagnetic field propagating through negative index lens. The computational domain is  $220 \times 220 \times 100$  grid points, in the  $x$ ,  $y$ , and  $z$  direction, respectively. Figure 1(a) shows the model, a negative index (NI) lens is placed in the middle of the model. We used Drude model to set  $\varepsilon$  and  $\mu$  as following expression:

$$\varepsilon = \varepsilon_0 \left(1 - \frac{\omega_p^2}{\omega^2}\right) \quad \mu = \mu_0 \left(1 - \frac{\omega_p^2}{\omega^2}\right)$$

For the PML (perfect matched layer), we used 15 layers with  $\sigma_{\max} = 10$ . The analytical expression

for  $\sigma$  is given by  $\sigma_n = \sigma_{\max} \left(\frac{n}{L}\right)^2$

where  $n$  is either  $x$ ,  $y$ , or  $z$  and  $L$  is the PML's thickness.

A dipole current source was located at (38, 110, [38 62]). The input signal is given by

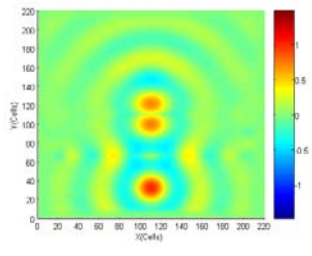
$$f(t) = \begin{cases} g_{on}(t) \sin(\omega_0 t) & \text{for } 0 \leq t < mT_p \\ \sin(\omega_0 t) & \text{for } mT_p \leq t < (m+n)T_p \\ g_{off}(t) \sin(\omega_0 t) & \text{for } (m+n)T_p \leq t < (m+n+m)T_p \\ 0 & \text{for } (m+n+m)T_p < t \end{cases}$$

where  $T_p = 1/f_0$  is the period of one single cycle with  $f_0 = 30GHz$  in the simulation. The

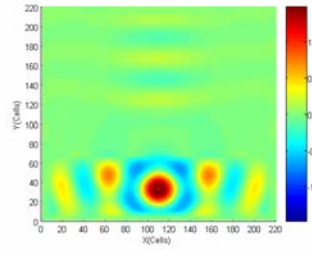
three-derivative smooth window functions are given by  $g_{on}(t) = 10x_{on}^3 - 15x_{on}^4 + 6x_{on}^5$

$$g_{off}(t) = 1 - [10x_{off}^3 - 15x_{off}^4 + 6x_{off}^5] \text{ with } x_{on} = 1 - (mT_p - t)/mT_p, x_{off} = [1 - (m+n)]/mT_p$$

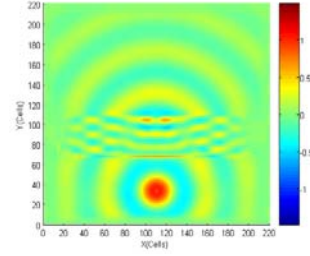
Fig. C (9-11) showed the  $\mathbf{E}_z$  field distribution of the model for three different index lens with  $n=-1, -3$  and  $-0.23$  respectively, In Fig. C10 (a), two focus points are observed in the  $xy$  plane because of index match between the lens and free space. Collimation feature is observed in fig3 (a) for lens  $n=-0.23$  while divergence of the field is shown in Fig.C11 (a). Fig.C9 (b), Fig.C10 (b) and Fig.C11 (b) presented the field along the boundary of the lens in  $yz$ -plane. From all the three figures, propagation modes are observed parallel to  $y$  direction. The depth of the lens



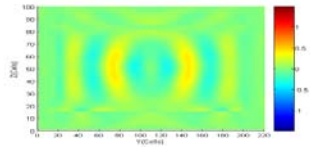
(a)



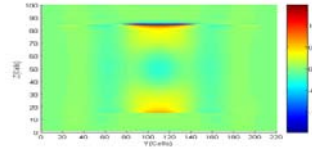
(a)



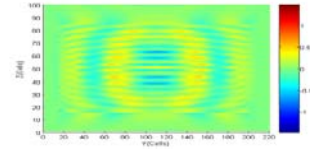
(a)



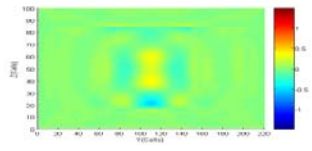
(b)



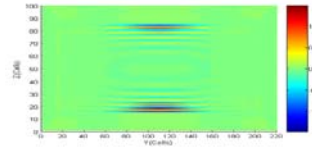
(b)



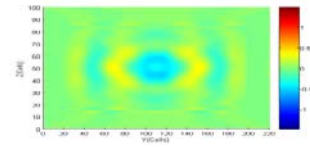
(b)



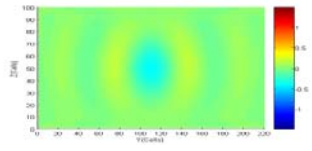
(c)



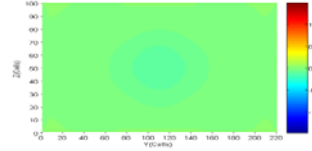
(c)



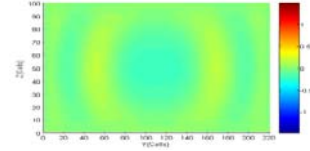
(c)



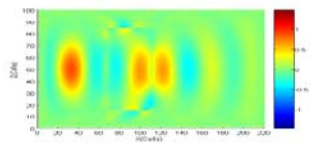
(d)



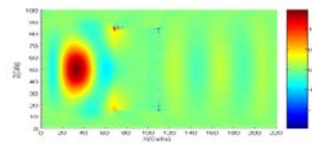
(d)



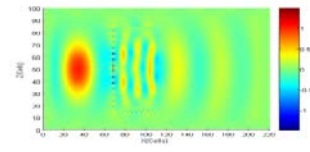
(d)



(e)



(e)



(e)

**Figure C9**  $E_z$  Field distribution for  $n=1$  in the (a)  $xy$ -plane at  $z=50$ ; (b)  $yz$ -plane at  $x=68$  (c) $x=110$  ;(d) $x=150$  ;(e) $xz$ -plane at  $y=115$

**Figure C10**  $E_z$  Field distribution for  $n=-0.23$  in the (a)  $xy$ -plane at  $z=50$ ; (b)  $yz$ -plane at  $x=68$  (c) $x=110$  ;(d) $x=150$  ;(e) $xz$ -plane at  $y=115$

**Figure C11**  $E_z$  Field distribution for  $n=-3$  in the (a)  $xy$ -plane at  $z=50$ ; (b)  $yz$ -plane at  $x=68$  (c) $x=110$  ;(d) $x=150$  ;(e) $xz$ -plane at  $y=115$

along  $z$  direction is two wavelengths for  $f_0 = 30GHz$  in vacuum. In Fig. C11 (b), strong interference is observed. The interference caused standing wave mode since depth of lens along  $z$  is six wavelengths.

The fields along the other boundary of the lens in  $yz$ -plane are shown in Fig.C9 (c), Fig.C10 (c) and Fig.C11(c). The focus is observed for index matched lens  $n=-1$  in Fig.C9(c). Propagation mode are observed in Fig.C9 (c) and Fig.C11 (c) while field is restricted to center area resulted from collimation in Fig.C10 (c).The fields in the free space in  $yz$ -plane after through the lens are shown in Fig.C9 (d), Fig.C10(d) and Fig.C11(d). The field is more divergent in fig 4(d) compared with the one in Fig.C9 (d). In Fig.C10 (d), no propagation parallel to  $y$  direction is presented.The fields in  $xz$ -plane are shown in Fig.C (9-11)(e). Two focuses are observed in Fig. C10 (e).Plane wave phase front is observed in Fig.C10 (e) and convergent wave is presented in Fig.C10 (e).

*Simulation Study of the waveguide MDM with effective negative index*

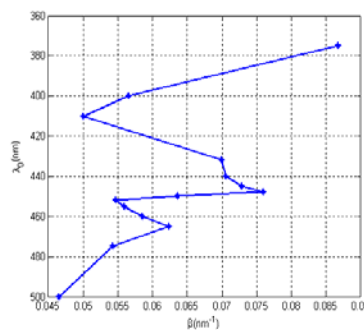


**Figure C12** Calculated dispersion curves for an Ag-Si<sub>3</sub>N<sub>4</sub>-Ag waveguides with 50nm thickness dielectric core

Three-dimensional FDTD method is employed to calculate the dispersion curve for an Ag-Si<sub>3</sub>N<sub>4</sub>-Ag waveguides with 50nm dielectric core. A point source excited the electromagnetic field inside the waveguide. The wavevector is calculated by spatial Fourier transfer. The dispersion curve exhibits a negative slope over 410-448nm and hence negative index behavior is expected in this frequency domain. In range 455-465nm, the curve also shows negative slope. As the electrical field distribution is Bessel function, the period continuous changing along the propagation direction. The finite size of calculation domain causes reflection from the boundary even PML (perfect matched layer) is used.

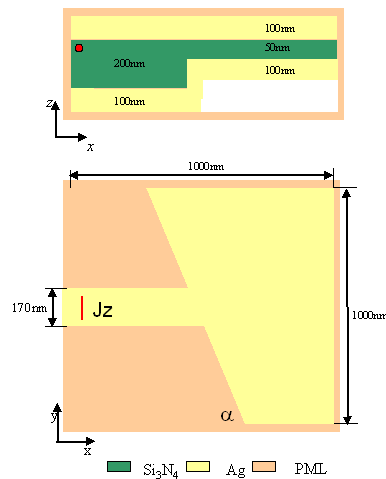


**Figure C13** (a) cross section and (b) top view of the simulated waveguides

Wave propagation through a cascaded waveguides was simulated. Fig.C13 shows the cross section and top view of the waveguides. An Ag-Si<sub>3</sub>N<sub>4</sub>-Ag waveguides with 200nm dielectric core is connected with an Ag-Si<sub>3</sub>N<sub>4</sub>-Ag waveguides with 50nm dielectric core. The waveguide with 200 nm Si<sub>3</sub>N<sub>4</sub> is a 170nm wide slot shape. The interface of two waveguides makes an angle  $\alpha = 79.3^\circ$  with horizontal direction.

The simulation results are presented in Fig.C14. A current source  $J_z$  at 428nm is induced parallel to y direction at  $z=275\text{nm}$ . This wavelength falls in the negative-index regions for the 50nm dielectric core waveguide according to dispersion curve.  $E_z$  field at  $z=275\text{nm}$  is shown in fig3. We observed negative refraction with angle  $\varphi_2 = 12.5^\circ$  when the beam propagates through the interface. The incident angle  $\varphi_1$  is  $10.7^\circ$ . The effective index for 50nm  $\text{Si}_3\text{N}_4$  waveguide is -4 at 428nm from calculation. Hence the effective index for 200nm core waveguide is around 4.66 by Snell's law.

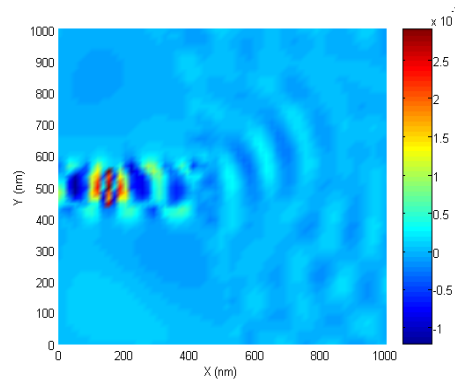


**Figure C14**  $E_z$  Field distribution in the cascaded waveguides on  $xy$ -plane at  $z=275\text{nm}$

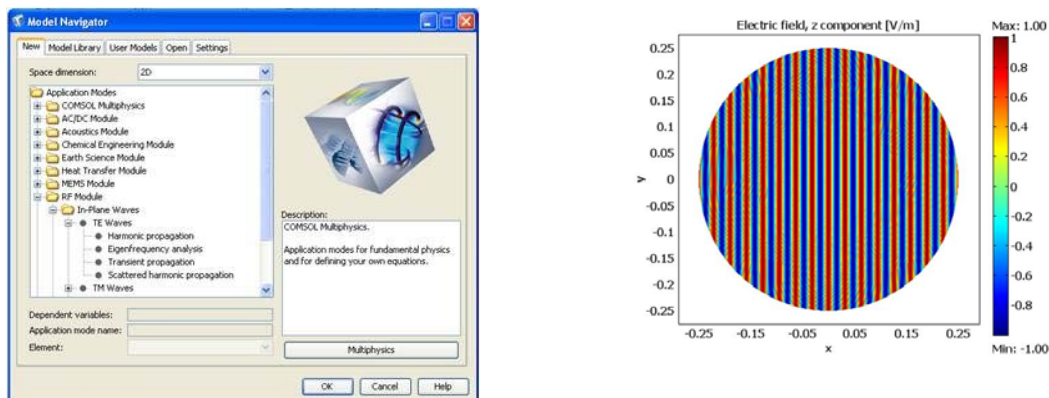
## References

1. H.J.Lezec, J.A.Dionne, H.A.Atwater, Negative refraction at visible frequencies, *Science*, 316,430(2007)

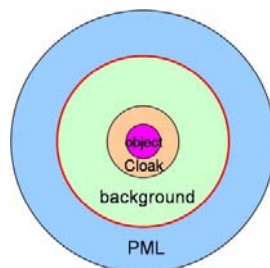
## APPENDIX D: SCATTERING FIELDS FROM THE CLOAK

### *Scattering harmonic propagation*

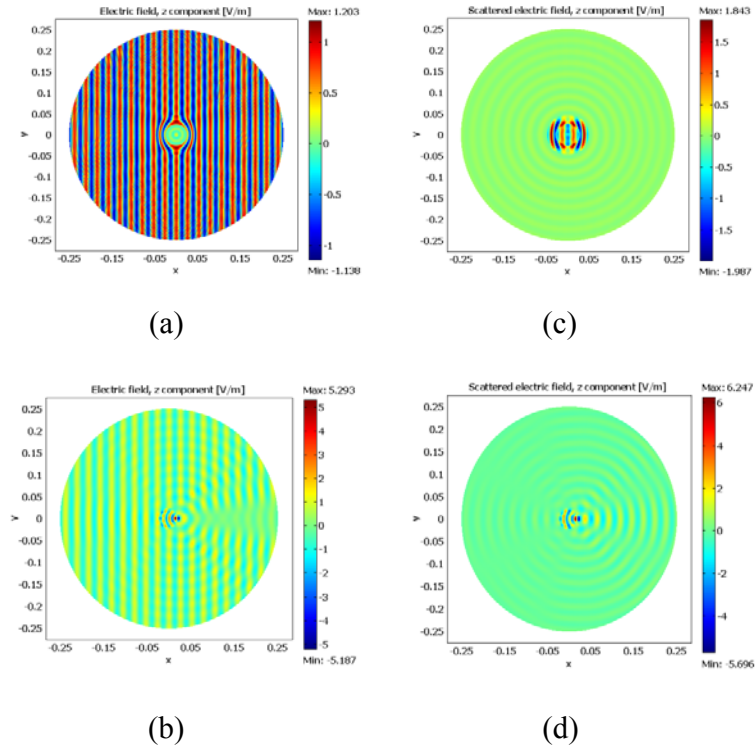
The scattering from the designed cloak is studied using FEM in this appendix. The “Scattered harmonic propagation” mode in COMSOL is selected for the following simulation. The calculation domain is presented in Figure D2. A plane wave is incident on a hidden object ( $1.0\lambda$  in diameter) surrounded by a cloaking shell of thickness  $1.0\lambda$ . A perfect matched layer (PML) is put around the cloaked object to reduce reflection.



**Figure D1** (a) Picture of model navigator in COMSOL (b) the plot of the incident wave field



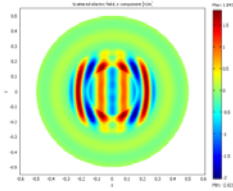
**Figure D2** Computational domain



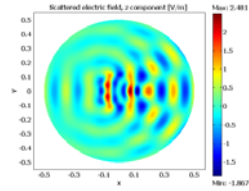
**Figure D3** Pseudo colormap of electrical field distribution due to a plane incident wave by FEM simulation. Total electrical fields (a) with cloak and (b) without cloak. Scattering field (c) with a cloak and (d) without cloak.

Fig. D3 (a) and (c) show the total electrical fields for the cases with and without cloak respectively. Nearly zero amplitude field is observed inside the cloak as expected except the singular point in center. Much less distortion is observed when the hidden object is surrounded by the cloak. The scattered fields are presented in Fig. D3 (b) and (d). Comparison shows the wave is guided around the object in the shell and merged behind the object with obvious reduction in back scattering. However, inside the cloak, there is strong scattering intensity as a result of the

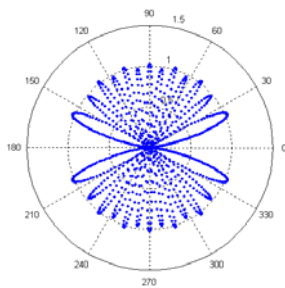
singularity in the center from the coordinate transformation.



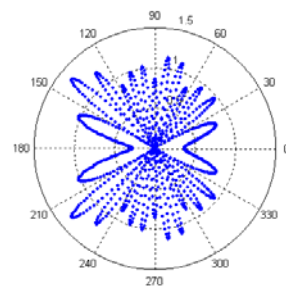
(a)



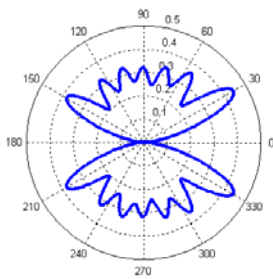
(b)



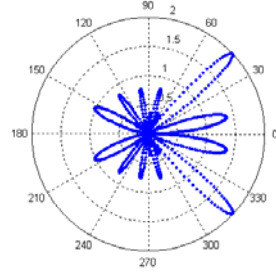
(c)



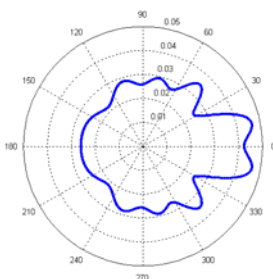
(d)



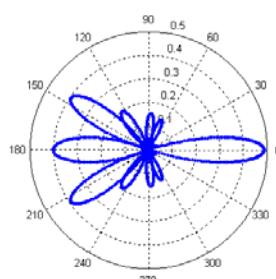
(e)



(f)



(g)



(h)

**Figure D4** Pseudo colormap of Electrical field distribution due to a plane incident wave by FEM simulation. The scattering fields (a) inside the cloak with the hidden object (b) from the bare object when there is no cloak. The line plots of the total electrical field as function of angle when there is (c) cloak (d) no cloak. The far fields (e) with cloak (f) with no cloak. The scattering fields (g) with cloak (h) with no cloak.

The scattering fields inside the cloak with the hidden object and from the bare object when there is no cloak are presented in Fig. D4 (a) and (b). The line plots of the total electrical field as function of angle for cases when there is cloak and no cloak are shown in Fig. D4 (c) and (d). The line is positioned along the boundary of the computation domain as marked in red in Fig. D2. Fig. D4 (e) and (f) are the far fields for the cases with cloak and without cloak. The scattering fields from the cloaked object and bare object are shown in Fig. 4D (g) and (h).

The line plots are compared in Fig.5D. As indicated in Fig.5D (a), the amplitudes of the near field from both cases are comparable but rather very different pattern. However, the amplitude of the far field when there is a cloak is much smaller than the case with only bare object. Compared the scattering electrical field, the scattering is significantly reduced when the hidden object is put inside the cloak.

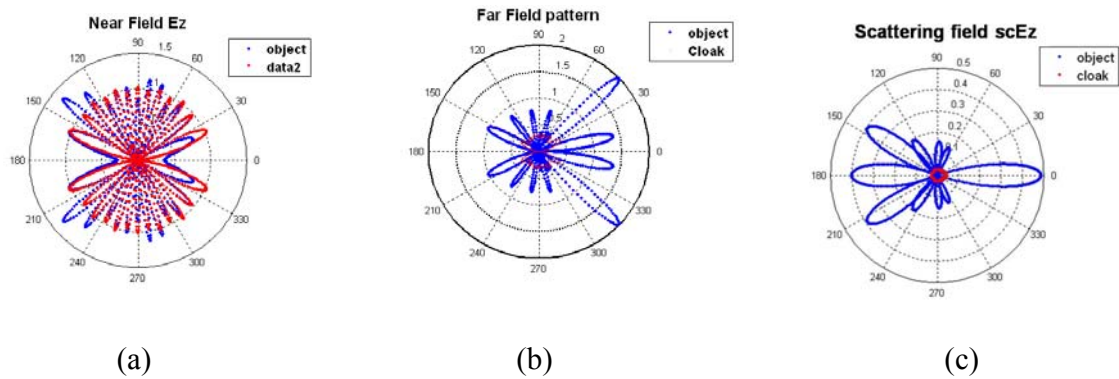


**Figure D5** The line plots of the (a) total electrical field (b) the far fields and (c) the scattering fields as functions of angle.

### Stratton-Chu formula

The far electromagnetic field can be calculated from the near field using the Stratton-Chu

formula 
$$\mathbf{E}_p = \frac{jk_0}{4\pi} \mathbf{r}_0 \times \int [\mathbf{n} \times \mathbf{E} - \eta_0 \mathbf{r}_0 \times (\mathbf{n} \times \mathbf{H})] \exp(jk_0 \mathbf{r} \cdot \mathbf{r}_0) dS$$
. Because the far field is calculated in free

space, the magnetic field at the far-field point is given by 
$$\mathbf{H}_p = \frac{\mathbf{r}_0 \times \mathbf{E}_p}{\eta_0}$$
. The Poynting vector gives the

power flow of the far field: 
$$\mathbf{r}_0 \cdot \mathbf{S} = \mathbf{r}_0 \cdot \text{Re}(\mathbf{E}_p \times \mathbf{H}_p^*) \sim |\mathbf{E}_p|^2$$
. Thus the far-field radiation pattern is given by

$|\mathbf{E}_p|^2$ . Because the Stratton-Chu formula only defines the angular distribution of the

electromagnetic field and does not depend on the distance from the near field, you can evaluate

the far field at the some boundaries you pick.

### TE wave propagation of perfect cloak (Perfect Cloak\_March08\_2010.mph)

The full-wave simulation is carried out using TE mode in software COMSOL as presented in Fig.

D6. The cloak is described by full specification of the material property.

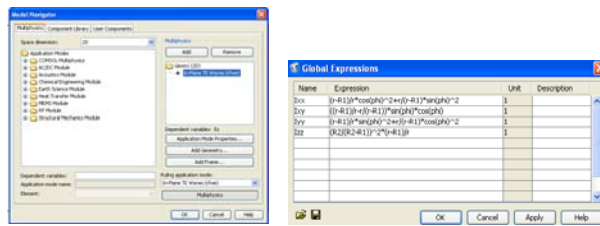


**Figure D6** Picture of model navigator in COMSOL

The calculated Electric field  $E_z$  is shown in Fig. D7 (a). As shown, the electric field is guided inside the cloak and reform to its original trajectory. The normal of the electrical field is zero inside the cloak as indicated in Fig. D7 (b) except the singularity point in center. The scattering is negligible outside the cloak according to Fig. D7(c).

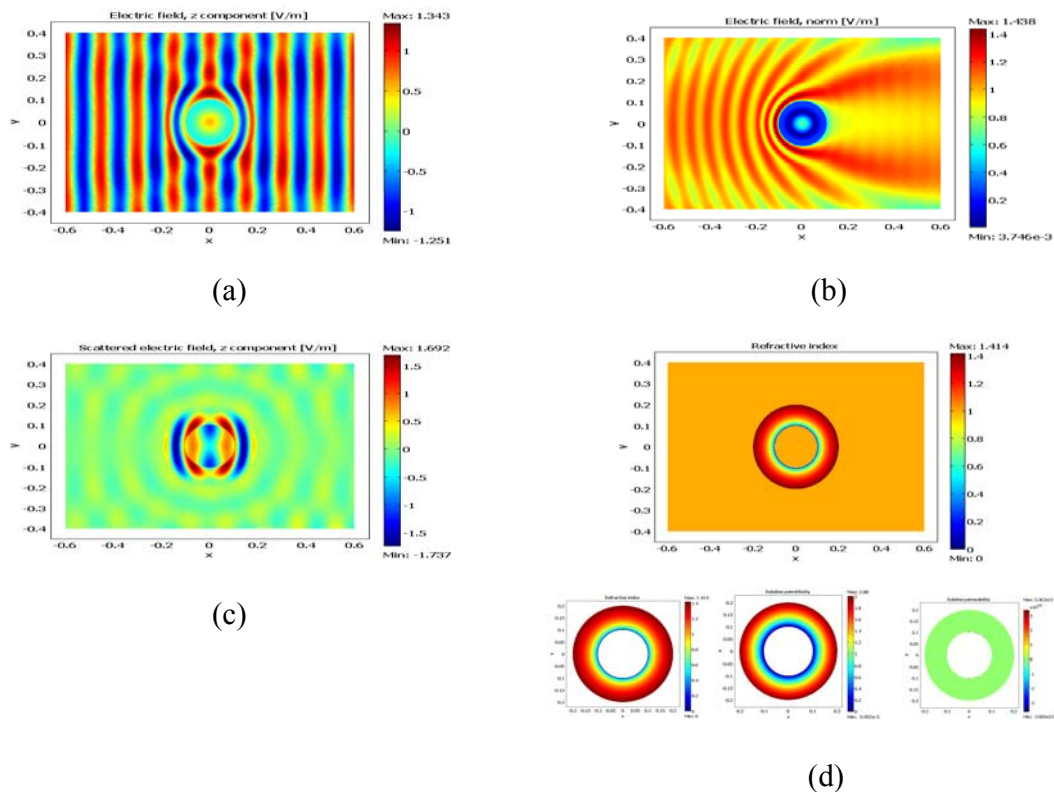


**Figure D7** TE-wave simulation of perfect cloak (a) Electric field  $E_z$  (b) Normal of Electric field  $E_z$  (c) Scattered electric field  $scE_z$  (d) Material specification of cloak

**TE wave propagation of simplified cloak (Simplified Cloak\_March08\_2010.mph)**

The full-wave simulation is carried out using TE mode in software COMSOL as presented in Fig. D6. The cloak is described by reduced specification of the material property.

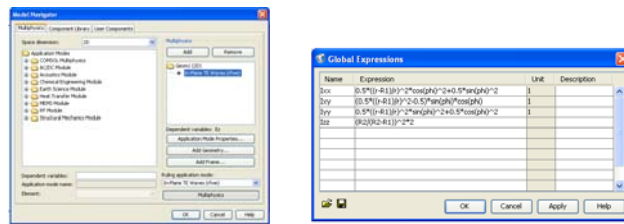


**Figure D8** Picture of model navigator in COMSOL

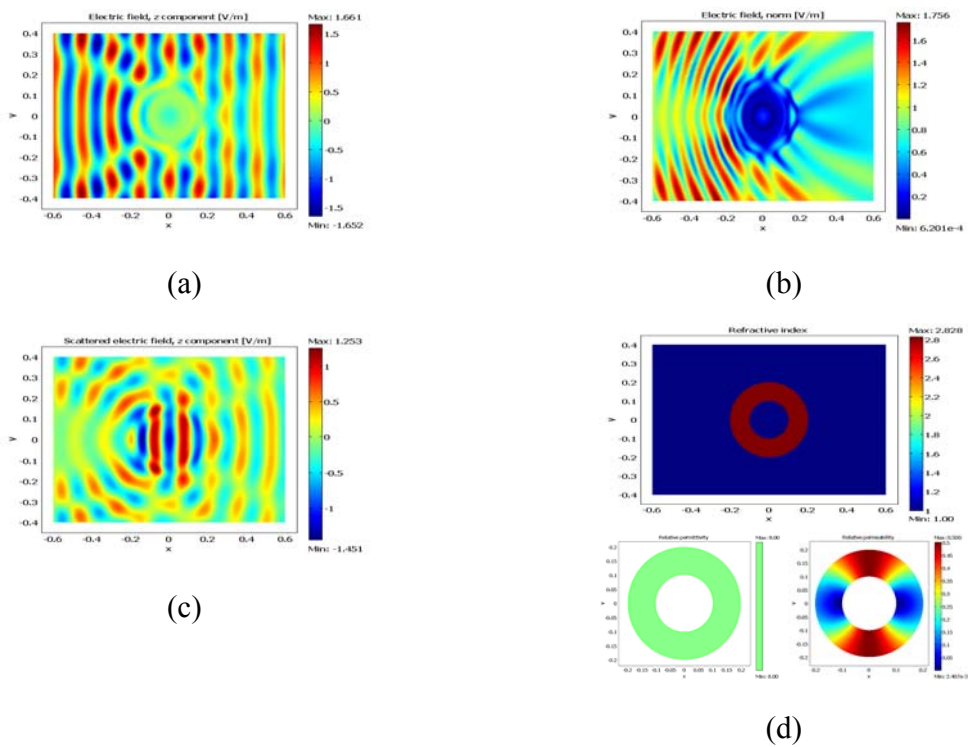


**Figure D9** TE-wave simulation of reduced cloak (a) Electric field Ez (b) Normal of Electric field Ez (c) Scattered electric field scEz (d) Material specification of cloak

There is more distortion in the calculated Electric field  $E_z$  in Fig. D9 (a) as a result of the reduced parameter compared in Fig. D7(a). However, the electric field is bent inside the cloak around the hidden object. The normal of the electrical field is nonzero at the interface between the cloak and hidden object as indicated in Fig. D9 (b) .The forward scattering is observed in Fig. D9 (c). On the other hand, there is much less back forward scattering.

The electric field  $E_z$  is calculated under a incident point source out as presented in Fig. D10 (a). However, the normal of the electrical field is the same in Fig. D10 (c) as the total field in Fig. D10(a). The software COMSOL failed to give the correct results for scattering field under point excitation. The scattered electric displacement is plotted in Fig. D10 (d). Other simulation approach should be found to test these results.

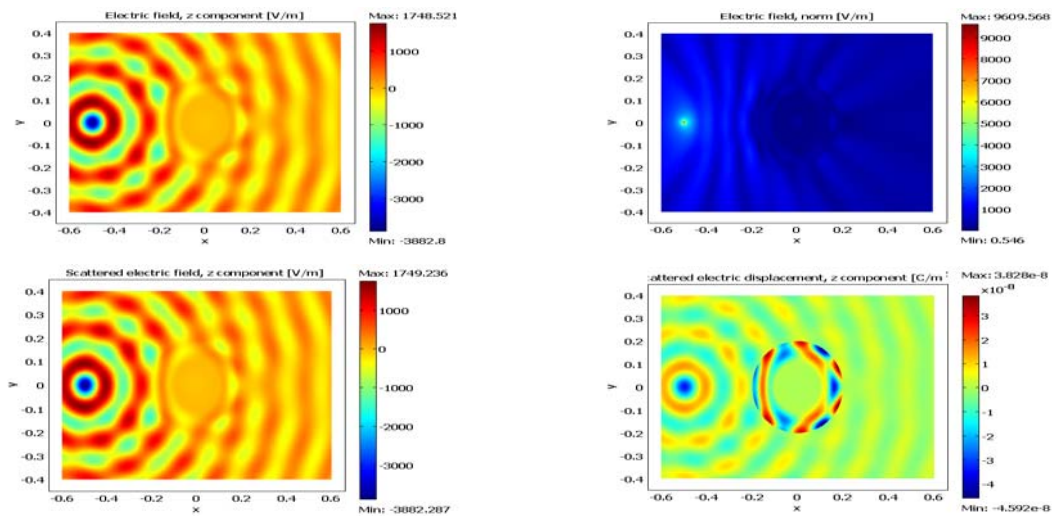


**Figure D10** TE-wave simulation of reduced cloak under a point source (a) Electric field  $E_z$  (b) Normal of Electric field  $E_z$  (c) Scattered electric field  $scE_z$  (d) Scattered electric displacement

### ***Experiment measurement***

The measurement data at 60kHz is processed to obtain the scattering pressure field. At each measurement point, we acquired a pressure pulse as function of time. To obtain the intensity at each grid point, we define the intensity as  $I = \frac{1}{T} \int_0^T p^2 dt$ . The intensity distributions are shown in Fig.D12 (a-d) by process the measurement data. Due to the point-like transducer, there is stronger field observed closer to the source.

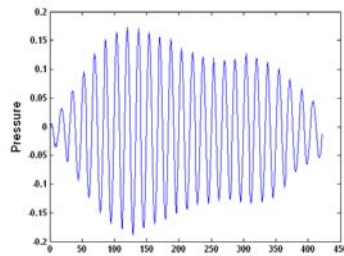


**Figure D11 Measured pressure amplitude at a grid point**

Strong scattering presented in Fig.D12 (a) when there is a bare object in the center of the water tank. However, with a cloak, the intensity is more homogeneous on the exit side of the cloak. Fig. D12(c) is the intensity distribution there is no object in the water tank. The intensity of the measured pressure field of a cylinder with same dimension with the cloak but no acoustic circuit machined is shown in Fig. D12 (d). Large shadowing area is observed resulted from this cylinder.

The intensity of the scattering field is calculated as

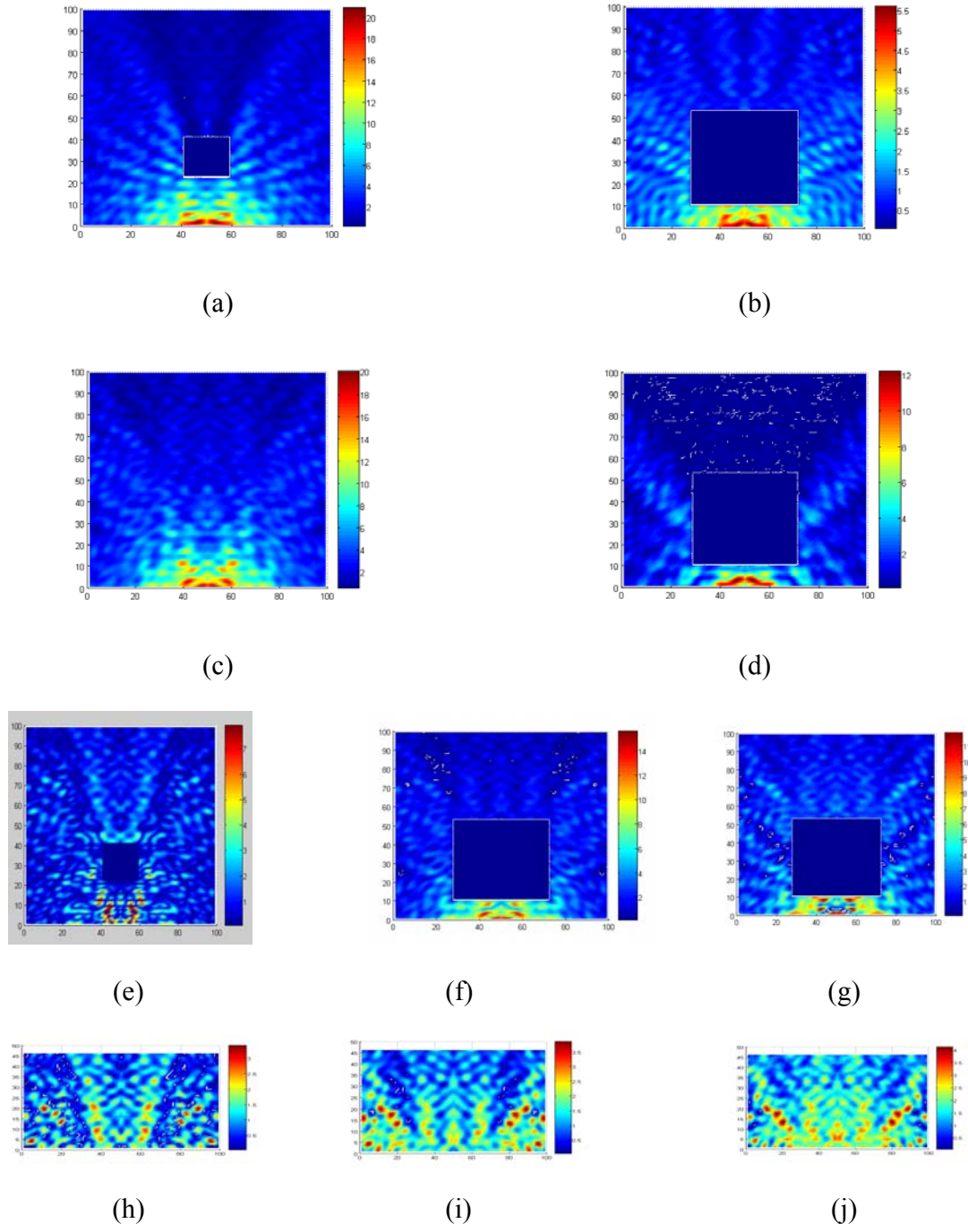


**Figure D12** Measured intensity of the pressure field of (a) bare object (b) cloak (c) free space (d) large cylinder. The intensity of the scattering field of (e) bare object (f) cloak and (g) large cylinder. (h)(i)(j) are the zoom in of the square area in (e)(f)(g) respectively.

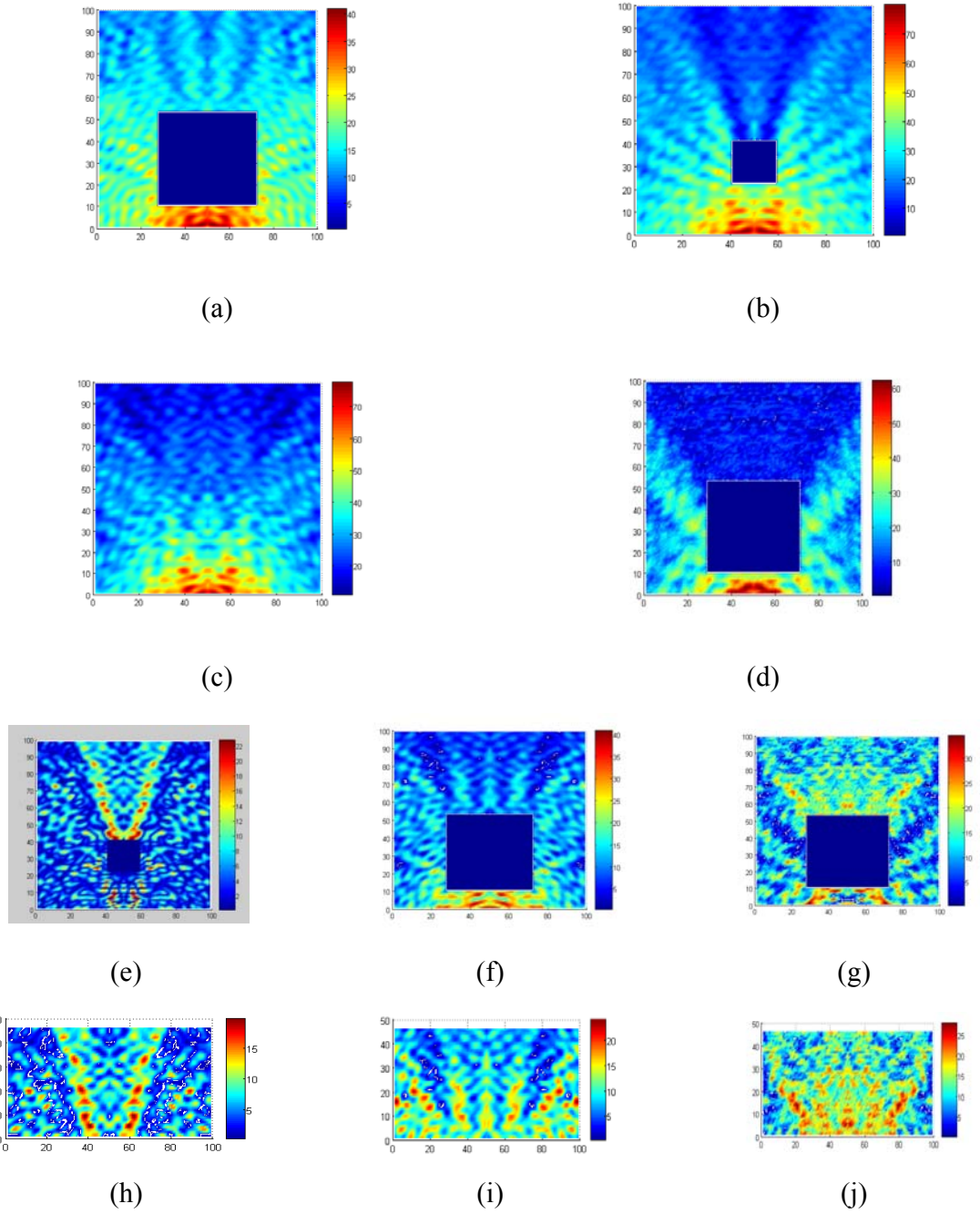


**Figure D13** Measured intensity of the pressure field of (a) bare object (b) cloak (c) free space (d) large cylinder. The intensity of the scattering field of (e) bare object (f) cloak and (g) large cylinder. (h)(i)(j) are the zoom in of the square area in (e)(f)(g) respectively.

The intensity of the scattering field of bare object, cloak and large cylinder is shown in Fig.D12 (e-g). Fig.D12 (h-j) are the zoom in of the square region marked by dashed lines in Fig.D12 (e-g) respectively. The patterns of the backward scattering are very similar for three cases. However, the backward scattering from the bare object is concentrated in the center area while there is higher intensity in the corner scattered from the cloak. When the cylinder is not machined with the acoustic circuit network, there is much larger shadowing area observed in Fig.D12 (g)

In another data processing, the intensity is defined  $a(x) \approx \int |P(x,t)| dt = \sum_n |P_n(x)|$  The same measurement data at 60 kHz is processed to obtain the scattering pressure field. The intensity distributions are shown in Fig.D13 (a-d) by process the measurement data. Due to the point-like transducer, there is stronger field observed closer to the source.

Large shadowing area is presented in Fig.D13 (a) when there is a bare object in the center of the water tank. However, with a cloak, the intensity is more homogeneous on the exit side of the cloak. Fig. D12(c) is the intensity distribution there is no object in the water tank. The intensity of the measured pressure field of a cylinder with same dimension with the cloak but no acoustic circuit machined is shown in Fig. D12(d), shadowing much larger shadowing area compare with the cloak in Fig. D12(b).

The intensity of the scattering field is calculated as

$$\begin{aligned}
 I_{sc,cloak}(x) &\approx I_{cloak}(x) - I_{freespace}(x) \\
 I_{sc,hiddenobj}(x) &\approx I_{hiddenobj}(x) - I_{freespace}(x) \\
 I_{sc,cylinder}(x) &\approx I_{cylinder}(x) - I_{freespace}(x)
 \end{aligned}$$

The intensity of the scattering field of bare object, cloak and large cylinder is shown in Fig.D13

(e-g). Fig.D13 (h-j) are the zoom in of the square region marked by dashed lines in Fig.D13 (e-g) respectively. A strong scattering in beam shape is observed from the bare object while scattering shows stronger in the corner from the cloak. When the cylinder is not machined with the acoustic circuit network, there is much larger shadowing area observed in Fig.D13 (g)

## APPENDIX E: EXPERIMENTAL SETUP AND DATA ACQUISITION

### *Negative index lens*

To study the focusing phenomena of the acoustic metamaterial in experiment, we machined a 2D array of periodically connected subwavelength Helmholtz resonators in an aluminum plate and the resonators are filled with water. The left half part is composed of a 2D array (40 by 40) of larger cavities connected with main channels. The volume of the cavity is around ten times of that of one section of the channels. The periodicity (3.175mm) of the sample is one-eighth of the wavelength at around 60 kHz frequency range. The right half part of the sample is the dual configuration of the left half part, in which there is an array (40 by 40) of orifices connected with channels. The volume of one section of the main channel is designed as around ten times of that of the orifice.

For experimental confirmation of ultrasound focusing in this acoustic metamaterial, we measured the pressure field through this PI/NI interface. The ultrasound waves were launched from a horn shaped transducer with a tip of 3mm diameter in size. The tip is inserted into a hole drilled through the center of the PI part ((column, row) = (20, 20)) to illuminate the sample. A waveform generator (Tektronix AFG 310) is used to drive the transducer. The source generated a

Periodicity of the lattice:	0.125	0.125
Diameter of the open hole:	0.04	0.04
Length of the open hole:	0.0378	0.06
Depth of the channel_left:	0.1128	0.1654
Width of the channel_left:	0.055	0.06
Diameter of the cavity:	0.0911	0.0943
Depth of the cavity:	0.0645	0.0817
Depth of the channel_right:	0.0478	0.05
Width of the channel_right:	0.04	0.03
Resonance frequency_left(KHz):	50	35
Working frequency for the refractive index to match(KHz)	60	45
Resonance frequency_right(KHz):	72	57.8571
Wavelength at working frequency(inch)	0.9731	1.2975
ratio	7.7848	10.3797
Inductance_left:	2.25E+06	2.95E+06
Capacitance_left:	4.50E-18	7.02E-18
Inductance_right:	1.56E+06	1.78E+06
Capacitance_right:	3.13E-18	4.25E-18
Volume of the openhole_left	4.75E-05	7.54E-05
Volume_channel_left	6.05E-04	9.43E-04
Volume_channel_right	6.49E-05	4.61E-05
Volume_cavity_right	4.20E-04	5.70E-04

**Figure E1** Geometry parameter of the negative index lens

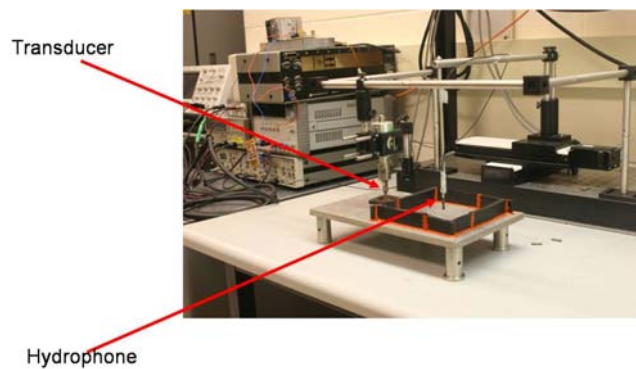


**Figure E2** Experimental setup for acoustic negative index lens

burst of sine waves with a width of 5 periods. To map the pressure field, a hydrophone was mounted on two orthogonal linear translation stages. By stepping the miniature hydrophone (RESON TC4038-1) to the positions above those through holes in the NI part and recording the pressure amplitude at every step, we acquired the spatiotemporal field distribution of the ultrasound wave focusing pattern. The pressure field is afterwards amplified by Stanford research systems model SR650 and captured using a digital oscilloscope (Agilent DSO6104A) and then

downloaded to a computer for post processing and analysis. The field pattern in the NI part at frequency of interest was obtained by Fourier transformation of the acquired pulse at each grid point, allowing the wave amplitude of each frequency component to be plotted as a function of position in the NI part. The limitations on the transducer working spectrum prevent us from probing the acoustic wave field below 60 KHz. One Labview program is wrote to control the experimental scanning.

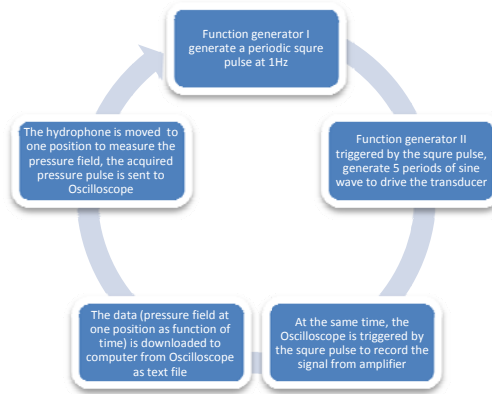


**Figure E3** Sequence of tasks in a circular flow controlled by Labview in the experiment

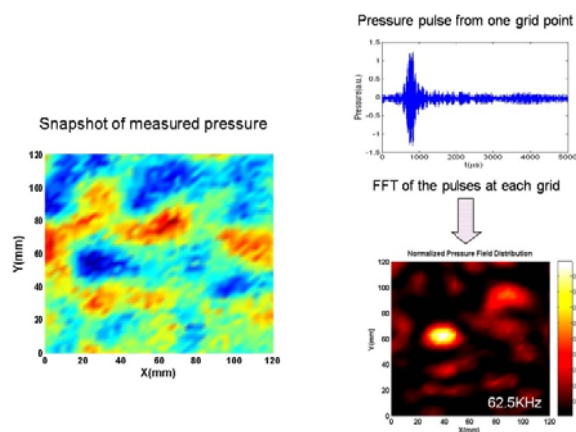


**Figure E4** FFT of the measurement data

### *Acoustic cloaking*

To demonstrate the shielding phenomena, the sample of cloaking is placed in a water tank to measure the pressure fields in the immediate environment of the cloaked object to compare with those without cloak. The tank edge is filled with absorbing rubber to reduce reflection. Because of the high impedance contrast between water and air as well as between water and glass, the system provides a 2D waveguide to confine the ultrasound wave propagation. The side of the cloak machined with the network structure is placed against the bottom of the tank. The cloak has a thickness of 3mm with the depth of the cavities smaller than 1.36 mm. The water inside the cloak is connected to the surrounding water which is 1.5 mm deep through the channels along the radial direction around the outer boundary of the cloak.

The ultrasound signal from a spherical shape transducer is launched to the water as a point source. A waveform generator (Tektronix AFG 310) is used to drive the transducer. The source generated a burst of sine waves with a width of 20 periods. The pressure field around the cloak sample in the water is detected by a miniature hydrophone (RESON TC4038-1), amplified by Stanford research systems model SR650 and captured using a digital oscilloscope (Agilent DSO6104A) and then downloaded to a computer for post processing and analysis. The hydrophone is attached to a motorized translation stage. The control program of a customized LabVIEW scans across the data acquisition region by moving the hydrophones in a small

increment 3mm to record the spatiotemporal distribution of the pressure field. The snapshot of the field pattern can be plotted as a function of position. To verify the broad operational bandwidth of the acoustic cloak, the transducer is excited over a discrete set of frequencies to illuminate the sample. The transducer operating spectrum limits us to test the frequency range from 52 kHz to 64 kHz. Similar sequence of tasks is controlled by a Labview program in the experiment.

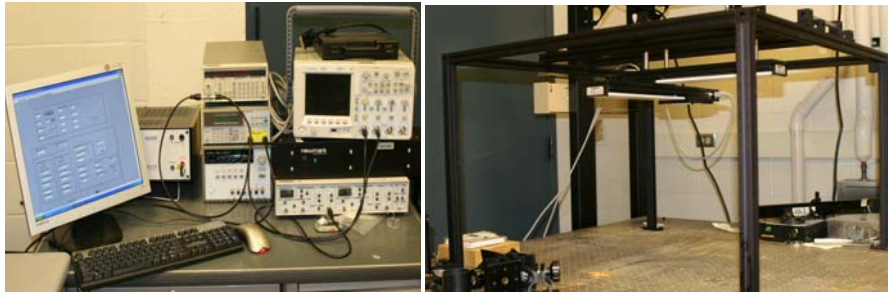


**Figure E5** Experimental setup for acoustic cloaking device

## APPENDIX F: CIRCUIT MODELING

### *Circuit modeling vs. full-wave simulation*

To develop an understanding of the difference between a full wave simulation of a distributed system and the correspondingly lumped circuit modeling, I conduct a simple analysis to quantify the comparison. In this analysis, I calculated the phase difference between two neighboring units in a periodic structure.

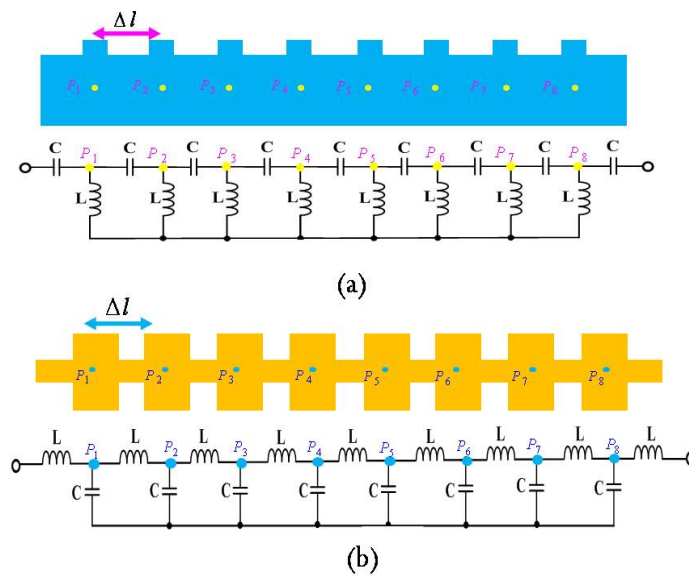
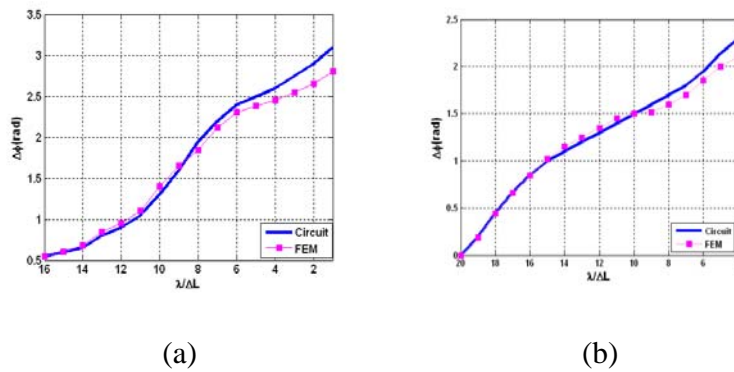


**Figure F1** A distributed acoustic system of the corresponding circuit model with (a) a high-pass topology (b) and a low-pass topology

In the first example, a main transmission channel with recurrent side branches, which are open at the outer end as show in Fig. F1(a), is simulated by FEM. This system is analogous to a

circuit of a series of capacitors with shunt inductors. On the other hand, an array of large cavities connected by small necks can be described by a lumped network of a series of inductors with shunt capacitors as presented in Fig.F1 (b).

To help the comparison, I chose those points in the center of the channel to calculate the phase lag. And in the circuit model, the phase can be more easily read from the two connecting nodes.



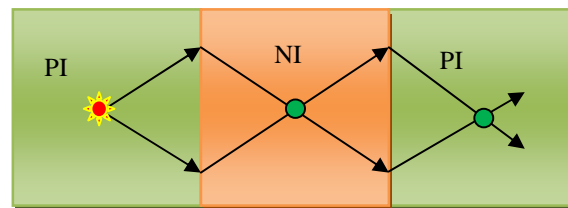
**Figure F2** Phase difference as a function of the ratio between wavelength and the unit cell size for (a) high-pass and (b) low-pass topology

Fig.F2 presents the phase difference as a function of the ratio between wavelength and the unit cell size. As shown in Fig. F2 (a-b), when the unit cell is very small compared with wavelength; the two models gave the value of phase advance between two units. However, as frequency increases, the unit cell appears larger to the incident acoustic waves. As a result, the errors increase at shorter wavelength. Because of the high-pass topology, the calculation can not

be carried at wavelength longer than 16 times of the size of the unit cell. On the other hand, the wave cannot be transmitted at higher frequency in low-pass topology with wavelength longer than two times of the size of the unit cell.

This analysis demonstrates that the equivalent circuit modeling can provide the desired information about wave propagation through the distributed acoustic system when the unit cell is smaller than one-eighth of wavelength.

### *Circuit modeling of negative index lens*



**Figur F3** A flat lens brings all the diverging rays from an object into two focused images

To study the ultrasound focusing by a negative index lens, a two-dimensional circuit model is simulated employing commercial software SPICE. The calculated lumped model is an approximation of the distributed acoustic system. The acoustic metamaterial with negative refractive index (NI) is composed by a two-dimensional (2D)  $30 \times 30$  periodic cascaded array of the unit cell as in **Error! Reference source not found.** (a). In order to build a PI/NI interface, an acoustic metamaterial with positive index (PI) is implemented by  $30 \times 30$  circuit cells as

shown in **Error! Reference source not found.** (b). In the simulation, the negative index lens is sandwiched between two positive index medium. In the circuits, a very small resistance is connected to each inductor. The boundary of the simulation model is grounded by a resistor with value equal to the characteristic impedance of the transmission line to reduce the reflection from the boundary.

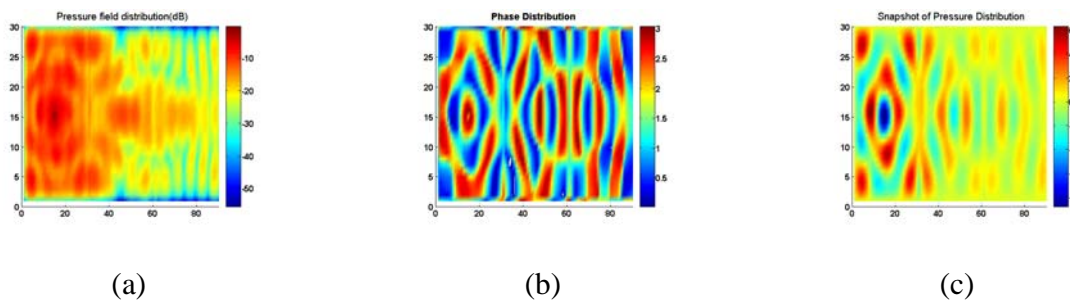


**Figure F4** Pseudo colormap of scaled pressure (a) amplitude and (b) phase distribution and (c) a snapshot due to a point source illuminating a 2D transmission model of the PI/NI/PI interface.

Fig.F4 (a) and (b) illustrates the normalized pressure magnitude and phase distribution at steady state when a continuous signal at 60 kHz is introduced at the center of the PI part. The  $x$ - $y$  axes are labeled according to the cell number. The maximum field magnitude was normalized to unity. The focal point is expected around node (45, 15) and (75, 15) since the relative index value equals  $-1$  at 60 kHz. In Fig.F4 (a) and (b), focusing is evident by the increased transmission and confinement of the fields near the focal plane (near node (45, 15) and (75, 15)). Moreover,

concavity waterfronts are observed near the two focuses as evident in Fig.F4(b). Fig.F4(c) is a snapshot of the pressure field at steady state.